2015

Design and Fabrication of Ultrathin Plasmonic Nanostructures for Photovoltaics, Color Filtering and Biosensing

Beibei Zeng
Lehigh University

Design and Fabrication of Ultrathin Plasmonic Nanostructures for Photovoltaics, Color Filtering and Biosensing

by

Beibei Zeng

Presented to the Graduate and Research Committee

of Lehigh University

in Candidacy for the Degree of

Doctor of Philosophy

in

Electrical Engineering

Lehigh University

January, 2015

Approved and recommended for acceptance as a dissertation in partial fulfillment of the requirements for the degree of Doctor of Philosophy.

_____
Date

Dr. Filbert J. Bartoli
Dissertation Director

_____
Accepted Date

Committee Member:

_____
Dr. Filbert J. Bartoli
(Chairman and Advisor)

_____
Dr. Zakya H. Kafafi

_____
Dr. Sushil Kumar

_____
Dr. Xuanhong Cheng

_____
Dr. Daniel Ou-Yang

Acknowledgements

First and foremost, I would like to express my sincere gratitude to my advisor Prof. Filbert J. Bartoli for his support, guidance, and inspiration in the last four years of my Ph.D. study. All the results presented in this doctoral dissertation would not have been achieved without his support and contribution. His scientific vision, critical thinking, and creativity are remarkable. He helps me gradually become mature as a scientist. I feel lucky to be his student and have benefited in every possible way that a student can benefit under his support and guidance.

I would also like to thank my committee members, Prof. Zakya H. Kafafi, Prof. Xuanhong Cheng, Prof. Sushil Kumar, and Prof. Daniel Ou-Yang, for their advices and collaborations in my Ph.D. study. The presented work in three different but related areas are interesting interdisciplinary projects that require expertise in the fields of nanophotonics, photovoltaics and biomedical sciences. I cannot accomplish this much without their expertise and advices throughout these years. I also want to specially thank Dr. Yongkang Gao. He is not only my colleague but also a friend to me, from whom I learnt a lot in the area of plasmonic biosensors.

I want to thank all my friends at Lehigh: Yaqing Ning, Le Zhao, Yadan Tang, Xia Luo, Sudeep Khanal, Tamara Bidone, Jing Liu, Xin Cui, Mengcen Qian, Estefania Perdomo, Fang Chen. Thank you all for your accompany. I want to thank Yanhui Zhao at Penn State University and Ting Xu at NIST, for being my friends since the first year of my master study at IOE of Chinese Academy of Sciences.

I want to thank my parents and my little brother for everything they gave me. It is because of your endless support, love, and caring that I can make my dream come true. I want to dedicate this dissertation to my parents.

Finally, I want to thank my wife, Chaolan He, for all your understanding and support.

Table of Contents

List of Figures

Abstract

Since the first report of the extraordinary optical transmission (EOT) phenomenon through periodic subwavelength hole arrays milled in optically-thick metal film, plasmonics have generated considerable interest because they enable new fundamental science and application technologies. Central to this phenomenon is the role of surface plasmon polaritons (SPPs), which are essentially electromagnetic waves trapped at the interface between a metal and a dielectric medium through their interactions with free electrons at the metal surface. The resonant interaction between the incident light and surface charge oscillations enables the *concentration* and *manipulation* of light at deep subwavelength scales, opening up exciting application opportunities ranging from subwavelength optics and optoelectronics to bio/chemical sensing. Furthermore, additional phenomena arise as the thickness of metal film decreases to be comparable to its skin depth (optically-thin), and the single-interface SPPs on the top and bottom metal surfaces combine to form two coupled SPPs, the long-range and short-range SPPs. Until now, much less work has focused on the study of surface plasmon resonances (SPRs) in ultrathin nanostructured metals.

This dissertation seeks to elucidate underlying physical mechanisms of SPRs in ultrathin nanostructured metals and tailor them for practical applications. Inspired by state-of-the-art advances on plasmonics in optically-thick nanostructured metals, one- (1D) and two-dimensional (2D) ultrathin plasmonic nanostructures are exploited for particular applications in three essential areas: *photovoltaics*, *color filters* and *biosensors*,

achieving superior performances compared with their optically-thick counterparts. More specifically, this thesis is focused on systematic investigations on: (1) **plasmonic transparent electrodes** for organic photovoltaics and polarization-insensitive optical absorption enhancement in the active layer; (2) **plasmonic subtractive color filters** with record-high transmission efficiency and other unique properties; (3) rapid and highly-sensitive **plasmonic bio-sensors** employing ultrathin nanogratings. The successful development of these new plasmonic platforms have far-reaching impact on green energy technologies, next-generation displays and imagers, and label-free bio-sensing for point-of-care diagnostics.

Chapter 1

Introduction

1.1 Motivation

Over the past few decades, major technological revolutions have transformed our society and daily lives. Their remarkable innovations have been based primarily on our improved ability to manipulate two particles: **electrons** and **photons**. In particular, the control of electrons in semiconductor materials has generated fundamental changes, with laptops, mobile phones, and digital cameras, etc. On the other hand, the development of materials and devices with which to control photons has made major changes in society, such as wireless communication and the use of optical fibers and microwaves. However, electronic and photonic devices have their own shortcomings: electronic devices have nanoscale critical dimensions but low operating speed below 10 GHz; in stark contrast, photonic components possess high operating speed and bandwidth, but are limited in their size by the laws of diffraction [1.1].

Surface Plasmon Polaritons (SPPs) are hybrid modes that constitute an electromagnetic field (photons) coupled to oscillations of surface charges (electrons) at the metal surface, as shown in Fig. 1.1. In this interaction, the free electrons oscillate collectively in resonance with the incident photons, resulting in surface plasmon resonances (SPRs). The resonant interactions between the photons and the electron oscillations give rise to the unique properties of concentration and manipulation light at

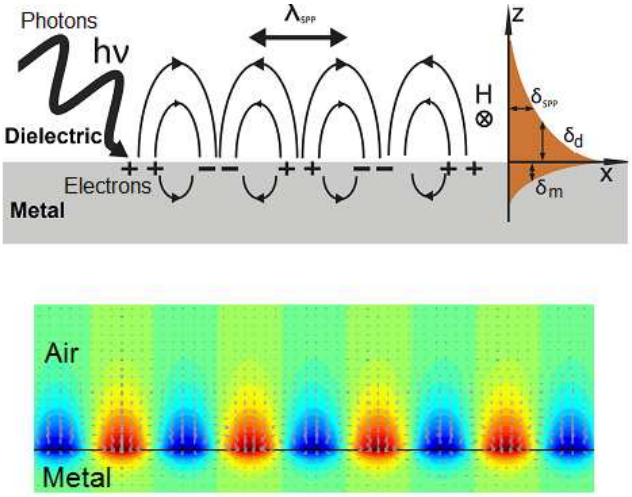

Fig. 1.1 Upper, SPPs at the interface between a metal and dielectric have a combined electromagnetic wave (photon) and surface charge (electron) character; lower, calculated electromagnetic field distributions of SPPs at the air/metal interface.

subwavelength scales [1.1-1.4]. SPPs are attractive candidates for overcoming the size limitation that the diffraction law imposes on conventional dielectric photonic structures. Consequently, SPPs offer precisely what electronics and photonics do not have: the size of electronics and the speed of photonics. Plasmonic structures and devices employing SPPs in the optical domain have the potential for applications such as on-chip integration of subwavelength optical circuits, data storages [1.1], and bio-sensing [1.2].

Fig. 1.2 The Lycurgus cup in British Museum dated back to 4th century AD. Due to scattering of metal nanoparticles on sidewall (5–60 nm in diameter), the cup appears green in reflected light, and red in transmission light. Inset: SEM image of a typical nanoparticle embedded in the glass.

The coupling of light (photons) to electrical charges (electrons) at metal surfaces was utilized hundreds or even thousands of years ago for the coloration of some particular historical artifacts, as shown in Fig.1.2, but the science was not known at that time. In the 1950s, surface plasmons (SPs) were widely recognized in the field of surface science following the pioneering work of Ritchie [1.5]. With the development of modern fabrication (i.e., electron-beam and focus ion-beam lithography, EBL and FIB) and characterization (i.e., scanning electron and atomic force microscopy, SEM and AFM) tools, renewed interests are focused on unique properties of controlled metallic nanostructures (that is, plasmonic) [1.3, 1.6], resulting in the explosion of plasmonics research in the past decade or so.

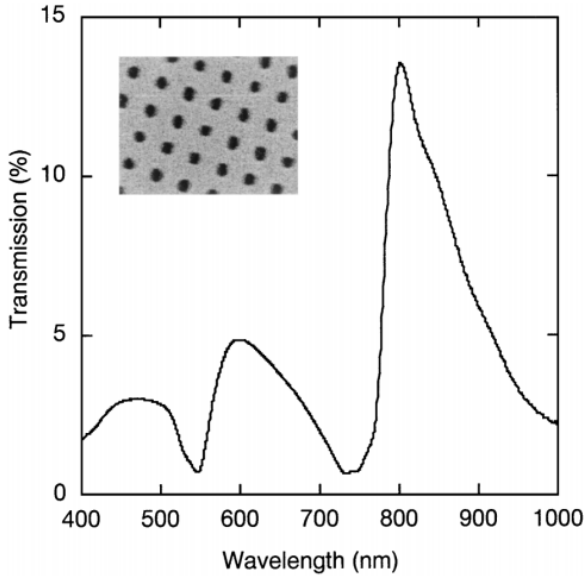

Fig. 1.3 Measured zero-order power transmittance, T_{00}, at normal incidence for a square array of nanoholes (period L=750 nm, average hole diameter of 280 nm) in a freestanding optically-thick Ag film (thickness h=320 nm). Inset is a SEM graph of the nanostructured metal film [1.8].

In this context, the first report of the extraordinary transmission (EOT) phenomenon through a subwavelength periodic array of nanoholes milled in an **optically-thick** metal

is a milestone in modern plasmonics [1.7], which has generated considerable interests in plasmonics research, enabling a dramatic growth in both fundamental sciences and device technologies. Fig. 1.3 shows the experimental "zero-order" optical transmittance (T_{00}), at normal incidence, through a periodic array of nanoholes patterned on a 320nm-thick metal film [1.8]. The period of the hole array L=750 nm, and the holes had an average diameter of 280 nm. The EOT effect is clearly observed: at the wavelength λ=800 nm, T_{00} of the order of 15% was measured. As the area covered by holes is only 11%, the normalized-to-area transmittance of light is 136%, which are orders of magnitude larger than 1% expected from the standard aperture theory for a single nanohole [1.9]. Besides its fundamental interests of light interacting with nanostructured metals, this EOT effect has opened up exciting application opportunities in photonics and optoelectronics, such as photolithography, chemical- or bio-sensors, wavelength-tunable filters, optical modulators, among others [1.6, 1.10].

On the other hand, as the thickness of metal film decreases to be comparable to its skin depth (tens of nanometers in visible regions, **optically-thin**), the single-interface SPPs at the top and bottom flat metal surfaces combine to form two coupled SPPs, the long-range and short-range SPPs (LR-SPPs and SR-SPPs) [1.11]. Until recently, much less work has been attributed to study SPRs in ultrathin metal films patterned with nanostructures [1.12]. In 2009, unexpected behavior of extraordinary low transmission (ELT) opposite to the EOT phenomenon was found in ultrathin Au films patterned with periodic subwavelength hole arrays: less light is transmitted through the perforated film

compared to the closed metal film [1.13]. Fig. 1.4 (a) shows a SEM image together with a scheme of the structure. A 2×2 cm^2 square hole array (period P=300 nm and hole diameter of D=200 nm) was fabricated on an ultrathin Au film (t=20 nm) by optical interference lithography. Surprisingly, additional holes do not increase the optical transmission through the ultrathin Au film, but the inverse effect is observed: the transmission is reduced in the spectral region from 1.8eV to 2.5eV, as shown in Fig. 3 (b).

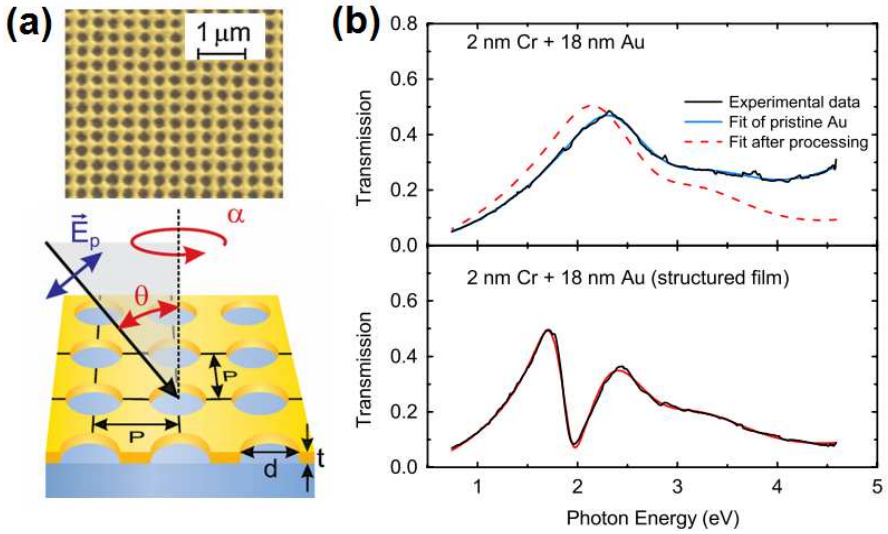

Fig. 1.4 (a) SEM image and scheme of the investigated nanohole arrays. Period P=300 nm; hole diameter D=200 nm; Au film thickness t=20 nm. (b) Transmission spectra of the unpatterned ultrathin Au film (top) and the nanohole arrays (bottom) at normal incidence [1.13].

This inspiring work has stimulated much fundamental research from many different groups [1.13-1.17], since the perfect electrical conductor (PEC) approximation used in Bethe theoretical descriptions of how light is passing through subwavelength apertures in an perfect metal film with infinitesimal thickness becomes invalid in this case. Although a general agreement exists that SPPs play a crucial role, there is still an ongoing debate on underlying physics leading to the ELT effect in ultrathin nanostructured metals [1.13, 1.16]. For instance, some researchers believed that the excitation of SR-SPPs leads to a

strong absorption and thus suppresses the transmission [1.13, 1.15]. However, the other groups argued that the quenched transmission must be ascribed to localized-SPRs (LSPRs), while SR-SPPs play only a marginal role in this anomalous effect [1.16]. Besides fundamental studies, some practical applications of ultrathin nanostructured metals have been initially proposed by different groups. For example, Fan's group has theoretically investigated the use of optically-thin (10nm-thick) nanopatterned metallic films as transparent conductive electrodes (TCEs) in optoelectronic devices [1.18]. However, compared with their optically-thick counterparts, ultrathin nanostructured metals have been much less studied for practical purposes, which may provide superior performance in some applications, such as plasmonic-enhanced photovoltaics, color filters, and optical biosensors, etc.

Therefore, it is highly desirable to systematically investigate the light-matter (photon-electron) interactions in ultrathin nanostructured metals for both fundamental sciences and practical applications. Theoretical and experimental analysis will be employed to fully clarify different electromagnetic modes in ultrathin nanostructured metals with different geometric parameters, finding niche applications in three areas of plasmonic-enhanced organic photovoltaics (OPVs), plasmonic color filters, and plasmonic biosensors.

In this chapter, I will first introduce the basic concepts and mechanisms for different SPP modes, including the dispersion relations, coupling mechanisms of single-interface

SPPs, LR- and SR-SPPs, and LSPRs. Then, the organization of this thesis will be outlined.

1.2 Single-interface SPPs on a smooth metal/dielectric interface of optically-thick metal films

The electromagnetic fields associated with SPPs are enhanced at metal/dielectric interfaces and decay exponentially into the media on either side of the interface. The electron charges on a metal surface can perform coherent fluctuations, also known as surface plasmon oscillations [1.4]. In this section, we discuss the fundamental properties of SPPs on the flat smooth single metal/dielectric interface.

1.2.1 Dispersion Relations of single-interface SPPs (SI-SPPs)

Let's start from a light wave propagating in free space [see Fig. 1.5(a)], it is described as follows:

$$E = E_0^{\pm} \exp[+i(k_x x \pm k_z z - \omega t)] \qquad (1.1)$$

Here, k_x and k_z are propagating constant in x and z directions, respectively. ω is the frequency of the electromagnetic (EM) wave. Suppose k_0 is the absolute value of the propagation constant of the EM wave, and consists of two components in x and z directions. So, in the medium: $k_0^2 = \varepsilon_0 \cdot \left(\frac{2\pi}{\lambda_0}\right)^2 = k_x^2 + k_y^2$, as shown in Fig. 1.5 (a). Here, ε_0 is relative permittivity of the medium (e.g. ε_0 =1 for air).

In the ω–k_x diagram, light waves with different incident angles are represented by dashed straight lines, as shown in Fig. 1.5 (b). The slope of the light line is $c/(\sqrt{\varepsilon_0}\, sin\theta_0)$. When light is propagating in air or vacuum at an angle θ_0, the light line is marked by

number 1. When the incident angle θ_0 is 90 degrees (propagating in the *x* direction), it is line 2. If it propagates in a medium with relative permittivity ε_0, it is line 3. So, in the air ε_0 =1, the largest propagation constant in the *x* direction is k_2, which is equal to k_0.

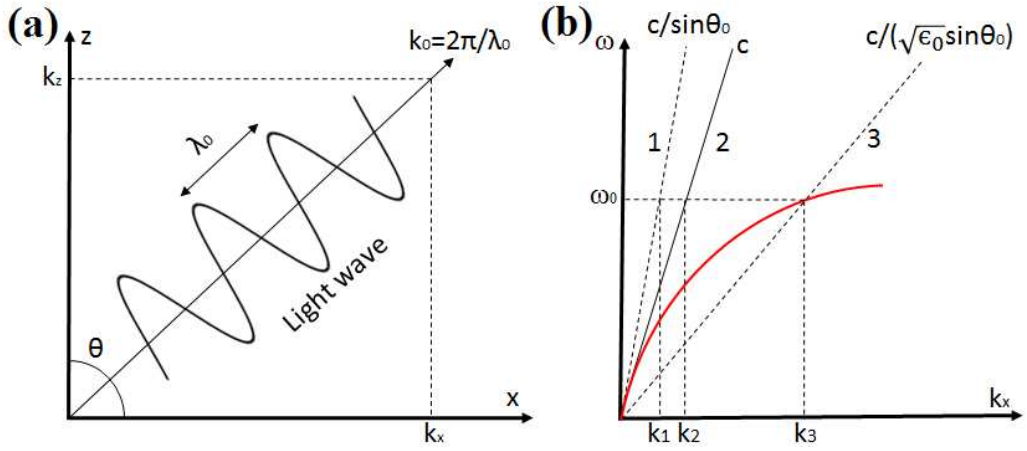

Fig. 1.5 (a) A wave vector of free-space light waves, k_0, in x-z plane; (b) an example of the dispersion relation of SPPs.

Now, let's consider the dispersion curve of the SPP modes supported by a metal/air interface. Maxwell's equations with boundary conditions yield the retarded dispersion relation for the plane surface of a semi-infinite metal film with the dielectric function $\varepsilon_1 = \varepsilon_1' + i\varepsilon_1''$, adjacent to a medium ε_0 as air or vacuum:

$$D_0 = k_{z1}/\varepsilon_1 + k_{z2}/\varepsilon_0 = 0 \tag{1.2}$$

$$\varepsilon_i \cdot \left(\frac{\omega}{c}\right)^2 = k_x^2 + k_{zi}^2 \quad (i = 0, 1) \tag{1.3}$$

Since the wave vector k_x is continuous through the metal/air interface, the dispersion relation can be described as:

$$k_x = \frac{\omega}{c}\left(\frac{\varepsilon_1\varepsilon_0}{\varepsilon_1 + \varepsilon_0}\right)^{1/2} \tag{1.4}$$

Incorporating the relative permittivity of metal $\varepsilon_1 = \varepsilon_1' + i\varepsilon_1''$ (real and imaginary part),

we obtain,

$$k_x' = \frac{\omega}{c}\left(\frac{\varepsilon_1'\varepsilon_0}{\varepsilon_1'+\varepsilon_0}\right)^{1/2}$$

(1.5)

$$k_x'' = \frac{\omega}{c}\left(\frac{\varepsilon_1'\varepsilon_0}{\varepsilon_1'+\varepsilon_0}\right)^{3/2}\frac{\varepsilon_1''}{2(\varepsilon_1')^2}$$

(1.6)

The dispersion curve of SPPs obtained using Eq. (1.5) is shown by the red curve in Fig. 1.5 (b), which approaches the free-space light line at small k_x, but remains beyond the light line 2, so that SPPs cannot transform directly into free-space light: it is a "non-radiative" EM wave. At a given frequency ω_0, the propagation constant of SPP modes along the *x* direction, k_3 (k_{spp}), is larger than that of the EM wave in free space, k_2 (k_0). Considering that $k_0^2=k_x^2+k_{zi}^2$, one obtains $k_{zi}^2= k_0^2- k_x^2 <0$. Consequently, k_{zi} is imaginary. When the k_{zi} is incorporated into Eq. (1.1), there will be an exponential decay component of exp ($-|k_{zi}|z$). In this case, the light intensity will decay exponentially with the distance from the interface. EM waves with this behavior are evanescent waves, which are highly confined to the metal/dielectric interface, see Fig. 1.1.

Some critical characteristics of SI-SPPs can also be defined as follows:

1. **Skin depth.** As mentioned above, the EM field amplitude of the SPPs decreases exponentially as exp ($-|k_{zi}|z$), normal to the metal surface (z direction), as shown in Fig. 1.1. The skin depth at which the EM field falls to 1/e becomes

$$z = \frac{1}{|k_{zi}|} \tag{1.7}$$

Therefore, in the medium 1 (e.g. metal), $\delta_m = z_1 = \frac{\lambda}{2\pi}(\frac{\varepsilon_1' + \varepsilon_0}{\varepsilon_1'^2})^{1/2}$ (1.8)

And in medium 2 (e.g. air), $\delta_d = z_2 = \frac{\lambda}{2\pi}(\frac{\varepsilon_1' + \varepsilon_0}{\varepsilon_0^2})^{1/2}$ (1.9)

For instance, for wavelength λ=600nm, on obtains $\delta_m = z_1$=24nm and $\delta_d = z_2$=390nm for Ag, and $\delta_m = z_1$=31nm and $\delta_d = z_2$=280nm for Au, respectively.

2. **Propagation length.** Similarly, the intensity of SPPs propagating along a smooth surface (x direction) decreases as $\exp(-2k_x'' x)$. From Eq. (1.6), the propagating length L_i (δ_{spp}) at which the intensity of SPPs decreases to 1/e is given by

$$\delta_{spp} = L_i = (2k_x'')^{-1} = \frac{c}{\omega}(\frac{\varepsilon_1' + \varepsilon_0}{\varepsilon_1'\varepsilon_0})^{3/2}\frac{(\varepsilon_1')^2}{\varepsilon_1''} \tag{1.10}$$

The length scales of SI-SPPs for Al and Ag films are shown in Fig. 1.6.

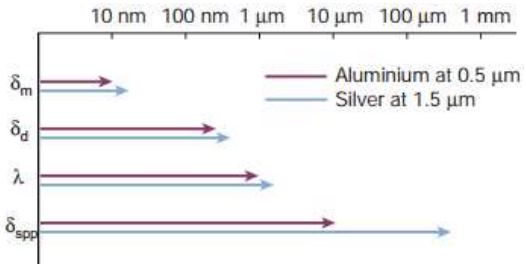

Fig. 1.6 The characteristic length scales of SI-SPPs for Al (λ=0.5μm) and Ag (λ=1.5μm) films [1.1].

1.2.2 Optical coupling of SPPs on a smooth metal/dielectric interface

The coupling of photons to SPPs meet the difficulty that the dispersion relation of SPPs lies beyond the light line, as shown in Fig. 1.5(b). In order to excite SPPs by p-polarized light incident on a planar metal surface from the adjacent dielectric medium,

the frequency of the incident light must equal the frequency of SPPs; and the wave-vector of the incident light parallel to the metal surface is $k_x=\sqrt{\varepsilon_0}\,(2\pi/\lambda_0)sin\theta_0$, where θ_0 is the angle of incidence, must equal the wave-vector of SPPs, $k_x=\frac{\omega}{c}(\frac{\varepsilon_1\varepsilon_0}{\varepsilon_1+\varepsilon_0})^{1/2}$. The first condition is easily satisfied. However, as is seen from the SPP dispersion relation in Fig. 1.5(b), the SPP wave vector is larger than that of the free-space light in the adjacent dielectric medium (air or vacuum) at the same frequency ω_0. Thus, the incident light through that medium cannot directly couple to SPPs due to the wave-vector mismatch. Therefore, special experimental arrangements have been designed to provide the necessary wave-vector conservation. Typically, the photon and SPP wave-vectors can be matched by using either photon tunneling in the total internal reflection geometry (Kretschmann and Otto configurations) or diffraction effects (Fig. 1.7). Generally, there are two popular optical coupling mechanisms for SPPs.

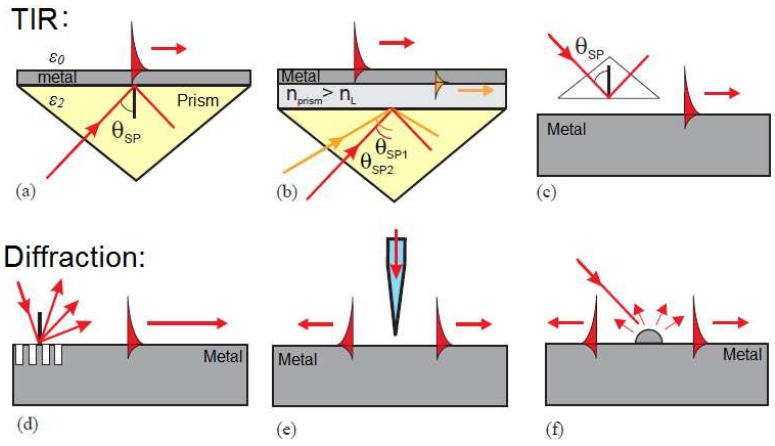

Fig. 1.7 Schematic of the optical coupling mechanisms of SPPs. (a) Kretschmann configuration, (b) two-layer Kretschmann configuration, (c) Otto configuration, (d) diffraction on a grating, (e) excitation with a SNOM tip, and (f) diffraction on a surface defect.

1) Total Internal Reflection (TIR) Coupler

If light ($k=\omega/c$) is reflected at a metal surface covered with a dielectric medium ($\varepsilon_2>1$, e.g. a quartz prism) at an angle of incidence greater than the critical angle for total internal reflection ($\theta_0>\theta_c$), see Fig. 1.7 (a), the projection of the photon wave-vector parallel to the metal surface becomes $\frac{\omega}{c}\sqrt{\varepsilon_2}(sin\theta_0)$. At the angle of incidence θ_0 at which the in-plane photon wave-vector coincides with that of SPPs at the air-metal interface, light is tunneled through the metal film and coupled to SPPs:

$$k_{spp} = \frac{\omega}{c}\left(\frac{\varepsilon_m \cdot \varepsilon_0}{\varepsilon_m + \varepsilon_0}\right)^{1/2} = \frac{\omega}{c}\sqrt{\varepsilon_2}(sin\theta_0) \qquad (1.11)$$

The dispersion relation for SPPs propagating on the air/metal interface can thus be satisfied for a given $\theta_0=\theta_{spp}$ [see the dispersion curve of SPPs and light line 3 in Fig. 1.5(b)]. Under the resonant condition, a sharp minimum is observed in the reflection spectrum as light can be coupled to SPPs with almost 100% efficiency. Since the SPP field is highly close to a metal surface, it is significantly enhanced at the surface. For example, this gives a field intensity enhancement by more than two orders of magnitude for a 60 nm-thick Ag film illuminated with light of λ=600nm [1.4]. In order to excite SPPs on the internal metal interface, an additional dielectric layer with a refractive index smaller than the prism should be deposited between the prism and the metal film, as shown in Fig. 1.7(b). In such a two-layer scheme, both SPPs on the either side of metal film can be excited, at different angles of incidence. For surfaces of bulk metal film, SPPs can be excited in the Otto configuration, see Fig. 1.7(c). Here, the prism is positioned close to the metal surface, and the photon tunneling occurs through the air gap between the prism and the metal surface.

2) Diffraction Effects

Another way to provide the wave-vector conservation for the excitation of SPPs is to use diffraction effects. For example, Fig. 1.7(d) shows a diffraction grating patterned on a smooth metal film. If light impinges on a grating with a grating period p, at an angle θ_0, the diffracted components parallel to the metal surface can have wave-vectors of $(\omega/c)\sin\theta_0 \pm m\cdot 2\pi/p$, where m is an integer indicating the order of diffraction [1.4]. The diffracted light on a periodic structure provides the wave-vector conservation and coupling to SPPs:

$$k_x = \left(\frac{\omega}{c}\right)\sin\theta_0 \pm m \cdot \frac{2\pi}{p} = \frac{\omega}{c}\left(\frac{\varepsilon_m \cdot \varepsilon_0}{\varepsilon_m + \varepsilon_0}\right)^{1/2} = k_{spp} \tag{1.12}$$

Or more generally,

$$k_x = \left(\frac{\omega}{c}\right)\sin\theta_0 \pm \Delta k_x = k_{spp} \tag{1.13}$$

where $\Delta k_x = k_{spp} - k_1$ is illustrated in Fig. 1.5 (b). When $m\cdot 2\pi/p$ equals the momentum mismatch Δk_x between the free-space photon and the SPP mode at the same frequency, the incident light can be coupled to SPP modes on the smooth metal surface by the grating. In addition, the optical excitation of SPPs can also be achieved through the diffraction of light from an isolated surface feature, as shown in Fig. 1.7 (e) and (f). Using illumination through a NSOM tip or an isolated surface defect, circular SPPs can be locally launched at the metal surface. One can consider a near-field coupling of light diffracted on the subwavelength aperture or surface defect into SPPs. It should be noted that the reverse process takes place as well: non-radiative SPPs propagating along the grating or a surface defect can reduce their wave vector k_{spp} by Δk_x, so that light can be

coupled out of SPP modes.

1.3 Long- and short-range SPPs in optically-thin smooth metal films

It is known that as the thickness of metal film decreases to be comparable to or smaller than its skin depth δ_m(e.g., δ_m=24nm for Ag at λ=600nm), two SI-SPP modes at top and bottom metal/dielectric interfaces would interact with each other and split to coupled SPR modes with extremely different propagation distances, long- and short-range (LR- and SR-) SPP modes [1.19, 1.20], which have anti-symmetric and symmetric charge distributions, respectively, as shown in Fig. 1.8.

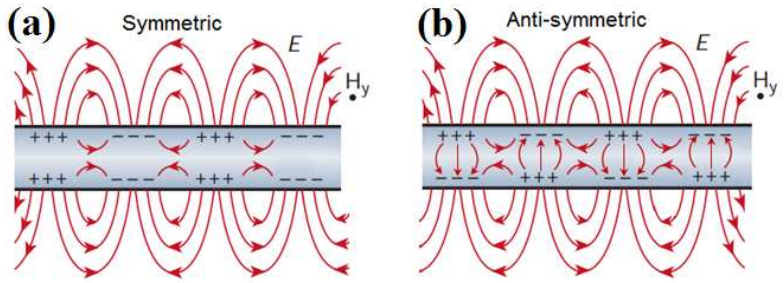

Fig. 1.8 Symmetric and anti-symmetric charge and EM distributions of SR- and LR-SPPs, respectively.

The dispersion relations for LR- and SR-SPP modes can be described by the following equation:

$$\tanh(k_2 t)(\varepsilon_{d1}\varepsilon_{d2}k_2^2 + \varepsilon_m^2 k_1 k_3) + \varepsilon_m k_2(\varepsilon_{d1}k_3 + \varepsilon_{d2}k_1) = 0 \qquad (1.14)$$

Here $k_1^2 = k_{spp}^2 - \varepsilon_{d1}k_0^2, k_2^2 = k_{spp}^2 - \varepsilon_m k_0^2$, $k_3^2 = k_{spp}^2 - \varepsilon_{d2}k_0^2$, $k_0 = \omega/c$ and t is the thickness of the metal film. ε_{d1}, ε_{d2} and ε_m are dielectric constants of the top and bottom dielectric media, and the metal, respectively. For example, for Ag films with different thicknesses from 10nm to semi-infinite, the dispersion curves of different SPPs modes are calculated using Eq. (1.14) and shown in Fig. 1.9(a). The black and red solid curves represent two SI-SPPs modes at air/Ag and SiO_2/Ag interfaces for semi-infinite Ag films, respectively. As the

film thickness decreases from 50nm to 10nm, the interaction between two SI-SPPs at air/Ag and SiO_2/Ag interfaces becomes more strongly, leading to more bended dispersion curves. On the other hand, due to the asymmetric geometry (air/Ag/SiO_2, $\varepsilon_{d1} < \varepsilon_{d2}$), Fig. 1.9(b) shows that strongly damped SR-SPP modes exist with a symmetric charge distribution at the air/Ag and SiO2/Ag interfaces for the 30nm-thick Ag film [1.21].

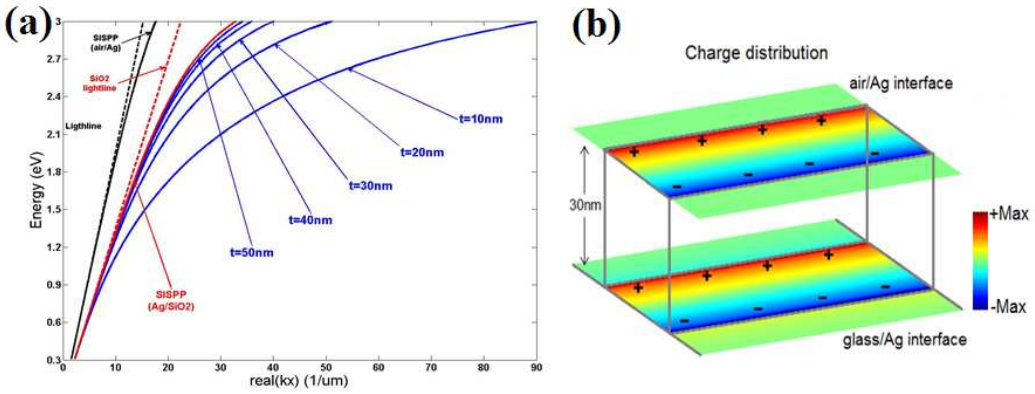

Fig. 1.9 (a) Calculated dispersion curves of SPPs for Ag film with different thicknesses from 10nm (SR-SPPs) to semi-infinite (black and red solid curves, SI-SPPs). (b) Symmetric charge distribution at the air/Ag and glass/Ag interfaces for a 30nm-thick Ag film.

1.4 Localized SPRs in metal nanoparticles

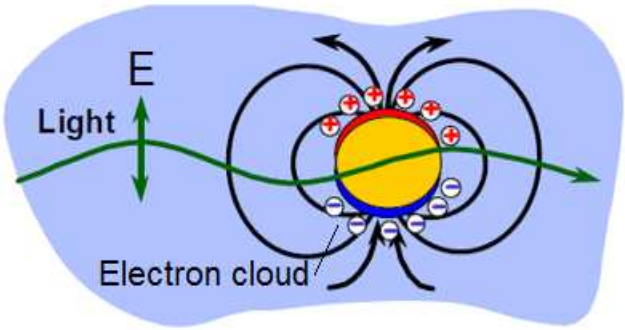

Fig. 1.10 Schematic diagram of the excitation of Localized SPRs (LSPRs) in metal nanoparticles by an external light field.

In contrast to propagating SPPs mentioned above, incident light interacts with metal nanoparticles much smaller than the incident wavelength (Fig. 1.10), leading to a plasmon that oscillates locally around the nanoparticle with a frequency known as the

LSPR [1.22]. The LSPR mode is related to SPPs at planar metal surfaces as discussed in the previous sections. However, there are some fundamental differences. For example, we have seen that SPPs are propagating, dispersive EM waves coupled to the surface electrons at the metal/dielectric interface. On the other hand, LSPRs are ***non-propagating*** excitations of the conduction electrons of metal nanostructures coupled to the external EM field, with a decay length that is 40–50 times shorter than that of SPPs. And the singular resonance frequency for LSPRs is opposite to the dispersion relations for SPPs. A full theoretical treatment of LSPRs is quite lengthy and beyond the scope of this dissertation. We briefly summarize some basic and key concepts of LSPRs in this section.

1.4.1 Simple semi-classical model

The optical properties of LSPRs in metal nanoparticles are qualitatively understood in the semi-classical model, as shown in Fig.1.10. Since the geometric size of a nanoparticle is on the order of the penetration depth of EM waves in metals ($\delta_m \approx$30nm for Ag or Au in visible regions), the excitation light is able to penetrate the nanoparticle. The EM field inside the metal nanoparticle shifts the conduction electrons collectively with respect to the fixed positive charge of the lattice ions. The electrons build up charges on the surface at one side of the nanoparticles. The electrical attraction between the negative and positive charges on the opposite side results in a restoring force. If the frequency of the excitation light is in resonance with the eigen-frequency of the collective oscillation, a small incident field leads to a strong resonant oscillation. The resonance frequency is mainly determined by the strength of the restoring force, which depends on

the separation of the surface charges, i.e. the nanoparticle size, shape, and the polarizability of the medium. And the magnitude of the oscillation depends only on the damping involved. The alternating surface charges effectively form an oscillating dipole that radiates EM waves.

1.4.2 Quasi-static approximation-Rayleigh theory

A simple *quasi-static* model is first presented, which is attributed to Lord Rayleigh, for nanoparticles neglecting retardation effects due to self-induction of EM fields. In this approach, the investigated region is much smaller than the wavelength of incident light, so the phase of the oscillating EM field is constant over the region of interest. This simple approximation describes the optical properties metal nanoparticles adequately for many purposes. The simple electrostatics can be used to calculate the response (field distribution) of a metal nanoparticle to an external EM field, in which Maxwell's equations with boundary conditions yield for the polarizability α of the metal nanoparticles [1.22]:

$$\alpha = 3V\left(\frac{\varepsilon(\omega)-\varepsilon_0}{\varepsilon(\omega)+2\varepsilon_0}\right) \tag{1.15}$$

V is the nanoparticle volume, and $\varepsilon(\omega)$ and ε_0 are the dielectric constants of metal and surrounding medium, respectively. It is apparent that the polarizability experiences a resonant enhancement under the condition that $|\varepsilon(\omega) + 2\varepsilon_0|$ is a minimum, which for the small or slowly-varying Im[ε] around the resonance simplifies to:

$$Re[\varepsilon(\omega)] = -2\varepsilon_0 \tag{1.16}$$

This relationship is called the Fronhlich condition, and the associated mode is the dipole SPR of the metal nanoparticle. The resonance frequency depends on the dielectric environment, which red-shifts as $\varepsilon(\omega)$ is increased. Metal nanoparticles are thus ideal platforms for optical sensing of refractive index changes of the surrounding environment [1.2]. Note that the magnitude of polarizability α at resonance is limited by the incomplete vanishing of the denominator of Eq. (1.15), due to Im[ε]≠ 0.

The resonance in polarizability α also implies a resonant enhancement of both the internal and dipolar EM fields. It is this field enhancement at the resonance on which many of the prominent applications of LSPRs in metal nanoparticles for optical devices and sensors. From the view point of optics, it is much more interesting to note that another consequence of the resonantly enhanced polarizability α is a concomitant enhancement in the efficiency with which a metal nanoparticle scatters and absorbs light. The corresponding scattering and absorption cross-sections, C_{sca} and C_{abs}, can be calculated through the Poynting-vector [1.23]:

$$C_{sca} = \frac{k^4}{6\pi}|\alpha|^2 = \frac{3k^4V^2}{2\pi}\left|\frac{\varepsilon(\omega)-\varepsilon_0}{\varepsilon(\omega)+2\varepsilon_0}\right|^2 \tag{1.17}$$

$$C_{abs} = kIm[\alpha] = 3kVIm[\frac{\varepsilon(\omega)-\varepsilon_0}{\varepsilon(\omega)+2\varepsilon_0}] \tag{1.18}$$

For small particles with $V \ll \lambda^3$, the absorption efficiency $C_{abs} \propto V$ dominates over the scattering efficiency with a rapid scaling of $C_{sca} \propto V^2$. Eq. (1.17) and (1.18) show that both absorption and scattering are resonantly enhanced at the dipole SPR of the metal nanoparticles when the Fronhlich condition is met ($Re[\varepsilon(\omega)] = -2\varepsilon_0$). For a spherical

nanoparticle with a volume V and dielectric function $\varepsilon = \varepsilon_1 + i\varepsilon_2$ in the *quasi-static* limit, the explicit expression for the extinction cross-section $C_{ext} = C_{abs} + C_{sca}$ is,

$$C_{ext} = 9V\frac{\omega}{c}\varepsilon_0^{3/2}[\frac{\varepsilon_2}{(\varepsilon_1+2\varepsilon_0)^2+\varepsilon_2^2}] \quad (1.19)$$

The assumption of spherical nanoparticle shape can be relaxed to more general geometries [1.23], however, the basic physics of the LSPR of a subwavelength metal nanostructure is well described by this special case.

1.4.3 Mie theory

The theory of scattering and absorption of EM radiation by a small spherical particle predicts a resonant field enhancement due to a resonance of the polarizability α. The nanoparticle acts as an electric dipole, resonantly absorbing and scattering EM fields. However, this theory of the dipole SPR is strictly valid only for small particles with dimensions below 100nm illuminated with visible or near-IR radiation. For particles of larger sizes, where the *quasi-static* approximation is not valid due to significant phase changes of the driving field over the whole particle, a rigorous electrodynamic treatment is required. In 1908, Mie was the first to develop a complete theory of the light scattering and absorption of metal spheres, in order to understand the colors of colloidal Au particles in solution. Therefore, this approach is now known as *Mie theory*, in which the scattering and extinction efficiencies are calculated by [1.23],

$$Q_{sca}^{(n)} = \frac{C_{sca}}{\pi r^2} = \frac{2}{(kr)^2}(2n+1)(|a_n|^2 + |b_n|^2) \quad (1.20)$$

$$Q_{ext}^{(n)} = \frac{C_{ext}}{\pi r^2} = \frac{2}{(kr)^2}(2n+1)Re(a_n + b_n) \tag{1.21}$$

Where k is wave-vector, r is particle radius, and a_n, b_n are the Mie coefficients,

$$a_n = \frac{\sqrt{\varepsilon_r}\psi_n(\sqrt{\varepsilon_r}kr)\psi_n'(kr) - \psi_n(kr)\psi_n'(\sqrt{\varepsilon_r}kr)}{\sqrt{\varepsilon_r}\psi_n(\sqrt{\varepsilon_r}kr)\xi_n'(kr) - \xi_n(kr)\psi_n'(\sqrt{\varepsilon_r}kr)} \tag{1.22}$$

$$b_n = \frac{\psi_n(\sqrt{\varepsilon_r}kr)\psi_n'(kr) - \sqrt{\varepsilon_r}\psi_n(kr)\psi_n'(\sqrt{\varepsilon_r}kr)}{\psi_n(\sqrt{\varepsilon_r}kr)\xi_n'(kr) - \sqrt{\varepsilon_r}\xi_n(kr)\psi_n'(\sqrt{\varepsilon_r}kr)} \tag{1.23}$$

with the Riccati-Bessel functions ψ_n and ξ_n. These equations allow the calculation of scattering cross-sections in a relatively straight forward manner using algebraic programs, such as MATHEMATICA or MATLAB. The quasi-static approximation for subwavelength particles can be recovered by a power series expansion of the absorption and scattering coefficients and retaining only the first term.

1.4.4 Applications of LSPRs in metal nanoparticles

The most well-known application of LSPRs in metal nanoparticles is to stain glass, which dates far back in history and is still used today (e.g. Ruby glass). The strong EM field around the metal nanoparticles, which can be much higher than the incident light field at the resonance frequency, is used to enhance nonlinear optical effects such as surface enhanced Raman scattering (SERS) [1.24]. Other nonlinear applications such as generation of higher harmonics or white light are currently being investigated.

In addition, since the resonance frequency of LSPRs is sensitive to the polarizability (i.e., refractive index changes) of the surrounding medium, LSPR spectroscopy offers many of the same advantages for sensing and spectroscopy as that of traditional prism-based SPR configurations, along with several additional benefits. For example, as the decay length of LSPR mode is 40–50 times shorter than that of the SPRs, the sensing

(sample) volume offered by LSPR sensors is much smaller than that of traditional SPR sensors [1.2]. Single-nanoparticle LSPR spectroscopy is another application, offering sensitivity that not only rivals, but can surpass, that of nanoparticle array-based LSPR spectroscopy [1.25].

1.5 Organization of this thesis

In this thesis, I will selectively summarize my research on SPRs in ultrathin nanostructured metals for both fundamental sciences and practical applications. Theoretical and experimental analysis will be employed to fully clarify different electromagnetic modes in ultrathin nanostructured metals with different geometric parameters, finding practical applications in three areas of plasmonic-enhanced organic photovoltaics, plasmonic color filters, and plasmonic biosensors.

In *Chapter 2*, **plasmonic transparent conducting electrodes** consisting of ultrathin two-dimensional (2D) or two one-dimensional (1D) perpendicular Ag nanogratings are investigated for organic photovoltaics with polarization-insensitive optical absorption enhancement.

In *Chapter 3*, ultrathin 1D Ag nanogratings are employed for **plasmonic subtractive color filters** with record-high transmission efficiency and other unique properties, i.e. high resolution color filtering with compact pixel size close to the optical diffraction limit, and the potential for transparent displaying.

In *Chapter 4*, a novel rapid and highly-sensitive **plasmonic bio-sensing** platform is proposed by patterning 1D nanogratings on 30nm-thick ultrathin Ag films. Excitation of

Fano resonances in the ultrathin Ag nanogratings results in transmission spectra with high amplitude, large contrast, and narrow bandwidth. An order-of-magnitude improvement in the temporal and spatial resolutions is achieved relative to state-of-the-art nanoplasmonic sensors, for comparable detection resolutions.

Fundamental studies of different electromagnetic modes in ultrathin nanostructured metal films are performed in each chapter for different applications with specific geometric parameters. Each chapter includes theoretical design and modeling, nanofabrication and optical characterization.

Finally, **conclusions** are presented and the achievements of this thesis summarized in *Chapter 5*. Future research directions will also be discussed.

References

[1.1] W. L. Barnes, A. Dereux and T. W. Ebbesen, Surface Plasmon subwavelength optics, Nature 424, 824 (2003); E. Ozbay, Plasmonics: Merging Photonics and Electronics at Nanoscale Dimensions, Science 311, 189 (2006); R. Zia, J. A. Schuller, A. Chandran, & M. L. Brongersma, Plasmonics: the next chip-scale technology. Materials Today, 9, 20 (2006).

[1.2] J. Homola, Surface Plasmon Resonance sensors for detection of chemical and biological species, Chem. Rev. 108, 462 (2008); J. N. Anker, W. P. Hall, O. Lyandres, N. C. Shah, J. Zhao and R. P. Van Duyne, Biosensing with Plasmonic Nanosensors, Nature Materials 7, 442 (2008).

[1.3] J. A. Schuller, E. S. Barnard, W. Cai, Y. C. Jun, J. S. White, M. L. Brongersma, Plasmonics for extreme light concentration and manipualtion. Nature Materials 9, 193 (2010).

[1.4] H. Raether, Surface Plasmons on Smooth and Rough Surfaces and on Gratings. (Springer-Verlag,

Berlin, 1988).

[1.5] R. H. Ritchie, Plasma losses by fast electrons in thin films. Phys. Rev.106, 874 (1957).

[1.6] T. W. Ebbesen, Surface plasmon subwavelength optics. Nature, 424, 824 (2003).

[1.7] T. W. Ebbesen, H. J. Lezec, H. F. Ghaemi, T. Thio, & P. A. Wolff, Extraordinary optical transmission through sub-wavelength hole arrays. Nature 391, 667 (1998).

[1.8] L. Martín-Moreno, F. J. García-Vidal, H. J. Lezec, K. M. Pellerin, T. Thio, J. B. Pendry, and T. W. Ebbesen, Theory of Extraordinary Optical Transmission through Subwavelength Hole Arrays. Phys. Rev. Lett. 86, 1114 (2001).

[1.9] H. A. Bethe, Theory of Diffraction by Small Holes. Phys. Rev. 66, 163 (1944).

[1.10] J. R. Sambles, Photonics: More than transparent. Nature 391, 641 (1998).

[1.11] E. N. Economou, Surface Plasmons in Thin Films. Phys. Rev. 182, 539 (1969).

[1.12] I. R. Hooper and J. R. Sambles, Coupled surface plasmon polaritons on thin metal slabs corrugated on both surfaces. Phys. Rev. B 70, 045421, (2004).

[1.13] J. Braun, B. Gompf, G. Kobiela and M. Dressel, How Holes Can Obscure the View: Suppressed Transmission through an Ultrathin Metal Film by a Subwavelength Hole Array. Phys. Rev. Lett. 103, 203901 (2009).

[1.14] J. Braun, B. Gompf, T. Weiss, M. Dressel, U. Hubner, Optical transmission through subwavelength hole arrays in ultrathin metal films. Phys. Rev. B 84, 155419 (2011).

[1.15] Q. Gan, et al., Short range surface plasmon polaritons for extraordinary low transmission through ultra-thin metal films with nanopatterns. Plasmonics, 7, 47, (2012).

[1.16] G. D'Aguanno, N. Mattiucci, A. Alu and M. J. Bloemer, Quenched optical transmission in ultrathin

subwavelength plasmonic gratings. Phys. Rev. B 83, 035426 (2011).

[1.17] S. G. Rodrigo, et al., Extraordinary optical transmission through hole arrays in optically thin metal films. Opt. Lett. 34, 4 (2009).

[1.18] P. B. Catrysse and S. Fan, Nanopatterned Metallic Films for Use As Transparent Conductive Electrodes in Optoelectronic Devices. Nano Lett. 10, 2944 (2010).

[1.19] J. J. Burke, G. I. Stegeman, and T. Tamir, Surface-polariton-like waves guided by thin, lossy metal films. Phys. Rev. B 33, 5186 (1986).

[1.20] F. Yang, J. R. Sambles, and G. W. Bradberry, Long-range surface modes supported by thin films. Phys. Rev. B 44, 5855 (1991).

[1.21] Z. Chen, I. R. Hooper, and J. R. Sambles, Strongly coupled surface plasmons on thin shallow metallic gratings. Physical Review B 77, 161405 (2008).

[1.22] S. A Maier, Plasmonics: Fundamentals and Applications. (Springer, New York, 2007).

[1.23] C. F. Bohren and D. R. Huffman, Aborption and scattering of light by small particles (Wiley, New York, 1983).

[1.24] D. L. Jeanmarie, R. P. Van Duyne Surface Raman spectroelectrochemistry, part 1: heterocyclic, aromatic, and aliphatic amines adsorbed on the anodized silver electrode. J. Electroanal. Chem. 84, 1–20 (1977).

[1.25] G. Raschke, et al., Biomolecular recognition based on single gold nanoparticle light scattering. Nano Lett. 3, 935 (2003).

Chapter 2

Transparent Conducting Electrodes employing Ultrathin Ag Nanogratings for Organic Photovoltaics

2.1 Introduction

One of the greatest challenges facing mankind is the supply of clean energy to fuel our economies. Photovoltaics have the potential to provide an unlimited source of clean energy by transferring solar energy into electricity [2.1]. Low-cost, light-weight and mechanically resilient solar power sources are of great interest for modern applications, such as electronic textiles, synthetic skin and robotics [2.2]. Compared with inorganic photovoltaics [2.3], the primary benefits of organic photovoltaics (OPVs) are often listed as low-cost, low-weight, flexibility and compatibility with reel-to-reel processing for high volume production [2.4-2.8]. Over the last decade, the power conversion efficiency (PCE) of OPVs has been steadily increasing from a few percent to about 12% [2.4-2.12], which is still much lower than that of inorganic photovoltaics (~44.4%). A significant challenge to achieving high performance OPVs lies in the low charge carrier mobility and small exciton diffusion length (1~10nm) in organic semiconducting materials [2.13]. This in turn limits the thickness of organic active layers, resulting in poor absorption of incident solar photons. Light trapping strategies have been recently employed to increase the

optical absorption without altering the thickness of organic active layers [2.14-2.26].

On the other hand, transparent conducting electrodes (TCEs) are essential components in optoelectronic devices, such as LEDs, displays, and photovoltaics. Most OPVs employ indium tin oxide (ITO) as a transparent electrode that offers high electrical conductivity and transmission of solar light in the visible and near-IR spectral regions [2.27]. However, the limited availability and increasing cost of ITO, its incompatibility with flexible substrates, and poor mechanical and chemical stability reduce its attractiveness for use in OPVs [2.28-2.30]. Hence, new materials and designs have been suggested as alternatives to ITO electrodes, including macroscopic metallic grids [2.31], Ag nanowires [2.32], randomly perforated ultrathin metal films [2.33], carbon nanotube networks [2.34], and graphene [2.35]. In addition, One-dimensional (1D) metallic nanogratings and two-dimensional (2D) metallic nanogrids have been theoretically and experimentally investigated and shown to possess high optical transmission and electrical conductivity, making them particularly attractive as TCEs [2.36]. More importantly, metallic nanostructures can excite surface plasmon resonances (SPRs) at the metal-dielectric interface [2.17-2.26], generating highly confined and enhanced electromagnetic fields. This results in an increase of optical absorption in ultrathin organic active light-harvesting layers, providing light trapping effects.

OPVs with ultrathin 1D Ag nanogratings TCEs have the potential for broadband absorption enhancement and have recently been shown to achieve stronger optical

absorption and higher PCEs than those with ITO electrodes [2.24-2.26]. Under AM 1.5 solar illumination with both transverse-magnetic (TM) and transverse-electric (TE) polarizations, a total absorption enhancement of 50% in organic active layers was reported for OPVs with 1D Ag nanogratings at top interface [2.25], and 67% for OPVs with two parallel 1D Ag nanogratings used as the top and bottom electrodes [2.24], compared to those using ITO and Ag electrodes. Enhancement of the short circuit current density J_{sc} (40%) and PCE (35%) of molecular OPVs with 1D Ag nanogratings have also been experimentally demonstrated [2.26]. However, only one specific polarization of the incident light was able to excite the plasmonic modes and achieve strong light-trapping effects [2.37]. The simultaneous optimization of the absorption enhancement for the incident light with different polarizations is difficult for 1D metallic nanostructures. Consequently, it is critical to design plasmonic TCEs that will lead to broadband and polarization-insensitive optical absorption enhancement in the organic light-harvesting layers. Plasmonic TCEs consisting of 2D metallic nanogrids may provide polarization-independent light-trapping effects and further enhance the optical absorption in these organic active layers [2.37, 2.38]. However, SPRs are not excited (and the electromagnetic fields are not enhanced) in the central part of the 2D metallic nanogrids for both polarizations, since the electric field is parallel to one of the grating directions. Hence, the central areas of the 2D metallic nanogrids do not contribute to the optical absorption enhancement in the adjacent active layers. To further enhance the optical absorption in the adjacent active layers, it is necessary to design new plasmonic

nanostructures in order to excite SPRs over the whole area, including the central part. In the current work, sandwiching the OPV structure between one top and one bottom 1D metallic nanogratings with perpendicular directions is proposed to excite plasmonic modes for both polarizations, potentially leading to larger polarization-independent absorption enhancement. In the following, we report a systematic study of the optical and electrical properties of ultrathin 1D Ag nanogratings and 2D Ag nanogrids, explore their use as plasmonic TCEs in OPVs, and optimize absorption enhancement as a function of nanograting and nanogrid's thickness, linewidth, and period.

2.2 Electrical and optical properties of ultrathin 1D Ag nanogratings and 2D Ag nanogrids

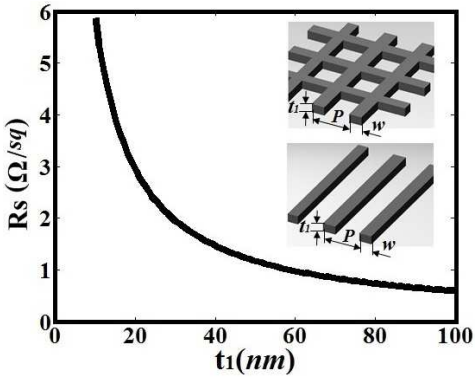

Fig. 2.1 Electrical sheet resistance of 1D Ag nanogratings or 2D Ag nanogrids (insets show the geometry with period P=300nm, line-width w=70nm) electrodes as a function of film thickness t_1.

The proposed plasmonic TCEs consisting of ultrathin Ag NGs are much thinner than typical metal films used in optical studies. As the thickness of metal film is comparable to its skin depth (tens of nanometers) at optical frequencies, the physical properties of ultrathin nanostructured metal film could be quite different from that of optically-thick metal films [2.36, 2.39]. The electrical properties of an electrode is usually described by

its sheet resistance. The 1D Ag nanogratings or 2D Ag nanogrids with line-width w, thickness t_1 and period P (see the inset of Fig. 2.1) have a sheet resistance $R_s = (\rho / t_1)(P / w)$ [2.36]. The electrical resistivity of bulk Ag film is $\rho = 1.58 \times 10^{-8} \Omega \cdot m$ [2.40]. R_s changes from 0.65 to $6.5 \Omega / sq$ as the thickness t_1 of the 1D Ag nanogratings or 2D Ag nanogrids decreases from 100 to 10nm (P=300nm and w=70nm, these values are the optimum for the largest absorption enhancement in OPV devices, as will be discussed in the following sections), as depicted in Fig. 2.1. These theoretically estimated values for R_s agree reasonably well with experimental results, and are well below that of ITO thin film (10~$20 \Omega / sq$) used as transparent electrodes [2.38].

In addition to excellent electrical conductivity, high optical transmission through the ultrathin Ag nanogratings or nanogrids is another important requirement for TCE applications. Three-dimensional (3D) finite-difference time-domain (FDTD) simulations were used to investigate the underlying physical mechanisms that determine the electronic and optical properties of ultrathin Ag nanogratings and nanogrids [2.41]. In simulations, 2D Ag NGs with line-width w, thickness t_1 and period P were positioned on a glass substrate. Fig. 2.2(a) shows 2D maps of the calculated transmission spectra for 2D Ag nanogrids as a function of the period and incident wavelength when line-width and thickness are fixed at w=70nm and t_1=30nm, respectively. The decreased transmission in region 1 (550nm<λ<900nm and 100nm<P<160nm) of Fig. 2.2(a) is caused by the high optical reflection, due to the cutoff of propagating electromagnetic modes through the vertically-oriented Ag-air-Ag waveguide [2.36].

The low transmission in region 2 (350nm<λ<450nm and 100nm<P<400nm) is attributed mainly to the intrinsic absorption in 2D Ag nanogrids, as shown in Fig. 2.2(b). Three different mechanisms may be responsible for the enhanced absorption in the 2D Ag nanogrids. For the ultrathin 2D Ag nanogrids, two single-interface surface plasmon polariton (SI-SPP) modes at top and bottom Ag/dielectric interfaces would interact with each other and lead to coupled long-range and short-range (LR- and SR-) SPP modes. The dispersion relations for LR- and SR-SPP modes in optically-thin continuous metal film can be described by the following equation [2.42,2.43]:

$$\tanh(k_2 t)(\varepsilon_{d1}\varepsilon_{d2}k_2^2 + \varepsilon_m^2 k_1 k_3) + \varepsilon_m k_2(\varepsilon_{d1}k_3 + \varepsilon_{d2}k_1) = 0 \qquad (2.1)$$

Here $k_1^2 = k_{spp}^2 - \varepsilon_{d1}k_0^2$, $k_2^2 = k_{spp}^2 - \varepsilon_m k_0^2$, $k_3^2 = k_{spp}^2 - \varepsilon_{d2}k_0^2$, $k_0 = \omega/c$ and t is the thickness of the metal film. ε_{d1}, ε_{d2} and ε_m are the dielectric constants of air, glass and Ag, respectively. For the ultrathin (30nm-thick) Ag film with an asymmetric geometry ($\varepsilon_{d1} < \varepsilon_{d2}$), only strongly damped SRSPP modes exist with anti-symmetric Ez field patterns at the top (Air/Ag) and bottom (SiO2/Ag) interfaces [2.22,2.39]. It is also known that the momentum mismatch between SPP modes and free space light can be bridged by the reciprocal vectors of periodic nanostructures $k_G = mG_x + nG_y$ ($|G_x| = |G_y| = 2\pi/P$, m and n are integers) [2.37]:

$$k_{spp} = k_0 \sin\theta + mG_x + nG_y$$

(2.2)

where θ is the incident angle. The dispersion relation of SRSPP modes can be obtained by substituting Eq. (2) into Eq. (1). The black solid curve in Fig. 2.2(b) refers to the

analytical dispersion of the SRSPP modes excited by the lowest order reciprocal vectors {(m,n)=(1,0),(-1,0),(0,1),(0,-1)} (100nm<P<230nm), which agrees well with the absorption spectra where the period is in the range of 100nm<P<220nm, since the dispersion relation of ultrathin Ag nanogrids with large duty cycles (linewith/period) can approximate that of continuous metal films.

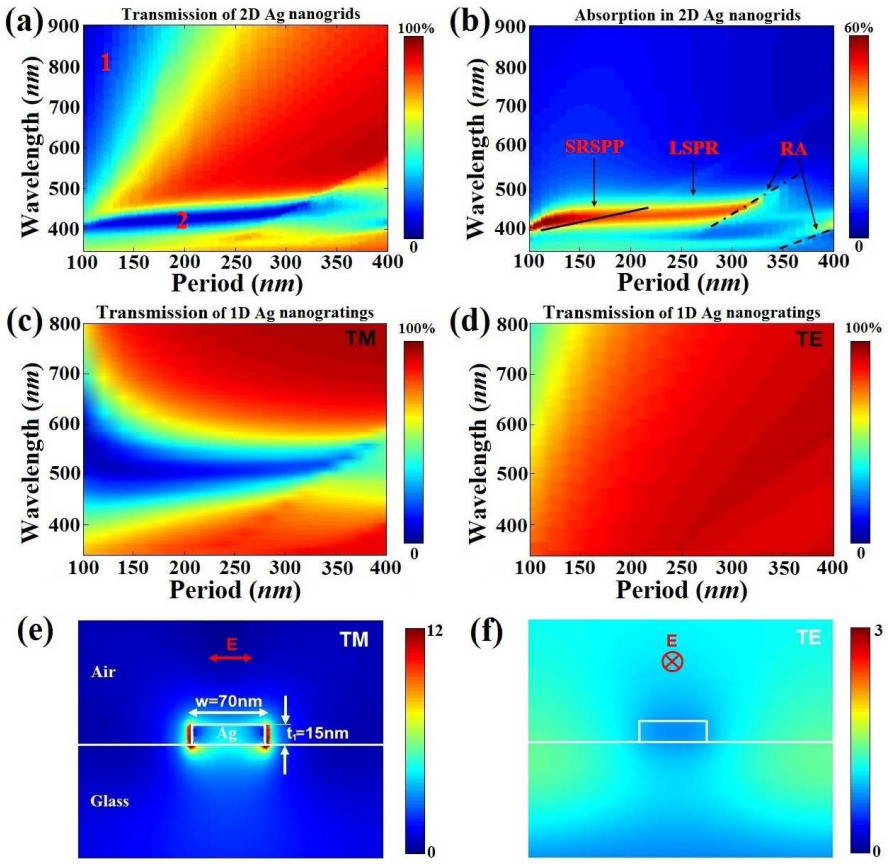

Fig. 2.2 Color maps of the calculated optical transmission (a) and absorption (b) spectra for 2D Ag nanogrids as a function of the period P and incident wavelength when line-width w and thickness t1 are fixed at 70nm and 30nm, respectively. The black solid and dash-dotted (dashed) curves in (b) refer to the analytical dispersions of SRSPP modes and Rayleigh-Wood anomaly at the Ag/glass (Ag/air) interface, respectively. Color maps of the calculated optical transmission of 1D Ag nanogratings (thickness t_1=15nm and line-width w=70nm) as a function of the period and incident wavelength, under (c) TM and (d) TE polarizations, respectively. The electric field distribution in the 15nm-thick 1D Ag nanogratings (linewidth w=70nm, period P=300nm) under (e) TM and (f) TE polarizations, respectively, when the incident wavelength is 500nm.

As the period P continues to increase from 230nm to 300nm when the line-width of

Ag NGs is fixed at w=70nm, the distance between two adjacent Ag strips becomes larger, resulting in weak inter-coupling between them [2.39]. Therefore, the absorption in 2D Ag NGs with period from 230nm to 300nm is attributed to localized-SPRs (LSPRs), which are supported by individual Ag strips [2.44]. The spectral positions of absorption band almost remain unchanged as the period of Ag NGs increases from 230nm to 300nm. This is due to the resonance wavelength of LSPRs is primarily determined by the geometry of individual Ag strips, which are fixed at w=70nm and t_1=30nm. When the momentum matching condition is satisfied ($\omega/c \cdot \sqrt{\varepsilon_d} = k_0 \sin\theta + mG_x + nG_y, \varepsilon_d$ represents the dielectric constant of the air or glass), the typical Rayleigh-Wood Anomaly (RA) occurs at Ag/glass and air/Ag interfaces [2.45], respectively, as shown by the black dash-dotted and dashed lines in Fig. 2.2(b). The ± 1 diffraction orders of incident light are scattered parallel to metal surfaces, giving rise to the strong optical absorption in Ag NGs [2.38].

3D FDTD simulations were also used to investigate the optical properties of ultrathin 1D Ag nanogratings under different polarization conditions. Fig. 2.2(c) and (d) show color maps of the calculated optical transmission spectra for 1D Ag nanogratings (line-width w_1=70nm and thickness t_1=15nm, these parameters are the optimum for absorption enhancement in OPV devices, as will be discussed in the following sections) as a function of its period and the incident wavelength, under TM and TE polarizations, respectively. In Fig. 2.2(c), the low transmission in the region of 400nm<λ<700nm and 100nm<P_1<150nm is caused by high optical reflection, which is due to the cutoff of propagating electromagnetic modes through 1D Ag nanogratings with small air openings

(30~80nm). For 1D Ag nanogratings with periods larger than 150nm, the transmission minima locate around the wavelength λ=500nm, which is attributed to LSPRs. The small decay length (tens of nanometers) of electromagnetic field in Fig. 2.2(e) demonstrates that the resonance mode is LSPR in the 15nm-thick 1D Ag nanogratings with line-width w_1=70nm and period P_1=300nm at the wavelength of 500nm. The TE-polarized incident light (Fig. 2.2(f)) transmits through the 15nm-thick 1D Ag nanogratings (line-width w_1=70nm) with high transmission (>90%) over the entire visible region. Fig. 2.2(f) clearly shows there is no resonance electromagnetic mode under TE polarization, in which case the incident light simply passes through the air openings between Ag strips.

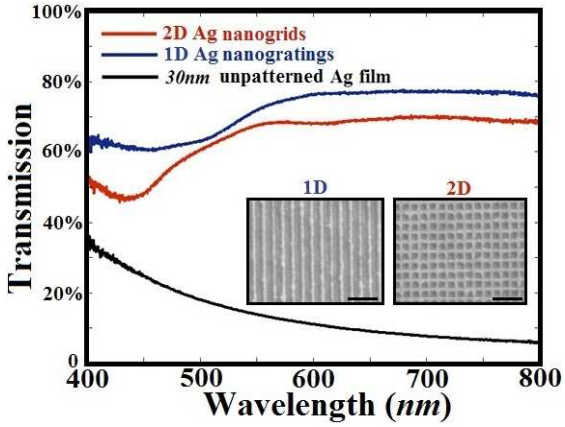

Fig. 2.3 Measured optical transmission through 1D Ag nanogratings and 2D Ag nanogrids (blue and red curves) with P=300nm, w=70nm, and t_1=30nm, and 30nm-thick unpatterned flat Ag film (black curve). Insets show SEM images of the fabricated 1D Ag nanogratings and 2D Ag nanogrids. Scale bar, 1μm.

Focused ion beam milling (FEI Dual-Beam system 235) was used to fabricate 1D nanogratings and 2D Ag nanogrids with period P=300nm and line-width w=70nm on a 30nm-thick Ag film, deposited by E-beam evaporation (Indel system) onto a glass slide (Fisherbrand). An Olympus X81 inverted microscope system was employed to measure the optical transmission of the fabricated metallic nanostructures. Fig. 2.3 shows the

normalized transmission spectra for 2D Ag nanogrids (red curve), 1D Ag nanogratings (blue curve), and 30nm-thick Ag solid films (black curve), which were measured by the fiber-based compact spectrometer (Ocean Optics USB 4000). Although there are differences between the experimental and numerical results due to fabrication and measurement errors, obvious transmission valleys are observed at a wavelength of 450nm for 2D nanogrids and 1D Ag nanogratings, which can be attributed to the excitation of LSPRs in individual Ag strips [2.38]. The optical transmission for 2D nanogrids and 1D Ag nanogratings is much higher than that of the unpatterned flat Ag film over the entire visible regions (400~800nm). While the optical transmission of the 1D Ag nanogratings is slightly higher than that of the 2D Ag nanogrids, the transmission near the resonance wavelength of 450nm is lower for the 2D Ag nanogrids, due to a higher Ag strip density of 2D Ag nanogrids (in two directions) that can contribute to LSPRs under different polarizations. The higher mode density of LSPRs can generate stronger field intensity and thus greater absorption enhancement in the adjacent OPV active layers.

2.3 Optical absorption enhancement in OPVs with 1D Ag nanogratings and 2D Ag nanogrids electrodes

Fig. 2.4(a) and (b) illustrate schematic diagrams of molecular OPVs with an ultrathin 2D Ag nanogrids electrode and two perpendicular top and bottom 1D Ag nanogratings electrodes, respectively. In Fig. 2.4(a), the 30nm-thick 2D Ag nanogrids electrode (linewidth w and period P) is positioned on a glass substrate and embedded in the poly(3,4-ethylenedioxythiophene):poly(styrenesulfonate) (PEDOT:PSS) film. Next

are the light-harvesting layers, consisting of a 10nm-thick electron donor copper phthalocyanine (CuPc) layer and a 10nm-thick electron acceptor perylene tetracarboxylic bisbenzimidazole (PTCBI) layer, followed by an 8nm-thick bathocuproine (BCP) layer that further transports electrons to the 80nm-thick bottom Ag electrode. In Fig. 2.4(b), the 15nm-thick top 1D Ag nanogratings electrode (line-width w_1 and period P_1) is positioned on a glass substrate and embedded in the PEDOT:PSS film, and is covered by the organic light-harvesting layers (10nm-thick CuPc and 10nm-thick PTCBI layers). This is followed by a 60nm-thick bottom 1D Ag nanograting (linewidth w_2 and period P_2) where the grating direction is perpendicular to the top 1D Ag nanograting embedded in the BCP layer, and on top of the 80nm-thick bottom Ag electrode.

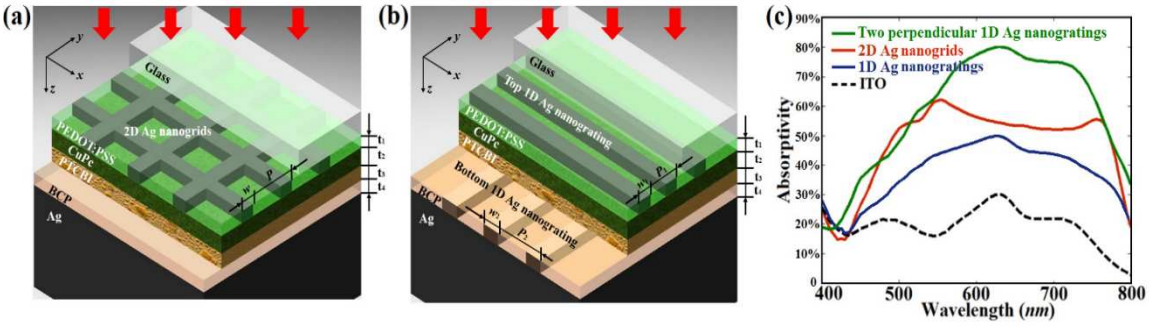

Fig. 2.4 Schematic diagrams of the proposed molecular OPVs with (a) a top 2D Ag nanogrids electrode, and (b) two perpendicular 1D Ag nanogratings electrodes. (c) Calculated optical absorption spectrum A(λ) in the organic active light-harvesting layers (CuPc:PTCBI) with a 100nm-thick ITO electrode (black dashed curve), 1D Ag nanogratings (t_1=30nm, w=70nm, and P=300nm, blue curve), 2D Ag nanogrids (t_1=30nm, w=70nm, and P=300nm, red curve), and two perpendicular 1D Ag nanogratings (w_1=w_2=70nm, P_1=P_2=300nm, green curve).

The 3D FDTD numerical method used to calculate the optical absorption in the CuPc:PTCBI light-harvesting layers allows the direct incorporation of the experimental optical constants of PEDOT:PSS, CuPc, PTCBI, BCP and Ag. The optical absorption spectrum A(λ) in the active layers is determined via FDTD simulations by calculating the

difference between the optical power incident on and transmitted through the active light-harvesting layers of the OPV device, and then normalizing it to the incident optical power. The simulations distinguish between the light that is absorbed or back-scattered by the plasmonic nanostructures and the forward propagating light. Only the light propagating past the plasmonic nanogratings and into the active light-harvesting layer is employed in calculations of the absorption of the organic layer. In the 3D FDTD simulation, a unit cell (consisting of one Ag strip with the active layers and Ag back reflectors) was used with periodic boundary conditions in the x and y directions (x=y=P) to simulate an infinite array of periodic nanogratings or nanogrids. Perfectly matched layer boundary conditions were used in the vertical z direction (z=±5μm) to prevent unphysical scattering at the edge of the simulation box. A coarse mesh size of 4nm was used over the whole simulation box. In the area of great interest (e.g. Ag nanostructures, thin active layers), the mesh size was decreased to 2nm, which is small enough to ensure the simulation accuracy. Fig. 2.4(c) shows the calculated optical absorption spectra A(λ) of the OPV active layers with two perpendicular 1D Ag nanogratings (w_1=w_2=70nm, P_1=P_2=300nm, green curve), 30nm-thick 2D Ag nanogrids (w=70nm, P=300nm, red curve) and 1D Ag nanogratings (w=70nm, P=300nm, blue curve), and 100nm-thick ITO electrodes (black dashed curve) under TM and TE polarized incident light, respectively. These geometric parameters are the optimum for achieving the strongest absorption enhancement in the organic active light-harvesting layers, as will be discussed in the following sections. The optical absorption A(λ) in the active layers with the two

perpendicular 1D Ag nanogratings is the strongest throughout most of the visible spectral region. The optical absorption A(λ) with the 2D Ag nanogrids is much stronger and broader than that with the 1D Ag nanogratings or the ITO electrode. The broadband absorption enhancement with the 2D Ag nanogrids and 1D Ag nanogratings can be attributed to the excitation of SPRs, and the formation of plasmonic cavity modes between the top 1D Ag nanogratings or 2D Ag nanogrids and the bottom Ag back reflector electrode, which can significantly confine and enhance the electromagnetic field in the ultrathin organic light-harvesting layers.

In order to elucidate the underlying physical mechanisms, different cross-sections (x-z, x-y, and y-z) of the electric field distribution for the OPVs with the top 1D Ag nanogratings, 2D Ag nanogrids and the two perpendicular 1D Ag nanogratings electrodes are depicted in Fig. 2.5(a-c), respectively, under different polarizations (electric fields along x and y axis) at the resonance wavelength λ=600nm. Fig. 2.5(a,i), (b,i) and (b,iii) show that strong electric field enhancement in the CuPc:PTCBI active layers occurs for the 1D Ag nanogratings (electric field along x axis) or 2D Ag nanogrids (electric field along x and y axis) at the resonance wavelength of 600nm. Due to the polarization-dependent excitation of SPRs in 1D Ag nanogratings, the field intensity in the active layers could only be enhanced for the incident light with the electric field perpendicular to the grating direction, as shown in the Fig. 2.5(a,i) and (a,ii). In addition, Fig. 2.5(a, iii) and (a, iv) show that the field intensity in the active layers is slightly suppressed when the electric field of the incident light is parallel to the grating direction,

since neither SPRs or waveguide modes are supported, and part of the incident light is blocked by the 1D Ag nanogratings. On the other hand, the x-z and y-z cross-sections of the electric fields in Fig. 2.5(b,i) and (b,iii) are identical, due to the polarization-independent excitation of SPRs in the 2D Ag nanogrids. Thus, as shown in Fig. 2.4(c), the optical absorption A(λ) in OPVs with the 1D Ag nanogratings is weaker than that with the 2D Ag nanogrids, in which the SPRs and plasmonic cavity modes can be excited under both x and y polarizations.

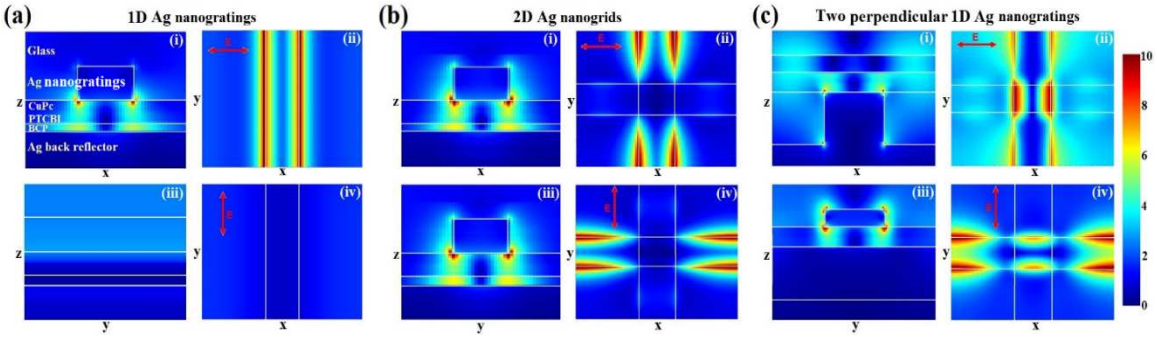

Fig. 2.5 Different cross-sections (x-z, x-y, and y-z) of the calculated electric field distributions for OPVs with (a) 1D Ag nanogratings, (b) 2D Ag nanogrids, and (c) two perpendicular 1D Ag nanogratings under different polarizations (electric fields along x or y axis) at the resonance wavelength λ=600nm.

The optical absorption in the OPV active layers with the 2D Ag nanogrids is stronger and broader than that with the 1D Ag nanogratings electrode. However, for each specific polarization (e.g., electric field along x or y axis), the x-y cross-sections in Fig. 2.5(b,ii) and (b,iv) show that the SPRs are not excited and thus the electric fields are not enhanced in the central part of the 2D Ag nanogrids under both polarizations, since the electric field is parallel to one of the grating directions. The central areas of the 2D Ag nanogrids do not contribute to the optical absorption enhancement in the adjacent active layers. To further enhance the optical absorption in the adjacent active layers, it is

necessary to design a different geometry for the Ag nanostructures in order to excite SPRs over the whole area, including the central part. Fig. 2.5(c,i) and (c,iii) clearly demonstrate that the electric fields are confined and enhanced at the bottom and top 1D Ag nanogratings under x and y polarizations, respectively. The incident light with the electric fields along the x-axis, as shown in Fig. 2.5(c,i) and (c,ii), is highly transmitted through the top ultrathin 1D Ag nanogratings (grating direction along x-axis), and then arrives at the bottom 1D Ag nanogratings (the grating direction is along y-axis, perpendicular with the top 1D Ag nanogratings), resulting in the excitation of the SPRs and absorption enhancement in the adjacent active layers. For the incident light with the electric fields along the y-axis (Fig. 2.5(c,iii) and (c,iv)), SPRs can be excited in the top 1D Ag nanogratings (along the x-axis). Due to the separately excited SPRs at the top and bottom 1D Ag nanogratings under different polarizations, the electric field is enhanced over the whole gratings area, including the central area under both polarizations, as depicted in Fig. 2.5(c,ii) and (c,iv). Therefore, the top and bottom perpendicular 1D Ag nanogratings electrodes provide much stronger optical absorption enhancement in the organic active light-harvesting layers than that calculated for the OPV active layers with the single layer 2D Ag nanogrids top electrode. Note that both LSPRs and the plasmonic cavity modes can be excited in OPVs with the top 1D Ag nanogratings, 2D Ag nanogrids and the two perpendicular 1D Ag nanogratings electrodes, as is clearly shown in Fig. 2.5 (a-c), in which these two modes couple with each other and contribute together to the absorption enhancement in the active layers.

2.4 Geometric optimizations of single-layer 2D Ag nanogrids and two perpendicular top and bottom 1D Ag nanogratings

2.4.1 Geometric optimization for 2D Ag nanogrids

In order to maximize the overall optical absorption in the active layers of OPVs with 2D Ag nanogrids, the geometric parameters of 2D Ag nanogrids need to be optimized. The solar photon flux density is defined as $\Phi_s(\lambda)=S(\lambda)\bullet\lambda/hc$, where $S(\lambda)$ is the AM1.5 solar irradiance spectrum [2.25]. The absorbed photon flux density, $A(\lambda)\bullet\Phi_s(\lambda)$, for the OPV device is determined via FDTD simulations, where $A(\lambda)$ is the optical absorption in the active layers. The total photon absorption A_{photon}, which represents the fraction of total solar photon flux density absorbed by the active layers, can be calculated using the equation [2.20]:

$$A_{photon}=\int_{\lambda_{min}}^{\lambda_{max}} A(\lambda)\cdot\Phi_s(\lambda)d\lambda \Big/ \int_{\lambda_{min}}^{\lambda_{max}} \Phi_s(\lambda)d\lambda \tag{2.3}$$

The wavelength region of interest is 400~800nm for the CuPc:PTCBI active layers [2.23-2.26]. $A_{photon\text{-}ref}$ refers to the total photon absorption for reference OPVs with 100nm-thick ITO electrodes. Fig. 2.6(a) gives the total photon absorption A_{photon} and its enhancement $(A_{photon}/A_{photon-ref}-1)\cdot 100\%$ as a function of the period (P) and thickness (t_1) of 2D Ag NGs when the line-width is fixed at w=70nm. A_{photon} with thinner Ag NGs is larger as the period changes from 100nm to 150nm, since the thinner Ag NGs have higher optical transmission in the spectral region of 650~800nm. A_{photon} continues to increase as the period of 30nm-thick Ag NGs increases up to 300nm, reaching a maximum value of 0.495. In addition, Fig. 2.6(b) shows the total photon absorption A_{photon} and its

enhancement as a function of the period P and line-width w when the thickness is fixed at t_1=30nm. The maximum A_{photon} occurs when the line-width is equal to 70nm and the period is 300nm. The maximum A_{photon} of 0.495 for OPVs with optimized 2D Ag NGs represents an enhancement of 150% compared to that using ITO electrodes. In OPV devices with the optimized plasmonic nanostructures, the enhanced electromagnetic field in the active layers is aligned with their absorption profiles. Note that A_{photon} is greatly enhanced for a large range of period P or thickness t_1 of the 2D Ag NGs, which provides good tolerance for the future fabrication of these OPV nanostrucutures.

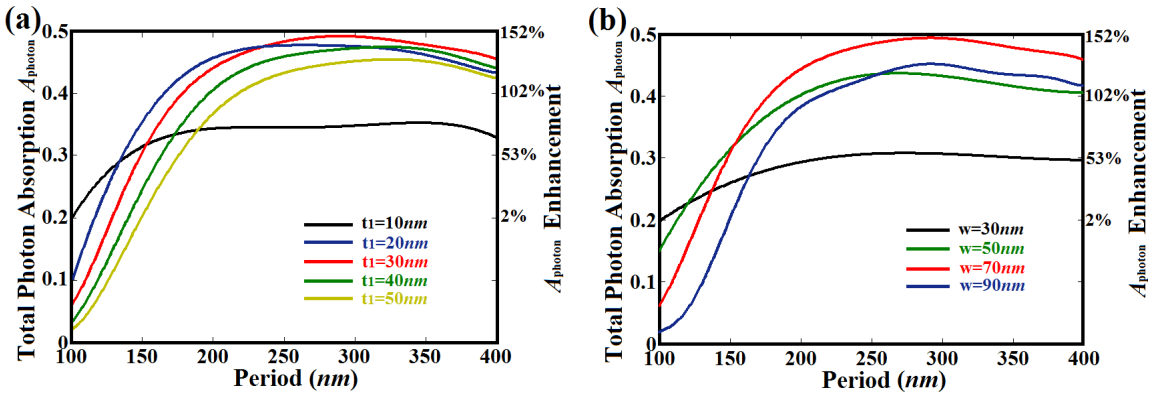

Fig. 2.6 Total photon absorption A_{photon} and its enhancement in OPVs as a function of 2D Ag NGs period P and (a) thickness t_1, when the line-width w is fixed at 70nm; or (b) line-width w, when the thickness t_1 is 30nm. All other parameters are the same as in Fig. 2.3(a).

It is worth noting that the total photon absorption A_{photon} and its enhancement with the optimized 2D Ag NGs, 0.495 and 150%, respectively, are even greater than that (0.45 and 128%) of our previous work on molecular OPVs with double 2D plasmonic nanostructures [2.23], consisting of a top Ag nanodisc array and bottom Ag nanohole array. Obviously, the OPV device with a single layer of 2D Ag NGs is much more practical and simpler than that with double 2D plasmonic nanostructures, since it would

be challenging to fabricate two different plasmonic nanostructures at the top and bottom interfaces. If the AM1.5 solar irradiance spectrum S(λ) is used as a weighting factor instead of the photon flux density Φs(λ), the overall optical absorption will be defined as the *total absorptivity* $A'_{photon} = \int_{\lambda_{min}}^{\lambda_{max}} (\frac{A_{TM}(\lambda) + A_{TE}(\lambda)}{2}) \cdot S(\lambda) d\lambda \Big/ \int_{\lambda_{min}}^{\lambda_{max}} S(\lambda) d\lambda$ [2.24, 2.25], where $A_{TM}(\lambda)$ and $A_{TE}(\lambda)$ are the absorption spectrum in the CuPc:PTCBI active layers for TM and TE polarized light, respectively, and S(λ) is the AM1.5 solar irradiance spectrum. And the total absorption enhancement is $(A'_{photon} / A'_{photon-ref} - 1) \cdot 100\%$. The total absorptivity and total absorption enhancement in active layers with the proposed 2D Ag NGs are 0.48 and 141%, respectively, which are much larger than 0.24 and 50% for that with 1D Ag nanogratings at the top interface [2.25], or even larger than the total absorption enhancement of 67% for OPVs with parallel top and bottom 1D Ag nanogratings electrodes [2.24].

2.4.2 Geometric optimization of two perpendicular top and bottom 1D Ag nanogratings

The geometric parameters of two perpendicular top and bottom 1D Ag nanogratings need also to be optimized in order to maximize the overall optical absorption enhancement in the active light-harvesting layers. Due to the complex scheme, the geometric parameters of the bottom 1D Ag nanogratings are first examined. Fig. 2.7(a) and (b) give the total photon absorption A_{photon} and its enhancement $(A_{photon} / A_{photon-ref} - 1) \cdot 100\%$ in OPVs with bottom 1D Ag nanogratings and top ITO electrodes, as a function of thickness t_4 and line-width w_2 of bottom 1D Ag nanogratings,

when period P_2 is fixed at 300nm; or period P_2, when the thickness and line-width are fixed at t_4 =60nm and w_2=70nm, respectively. In Fig. 2.7(a), A_{photon} is increased as the thickness t_4 changes from 30nm to 60nm, and line-width w_2 from 20nm to 70nm. A_{photon} reaches a maximum when the thickness and line-width are fixed at t_4 =60nm and w_2=70nm, respectively. Fig. 2.7(b) shows that the maximum A_{photon} occurs when the period is equal to 300nm.

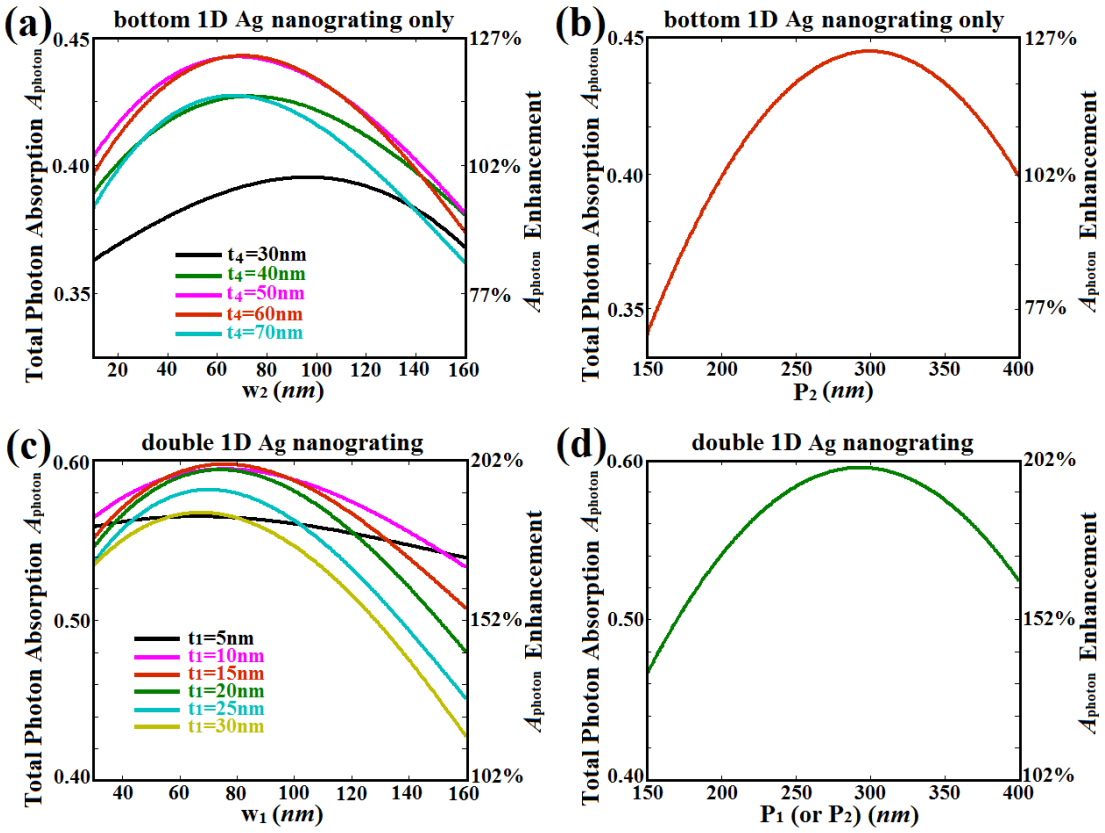

Fig. 2.7 Total photon absorption A_{photon} and its enhancement in OPVs with bottom 1D Ag nanogratings and top ITO electrodes, as a function of (a) thickness t_4 and line-width w_2 of bottom 1D Ag nanogratings, when period P_2 is fixed at 300nm, or (b) period P_2, when thickness and line-width are fixed at t_4=60nm and w_2=70nm, respectively; and in OPVs with two 1D perpendicular Ag nanogratings (bottom 1D Ag nanogratings with the optimized parameters t_4 =60nm and w_2=70nm), as a function of (c) thickness t_1 and line-width w_1 of top 1D Ag nanogratings, when period is fixed at 300nm, or (d) period P_1 (or P_2), when the thickness and linewidth are t_1 =15nm w_1=70nm, respectively.

The total photon absorption A_{photon} and its enhancement are calculated in OPVs

with two perpendicular top and bottom 1D Ag nanogratings (the bottom 1D Ag NGs with the optimized parameters t_4=60nm and w_2=70nm), as a function of thickness t_1 and line-width w_1 of top 1D Ag nanogratings, when the period is fixed at 300nm; or period P_1 (or P_2), when the thickness and line-width are t_1 =15nm w_1=70nm, respectively, as shown in Fig. 2.7(c) and (d). Fig. 2.7(c) shows that A_{photon} is increased as the thickness t_1 increases from 5nm to 15nm, and the line-width w_1 varies from 30nm to 70nm, respectively. A_{photon} decreases as the thickness t_1 or the line-width w_1 increases further, since the thicker or wider top Ag strips result in lower optical transmission. A_{photon} reaches a maximum value of 0.595 (A_{photon} enhancement 200%) when the thickness and line-width of the top 1D Ag nanogratings are t_1=15nm and w_1=70nm, respectively. Fig. 2.7(d) shows that A_{photon} and its enhancement as a function of the period P_1 (or P_2) of 1D Ag nanogratings when the thickness and linewidth of top and bottom 1D Ag nanogratings are set at their optimized values. The maximum A_{photon} occurs when the period is 300nm. A_{photon} is greatly enhanced over a large range of geometric parameters of the top and bottom 1D Ag nanogratings, indicating once more a good tolerance for future fabrication of these nanostructures. Note that A_{photon} and its enhancement with the optimized two perpendicular 1D Ag nanogratings, 0.595 and 200%, respectively, are much greater than those achieved in previous designs, including molecular OPVs with ultrathin 2D Ag NGs (0.495 and 150%). However, the fabrication of the OPV devices with the two perpendicular top and bottom 1D Ag nanogratings would probably be more challenging than that with a single layer top 2D Ag nanogrids [2.46].

2.5 Angular dependence of the optical absorption enhancement

In order to prevent the usage of expensive mechanical tracking systems that are often used to align the solar panel surface normal to the incident light, the solar cell needs a broad angular response [2.47-2.50]. Thus, it is necessary to investigate the angular dependence of the optical absorption enhancement in the proposed OPV nanostructures. The total photon absorption Aphoton and its enhancement $(A_{photon}/A_{photon-ref}-1)\cdot 100\%$ for OPVs with the optimized single-layer 2D Ag nanogrids decreased from 0.495 and 150% for normal incidence ($\theta=0^0$) to 0.152 and 30.6% for an incident angles of $\theta=60^0$, as red solid and blue dashed curves as shown in Fig. 2.8(a), respectively. Compared with our previous designs (polymeric OPVs with a top Ag nanodisc array and a flat Ag back reflector electrode), the A_{photon} enhancement with the 2D Ag nanogrids is stronger either under normal incidence (e.g. 150% v.s. 31.2% at $\theta=0^0$) or under larger incident angles (e.g. 30.6% v.s. 28.7% at $\theta=60^0$). In addition, A_{photon} and its enhancement for OPVs with the optimized two perpendicular top and bottom 1D Ag nanogratings decreased from 0.595 and 200% for normal incidence to 0.164 and 41% under 60^o incident angles (red solid and blue dashed curves in Fig. 2.8(b)). Compared with OPVs with the 2D Ag nanogrids, A_{photon} enhancement with the perpendicular top and bottom 1D Ag nanogratings is further increased either under normal incidence (e.g. 200% v.s. 150% at $\theta=0^0$) or large incident angles (e.g. 41% v.s. 30.6% at $\theta=60^0$).

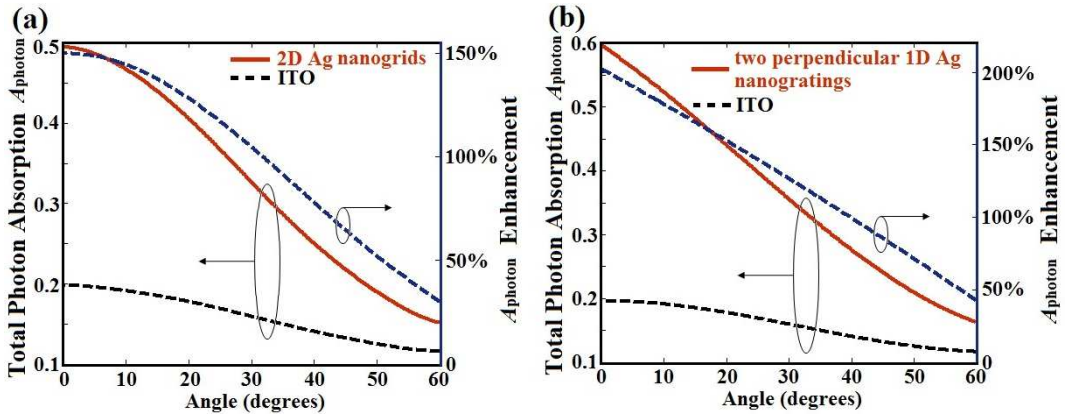

Fig. 2.8 Angular dependence of the total photon absorption for molecular OPVs with optimized (a) single-layer 2D Ag nanogrids; and (b) two perpendicular 1D Ag nanogratings electrodes (A_{photon}, red solid curves), and ITO electrodes ($A_{photon-ref}$, black dashed curves), and A_{photon} enhancement (blue dashed curves).

2.6 Summary

In summary, we have systematically studied the optical and electrical properties of novel plasmonic transparent electrode consisting of ultrathin 1D Ag nanogratings and 2D Ag nanogrids, with a calculated sheet resistance <10 Ω/sq. The underlying physical mechanisms that determine the optical properties of the ultrathin 1D Ag nanogratings and 2D Ag nanogrids have been investigated and delineated. Strong optical absorption enhancement in the OPV organic light-harvesting layers with 2D nanogrids, and two perpendicular top and bottom 1D Ag nanogratings electrodes have been calculated. The total photon absorption A_{photon} was increased to quite high values of 0.495 and 0.595 for the optimized single-layer 2D Ag nanogrids and two-layer perpendicular top and bottom 1D Ag nanogratings, respectively. This represents enhancements in optical absorption of 150% and 200%, respectively, compared to that of a reference OPV with a conventional ITO electrode. The fabrication of the OPV device with the two perpendicular top and bottom 1D Ag nanogratings, which provides the strongest absorption enhancement, may

prove to be more challenging than that with a single layer 2D Ag nanogrids. These design principles are quite general and can be extended to other organic, inorganic, and organic/inorganic hybrid optoelectronic devices with thin active layers that are adjacent to the plasmonic nanostructures. Since plasmonic resonances are very sensitive to the geometric parameters of the metallic nanostructures and the dielectric constants of the surrounding materials, careful consideration is required for each specific design and material used.

References

[2.1] M. A. Green, Third generation photovoltaics: Solar cells for 2020 and beyond, Physica E 14, 65 (2002).

[2.2] D. J. Lipomi, Z. Bao, “Stretchable, elastic materials and devices for solar energy conversion”, Energy Environ. Sci. 4, 3314 (2011).

[2.3] M. A. Green, “Recent developments in photovoltaics”, Sol. Energy 76, 3 (2004).

[2.4] C. W. Tang, “Two-layer organic photovoltaic cell”, Appl. Phys. Lett. 48, 183 (1986).

[2.5] P. Peumans, S. Uchida, and S. R. Forrest, “Efficient bulk heterojunction photovoltaic cells using small-molecular-weight organic thin films”, Nature 425, 158 (2003).

[2.6] G. Li, V. Shrotriya, J. Huang, Y. Yao, T. Moriarty, K. Emery, and Y. Yang, “High-efficiency solution processable polymer photovoltaic cells by self-organization of polymer blends”, Nat. Materials 4, 864 (2005).

[2.7] J. Y. Kim, K. Lee, N. E. Coates, D. Moses, T.-Q. Nguyen, M. Dante, and A. J. Heeger, “Efficient tandem polymer solar cells fabricated by all-solution processing”, Science 317, 222 (2007).

[2.8] M. Kaltenbrunner, M. S. White, E. D. Głowacki, T. Sekitani, T. Someya, N. S. Sariciftci & S. Bauer "Ultrathin and lightweight organic solar cells with high flexibility", Nat. Comm. 3, 770 (2012).

[2.9] H.-Y. Chen, J. Hou, S. Zhang, Y. Liang, G. Yang, Y. Yang, L. Yu, Y. Wu and G. Li, "Polymer solar cells with enhanced open-circuit voltage and efficiency", Nat. Photonics 3, 649 (2009).

[2.10] Y. Sun, G. C. Welch, W. L. Leong, C. J. Takacs, G. C. Bazan and A. J. Heeger, "Solution-processed small-molecule solar cells with 6.7% efficiency", Nat. Materials 37, 194 (2012).

[2.11] J. You, L. Dou, K. Yoshimura, T. Kato, K. Ohya, T. Moriarty, K. Emery, C.-C. Chen, J. Gao, G. Li & Y. Yang, "A polymer tandem solar cell with 10.6% power conversion efficiency", Nat. Comm. 4, 1446 (2013).

[2.12] http://www.nrel.gov/ncpv/images/efficiency_chart.jpg

[2.13] P. E. Shaw, A. Ruseckas, I. D. W. Samuel, "Exciton Diffusion Measurements in Poly(3-hexylthiophene)", Adv. Mater. 20, 3516 (2008).

[2.14] S.-B. Rim , S. Zhao , S. R. Scully , M. D. McGehee , P. Peumans , "An effective light trapping configuration for thin-film solar cells", Appl. Phys. Lett 91, 243501 (2007).

[2.15] K. Liu, B. Zeng, H. Song, Q. Gan, F. J. Bartoli, Z. H. Kafafi,, "Super absorption of ultra-thin organic photovoltaic films", Opt. Comm. 314, 48 (2014).

[2.16] D.-H. Ko , J. R. Tumbleston , L. Zhang , S. Williams , J. M. DeSimone , R. Lopez , E. T. Samulski , "Photonic Crystal Geometry for Organic Solar Cells", Nano Lett. 9, 2742 (2009).

[2.17] H. A. Atwater, and A. Polman, "Plasmonics for improved photovoltaic devices", Nat. Mater. 9, 205 (2010).

[2.18] R. A. Pala, J. White, E. Barnard, J. Liu, M. L. Brongersma, "Design of Plasmonic Thin-Film Solar

Cells with Broadband Absorption Enhancements", Adv. Mater. 21, 3504 (2009).

[2.19] W. Wang, S. Wu, K. Reinhardt, Y. Lu, S. Chen, "Broadband Light Absorption Enhancement in Thin-Film Silicon Solar Cells", Nano Lett. 10, 2012 (2010).

[2.20] B. Zeng, Q. Gan, Z. H. Kafafi, and F. J. Bartoli, "Polymeric photovoltaics with various metallic plasmonic nanostructures", J. Appl. Phys. 113, 063109 (2013).

[2.21] A. E. Ostfeld and D. Pacifici, "Plasmonic concentrators for enhanced light absorption in ultrathin film organic photovoltaics", Appl. Phys. Lett. 98, 113112 (2011).

[2.22] W. Bai, Q. Gan, G. Song, L. Chen, Z. Kafafi, and F. Bartoli, "Broadband Short-Range Surface Plasmon Structures for Absorption Enhancement in Organic Photovoltaics", Optics Express 18, A620 (2010).

[2.23] W. Bai, Q. Gan, G. Song, L. Chen, Z. Kafafi, and F. Bartoli, "Double plasmonic structure design for broadband absorption enhancement in molecular organic solar cells", Journal of Photonics for Energy 1, 011121 (2011).

[2.4] M. A. Sefunc, A. K. Okyay, and H. V. Demir, "Volumetric plasmonic resonator architechture for thin film solar cells", Appl. Phys. Lett. 98, 093117 (2011).

[2.25] C. Min, J. Li, G. Veronis, J. Lee, S. Fan, and P. Peumans, "Enhancement of optical absorption in thin-film organic solar cells through the excitation of plasmonic modes in metallic gratings", Appl. Phys. Lett. 96, 133302 (2010).

[2.26] M. Kang , T. Xu , H. Park , X. Luo , and L. Guo, "Efficiency Enhancement of Organic Solar Cells Using Transparent Plasmonic Ag Nanowire Electrodes", Adv. Mater. 22, 4378 (2010).

[2.27] K. Sreenivas, T. S. Rao, M. Abhai, C. Subhash, "Preparation and characterization of rf sputtered

indium tin oxide films", J. Appl. Phys. 57, 384 (1985).

[2.28] G. Gu, V. Bulovic, P. E. Burrows, S. R. Forrest, M. E. Thompson, "Transparent organic light emitting devices", Appl. Phys. Lett. 68, 2606 (1996).

[2.29] Z. Chen, B. Cotterel, W. Wang, E. Guenther, S.-J. Chua, "A mechanical assessment of flexible optoelectronic devices", Thin Solid Films 394, 202 (2001).

[2.30] W. S. Jahang, A. H. Francis, H. Moon, J. I. Nanos, M. D. Curtis, "Is indium tin oxide a suitable electrode in organic solar cells? Photovoltaic properties of interfaces in organic p/n junction photodiodes", Appl. Phys. Lett. 88, 093504 (2006).

[2.31] K. Tvingstedt, O. Inganas, "Electrode Grids for ITO-free Organic Photovoltaic Devices", Adv. Mater. 19, 2893 (2007).

[2.32] J. -Y. Lee, S. T. Connor, Y. Cui, P. Peumans, "Solution-Processed Metal Nanowire Mesh Transparent Electrodes", Nano Lett. 8, 689 (2008).

[2.33] H. M. Stec , R. J. Williams, T. S. Jones, and R. A. Hatton, "Ultrathin Transparent Au Electrodes for Organic Photovoltaics Fabricated Using a Mixed Mono-Molecular Nucleation Layer", Adv. Funct. Mater. 21, 1709 (2011).

[2.34] M. W. Rowell, M. A. Topinka, M. D. McGehee, H.-J. Prall, G. Dennler, N. S. Sariciftci, L. Hu, G. Gruner, "Organic solar cells with carbon nanotube network electrodes", Appl. Phys. Lett. 88, 233506 (2006).

[2.35] K. S. Kim, et al., "Large-scale pattern growth of graphene films for stretchable transparent electrodes", Nature 457, 706 (2009).

[2.36] P. B. Catrysse and S. Fan, "Nanopatterned Metallic Films for Use As Transparent Conductive

Electrodes in Optoelectronic Devices", Nano Lett. 10, 2944 (2010).

[2.37] H. Raether, Surface Plasmons on Smooth and Rough Surfaces and on Gratings (Springer-Verlag, Berlin, 1988).

[2.38] J. Groep, P. Spinelli, and A.Polman, "Transparent Conducting Silver Nanowire Networks", Nano Lett. 12, 3138 (2012).

[2.39] B. Zeng, Y. Gao, and F. J. Bartoli, "Ultrathin nanostructured metals for highly transmissive plasmonic subtractive color filters", Sci. Rep. 3, 2840 (2013).

[2.40] E. D. Palik, Handbook of Optical Constants of Solids (Academic Press: Orlando, FL, 1985).

[2.41] FDTD Solution Release 7.5 (2011), Lumerical Solutions Inc.

[2.42] J. J. Burke, G. I. Stegeman, and T. Tamir, "Surface-polariton-like waves guided by thin, lossy metal films", Phys. Rev. B 33, 5186 (1986).

[2.43] J. Braun, B. Gompf, G. Kobiela, and M. Dressel, "How Holes Can Obscure the View: Suppressed Transmission through an Ultrathin Metal Film by a Subwavelength Hole Array", Phys. Rev. Lett. 103, 203901 (2009).

[2.44] G. D'Aguanno, N. Mattiucci, A. Alu, and M. J. Bloemer, "Quenched optical transmission in ultrathin subwavelength plasmonic gratings", Phys. Rev. B 83, 035426 (2011).

[2.45] R. W. Wood, "On a remarkable case of uneven distribution of light in a diffraction grating spectrum", Philos. Mag. 4, 396 (1902).

[2.46] X. Li , et. al, "Dual Plasmonic Nanostructures for High Performance Inverted Organic Solar Cells", Adv. Mater. 24, 3046 (2012).

[2.47] N. Liu, M. Mesch, T. Weiss, M. Hentschel, and H. Giessen, "Infrared perfect absorber and its

application as plasmonic sensor", Nano Lett. 10, 2342 (2010).

[2.48] C. Watts, X. Liu, W. Padilla, "Metamaterials Electromagnetic wave absorbers", Adv. Mater. 24, OP98 (2012).

[2.49] K. Aydin, V. E. Ferry, R. M. Briggs, and H. A. Atwater, "Broadband polarization-independent resonant light absorption using ultrathin plasmonic supper absorbers", Nat. Comm. 2, 517 (2011).

[2.50] S. Y. Chou, W. Ding, "Ultrathin, high-efficiency, broad-band, omni-acceptance, organic solar cells enhanced by plasmonic cavity with subwavelength hole array", Opt. Exp. 21, A60 (2013).

Chapter 3

Ultrathin Nanostructured Metals for Highly Transmissive Plasmonic Subtractive Color Filters

In this chapter, nanopatterned ultrathin metal films are investigated for the use as highly transmissive plasmonic subtractive color filter arrays with sub-micrometer spatial resolution. This represents an attractive approach for on-chip color filters, which are vital

components for displays, image sensors, digital photography, projectors and other optical measurement instrumentation.

3.1 Introduction

Previous approaches based on traditional colorant filters employ organic dyes or chemical pigments that are vulnerable to processing chemicals, and undergo performance degradation under long-duration ultraviolet irradiation or at high temperatures. Furthermore, highly-accurate lithographic alignment techniques are required to pattern each type of pixel in a large-area array, significantly increasing fabrication complexity and cost. Plate-like dielectric deflectors have recently been proposed [3.1], but this scheme suffers from intrinsic limitations due to poor color purity, since the deflector covers only half of the total area. Nanoplasmonic color filters have been proposed recently as a promising means of overcoming the above limitations [3.2-3.11].

The well-known extraordinary optical transmission (EOT) phenomenon [3.12-3.14], observed in a single optically-thick metal film perforated with a periodic subwavelength hole array, has been extensively studied for additive color filtering (ACF) applications over the past decade. Such plasmonic color filters reject the entire visible spectrum except for selective transmission bands that are associated with the excitation of surface plasmon polaritons (SPPs) [3.2, 3.6-3.14]. These EOT transmission bands can be spectrally tuned throughout the entire visible spectrum by simply adjusting geometric parameters, such as the periodicity, shape and size of nanoholes, leading to the high color tunability. Single-layer nanostructured metals also have significant advantages over

colorant-based materials due to their ease of fabrication and device integration, and greater reliability under high temperature, humidity and long-term radiation exposure [3.2, 3.7-3.9]. Despite these advantages, the low transmission efficiency of hole-array plasmonic ACFs (~30% at visible wavelengths) remains a bottleneck that limits their commercial applications [3.8]. Recently, peak transmission efficiencies of 40~50% were achieved in the state-of-art hole-array plasmonic ACFs [3.2], but at the expense of spectral bandwidth and color crosstalk. This transmission efficiency is still far below that of commercial image sensors (~80%, FUJIFILM Electronic materials U.S.A., Inc.). Plasmonic ACFs formed by metal-insulator-metal (MIM) or metal-dielectric (MD) waveguide nanoresonators have achieved high transmission efficiencies of 50~80% [3.3, 3.10, 3.11], but are not suitable for low-cost nanofabrication and device integration due to their complex multilayer designs. There is still a critical need for novel plasmonic color filters with both high transmission efficiency and simple cost-effective architectures.

The present work explores the counter-intuitive extraordinary low transmission (ELT) phenomenon in a single optically-thin (30nm-thick) Ag film patterned with one dimensional (1D) nanogratings [3.15-3.21], and reports a novel approach to achieving plasmonic subtractive color filters (SCFs) with unusually high transmission of 60~70%. In this subtractive color filtering scheme, specific colors (i.e. cyan, magenta, and yellow, CMY) are generated by removing their complementary components (i.e. red, green, and blue, RGB) from the visible spectrum. Due to their broad passbands with twice the photon throughput of narrowband ACFs, SCFs have the major advantages of better light

transmission and a stronger color signal, and have been successfully used in image sensors for years [3.22, 3.23]. Unfortunately, highly efficient plasmonic SCFs have not been previously proposed or realized. The present work exploits recent advances in thin-film plasmonic nanostructures, and achieves for the first time, plasmonic SCFs with high transmission efficiency close to that for commercial image sensors. The transmission minima of plasmonic SCFs, corresponding to the ELT resonances, can be arbitrarily tuned to specific wavelengths across the entire visible region by simply varying the geometric parameters of nanogratings. Moreover, owing to short-range interactions of SPPs between nearest-neighbor nanostructures at the ELT resonances, plasmonic SCFs can efficiently filter colors with only a few (even only two) nanoslits, yielding ultracompact pixel sizes close to the optical diffraction limit (~λ/2, i.e. 200~350nm) that determines the highest achievable optical resolution [3.4, 3.24]. Therefore, plasmonic SCFs are capable of providing even smaller pixel sizes than those currently achieved in commercial image sensors ($1.12\times1.12\mu m^2$, Sony Corp.). In addition, plasmonic SCFs with ultrathin 1D nanogratings considered here can be easily generalized to two-dimensional (2D) nanostructures (i.e. nanoholes, nanosquares) to achieve polarization-independent operation. It should be noted, however, that the polarization-dependent color filtering function of 1D plasmonic SCFs, which can either filter transverse-magnetic (TM) polarized illumination or function as transparent windows under transverse-electric (TE) polarization, makes them highly attractive for next-generation transparent displays [3.25, 3.26].

3.2 Ultrathin plasmonic subtractive color filters based on Extraordinary Low Transmission

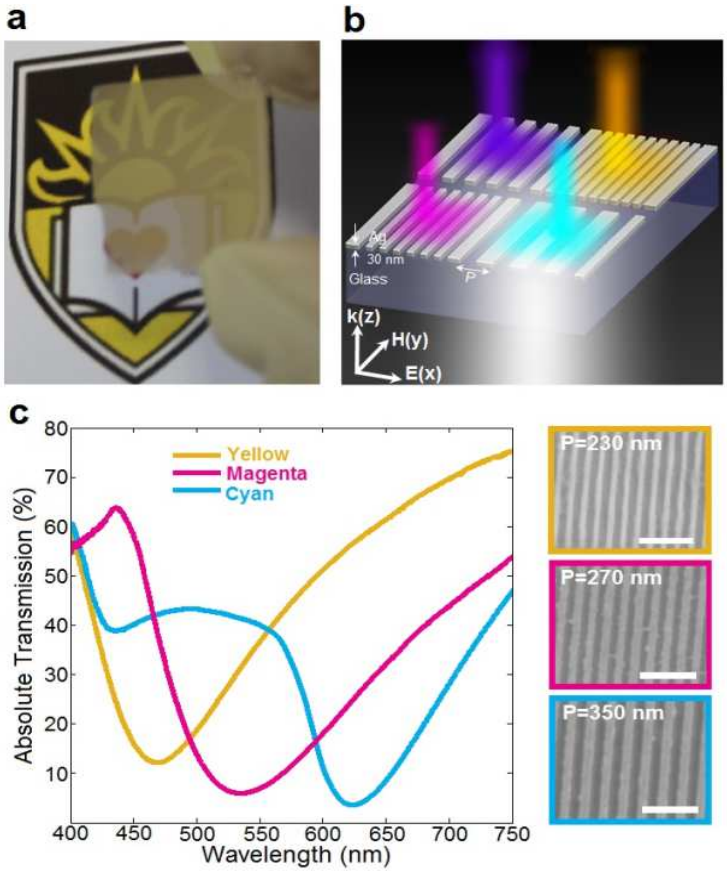

Fig. 3.1 Plasmonic subtractive color filters formed by ultrathin Ag nanogratings. (a) A photograph of a 30nm-thick semi-transparent Ag film deposited on a microscope glass slide, showing a Lehigh University logo in the background. (b) Schematic of the proposed plasmonic SCFs. (c) Measured TM transmission spectra for yellow, magenta and cyan plasmonic SCFs consisting of 30nm-thick Ag nanogratings with periods of 230*nm*, 270*nm* and 350*nm*, respectively. Right column shows SEM images of the fabricated nanogratings. Scale bars, 1μm.

Fig. 3.1(a) is a photograph of a 30nm-thick Ag film deposited on a standard microscope glass slide. The background pattern can be clearly seen through the semi-transparent Ag film. The Ag film thickness is determined to be 29.8nm. Its optical constants are noticeably different from those of an optically thick (350nm) Ag film (see Fig. 3.2).

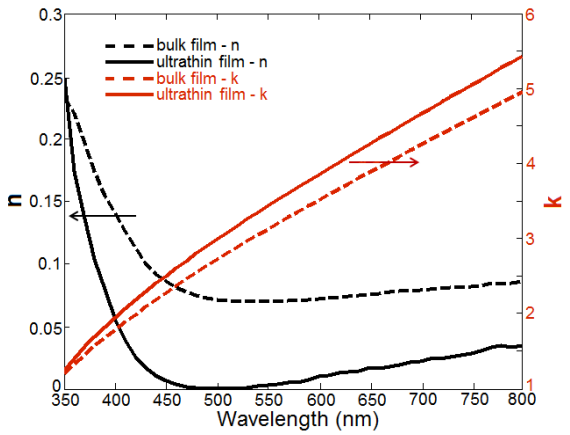

Fig. 3.2 Measured optical constants of ultrathin (30nm thick) and bulk (350nm thick) Ag films.

A schematic diagram of the proposed plasmonic SCFs is shown in Fig. 3.1(b), where 1D nanogratings with different periods are patterned on the ultrathin Ag film. For normally incident light polarized along the x-direction (TM polarization), the absorption and reflection are enhanced at the resonance wavelength [3.15-3.21], leading to a transmission minimum, which is opposite to the well-known EOT phenomenon that exhibits enhanced transmission peak at the resonance wavelength in optically-thick nanostructured metal films [3.12-3.14]. By simply varying the period of nanopatterns on the ultrathin metal film, arbitrary colors may be subtracted from broadband white light. The key features of this design, which contains only a single ultrathin nanopatterned metal layer, are their simple design rules, ease of fabrication, and scalable throughput by means of large-area nanofabrication methods, such as nanoimprint lithography or optical interference lithography [3.27-3.29]. For a proof-of-principle experiment, nanogratings with different periods were fabricated using focus ion beam (FIB) milling. The right column in Fig. 3.1(c) shows scanning electron microscopy (SEM) images of the

fabricated nanogratings with three different periods (230nm, 270nm and 350nm). The duty cycle of nanogratings was set as 0.5 for convenience. Fig. 3.1(c) presents measured transmission spectra of the cyan (P=350nm), magenta (P=270nm) and yellow (P=230nm) plasmonic SCFs under TM-polarization, with transmission minima that are positioned in red, green, and blue spectral regions, respectively. Note that the observed absolute peak transmission, 60~70% in the visible region, represent an unusually high transmission efficiency for such structures [3.2, 3.3, 3.6-3.14]. The full-widths at half maximum (FWHM) of the stop-bands are approximately 100 nm for yellow and cyan SCFs, and 160nm for magenta SCFs, which are comparable to the pass-band width for state-of-the-art plasmonic ACFs [3.2, 3.3].

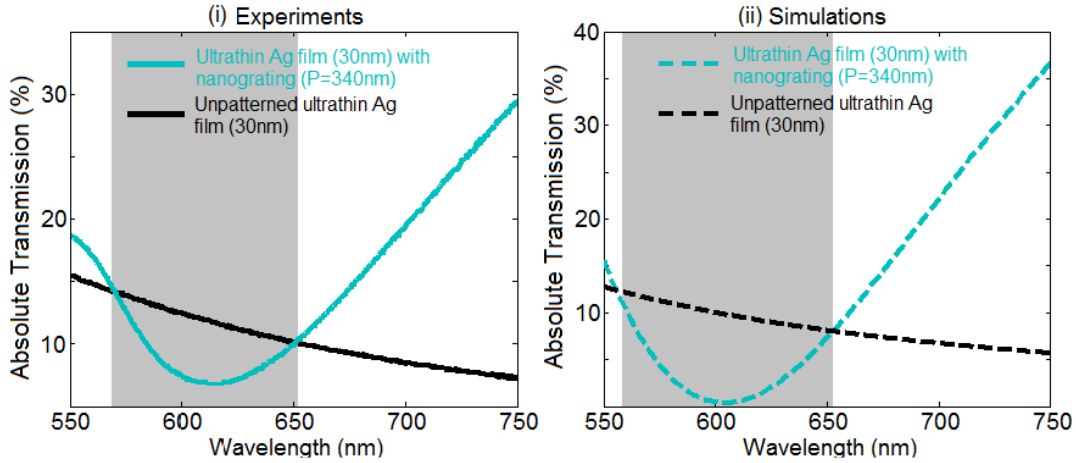

Fig. 3.3 Extraordinary low transmission in ultrathin Ag nanogratings. Measured (i) and simulated (ii) TM transmission spectra through 30nm-thick Ag films with nanogratings of period P=340nm (cyan curves) compared to that for the unpatterned film (black curves). The ELT phenomenon occurs in the gray spectral region.

The solid cyan and black curves in Fig. 3.3 represent the measured transmission spectra under TM-polarized illumination through 30nm-thick Ag films with and without 340nm-period nanogratings, respectively. The intriguing characteristic of ELT

phenomenon is that the optical transmission through the ultrathin Ag film patterned with nanogratings (solid or dashed cyan curves) is lower than that through the unpatterned Ag film (10~12%, solid or dashed black curves) over a broad spectral range (gray region), even though 50% of the highly-reflective Ag is removed in the nanogratings compared to the unpatterned Ag film. The 6% experimental transmission minimum centered at a wavelength of 610nm is consistent with the finite-difference time-domain (FDTD) simulations (dashed cyan curves). It should be noted that the calculated transmission minimum is close to zero (0.39%), indicating that the incident light can in principle be completely blocked by the ultrathin nanogratings at the resonance wavelength. Differences between the experimental and numerical results can be attributed to the nonparallel incident light employed in the measurement, nanofabrication defects, surface roughness, and finite periodicity. The simulated transmission (T), reflection (R) and absorption (A) for this 30nm-thick Ag nanograting with P=340nm are 0.39%, 85.5% and 14.11%, respectively, at the ELT resonance wavelength. Note that T=10.9%, R=82.86% and A=6.24% for the case of the unpatterned film. The increased reflection and absorption result in the suppression of the transmission in ultrathin Ag nanogratings.

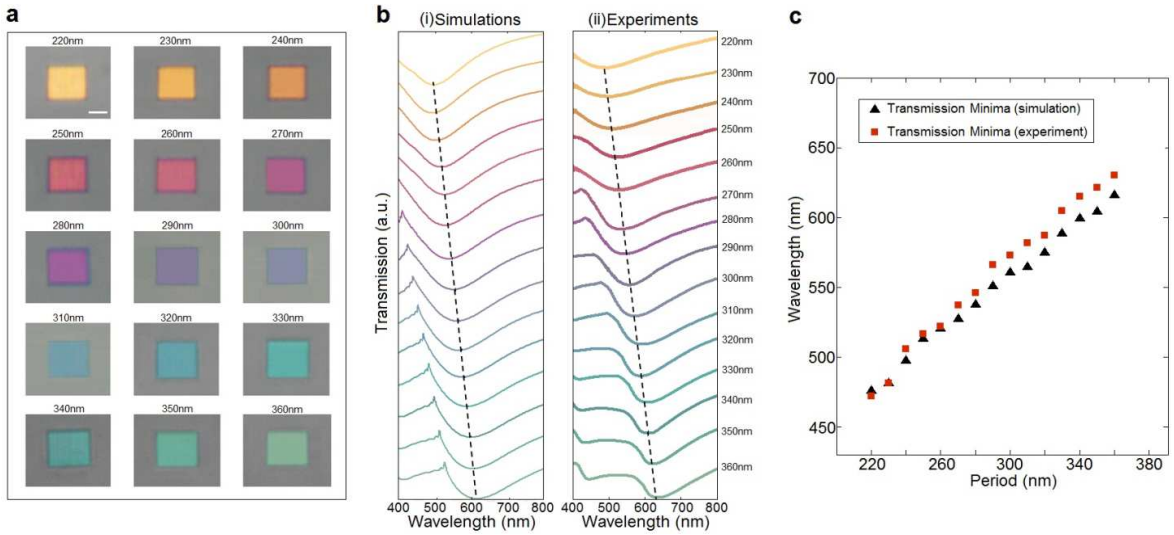

Fig. 3.4 Optical micrographs and spectral analyses of ultrathin plasmonic subtractive color filters with varying periods. (a) The full palette of transmitted subtractive colors from yellow to cyan is revealed in above $10\times10\mu m^2$ squares under TM-polarized white light illumination, as the nanograting period changes from 220nm to 360nm in 10nm increments. The scale bar is 5μm. (b) Simulated (i) and experimental (ii) TM transmission spectra of nanogratings with periods ranging from 220nm to 360nm. The trend lines (dashed black lines) approximate the change of the transmission minima with varying grating period. (c) Correlation between transmission minima observed in the experimental (red square) and simulation (black triangle) data.

In order to achieve a full palette of subtractive colors that spans the entire visible region, the period of nanogratings was varied from 220nm to 360nm in 10nm increments. All the fabricated nanogratings have the same dimensions of $10\times10\mu m^2$. Fig. 3.4(a) shows the corresponding optical microscope images (from yellow to cyan) of fifteen square-shaped plasmonic SCFs illuminated by TM-polarized white light. At the same time, these nanostructures strongly transmit TE-polarized light, which distinctly contrasts with that of previous optically-thick plasmonic ACFs or wire-grid polarizers [3.3, 3.30]. The polarization-dependent color filtering effects in plasmonic SCFs arise from the polarization-dependent excitation of SPPs in 1D Ag nanogratings. This unique feature indicates that the proposed plasmonic SCFs can function either as SCFs or highly

transparent windows under different polarizations, which has potential applications in transparent displays [3.25, 3.26]. Fig. 3.4(b) presents transmission spectra of the plasmonic SCFs, exhibiting transmission minima that are tuned across the visible spectrum by varying the period from 220nm to 360nm. FDTD simulations (i) agree reasonably well with the experimental results (ii). The trend lines (dashed black lines) approximate the variation of transmission minima from 470nm to 620nm as the periods change from 220nm to 360nm. The variation of the transmission minima with period are further illustrated in Fig. 3.4(c), showing a nearly linear relation between the resonance wavelengths and nanograting period. That arbitrary subtractive colors can be obtained by simply varying the grating period is highly advantageous. This could extend the operational range of conventional colorant color filters that do not scale well to more than three spectral bands, making them especially attractive for multispectral imaging applications [3.6].

3.3 Physical mechanisms responsible for Extraordinary Low Transmission

The phenomenon of ELT in ultrathin nanopatterned metal film has been the subject of numerous fundamental investigations since 2009 [3.15-3.21]. Although there is a general agreement that SPPs play a crucial role in ELT, recent studies have reported different conclusions regarding whether the suppression of transmission is due to the excitation of short-range SPPs (SRSPPs) or localized SPPs (LSPPs) [3.17, 3.18]. To elucidate the physical mechanisms underlying the ELT phenomenon, we model the

optical properties of ultrathin Ag nanogratings via FDTD simulations. 2D maps of the calculated transmission, absorption and reflection for 30nm-thick Ag nanogratings are shown in Fig. 3.5 (a)-(c), respectively, as a function of the incident wavelength and grating period. The duty cycle of nanogratings is set as 0.5. The low-transmission band in Fig. 3.5(a) shifts to longer wavelengths as the grating period increases.

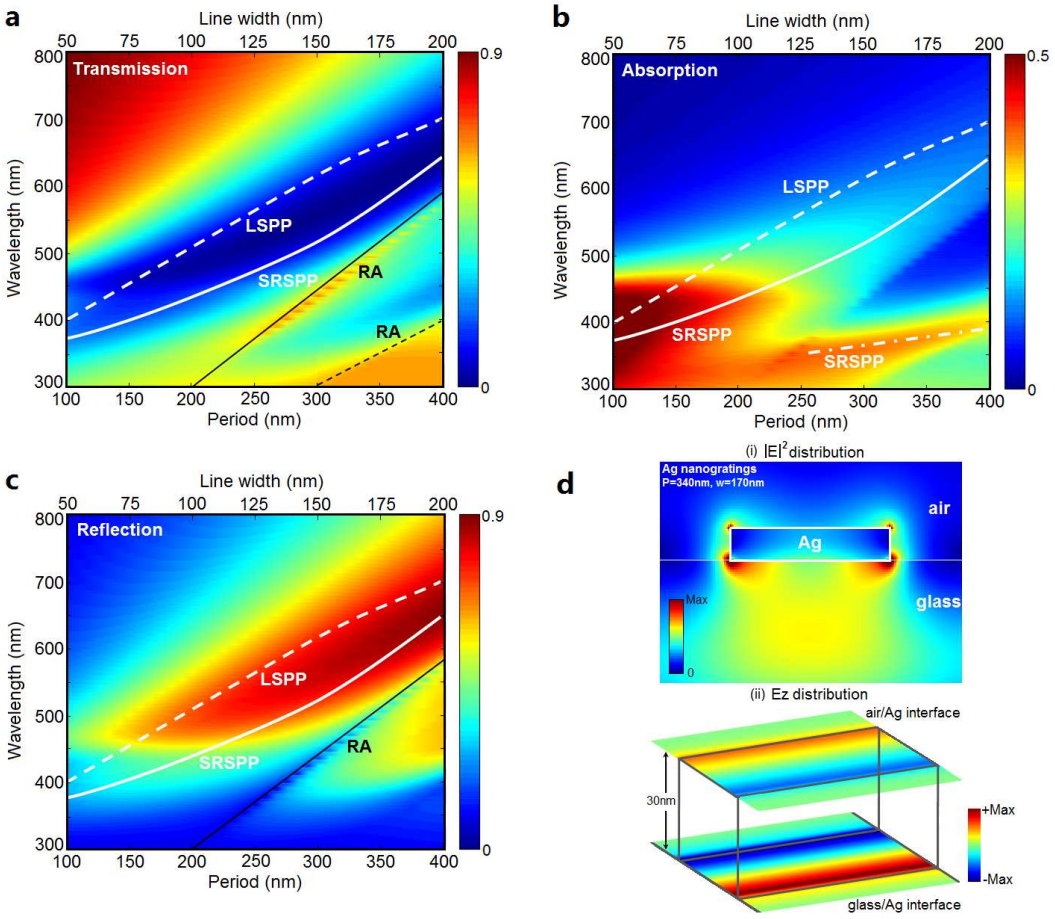

Fig. 3.5 Theoretical clarification of extraordinary low transmission in ultrathin Ag nanogratings. 2D maps of the calculated TM optical transmission (a), absorption (b) and reflection (c) spectra of 30nm-thick Ag nanogratings as a function of the incident wavelength and grating period, when the duty cycle of the nanogratings is set at 0.5. The solid and dashed black lines refer to RA at glass/Ag and air/Ag interfaces, respectively. The solid and dash-dotted white curves correspond to the analytical dispersion relations for the lowest and higher orders SRSPP modes, respectively. The dashed white line represents the calculated spectral positions of LSPP for single Ag lines with the same line-width as that of nanogratings. (d) Electric

field (i) and instantaneous E_z vector (ii) distribution at the air/Ag and glass/Ag interfaces of nanogratings (P=340nm) at the resonance wavelength of 610nm.

The resonance wavelengths of the lowest and higher orders SRSPP modes were calculated using analytical dispersion relations [3.18], and plotted in Fig. 3.5(a)-(c) as solid and dash-dotted white curves, respectively. The contribution of LSPP modes was estimated by calculating the spectral positions of LSPPs for single Ag lines (with the same line-width as that of nanogratings). These are represented by the dashed white line in Fig. 3.5(a)-(c). Both SRSPP and LSPP modes exhibit spectral dependence on the period (line-width) that is in reasonable agreement with the FDTD simulations. The simulated transmission minima and absorption/reflection peaks, which vary continuously from 400nm to 650nm in wavelength as the period increases from 100nm to 400nm, are located in between the dashed (LSPP) and solid white curves (SRSPP). This indicates that LSPP and SRSPP modes both contribute to the ELT effect for the range of geometric parameters considered here. A narrow transmission peak attributed to Rayleigh-Wood anomalies (RA) at the Ag/glass interface (solid black line) ranges at shorter wavelengths [3.31, 3.32]. The dashed black line in Fig. 3.5(a) represents the RA at the air/Ag interface, which matches well with a transmission peak in the ultraviolet region (300~400nm). Fig. 3.5(a)-(c) show that for the range of geometric parameters considered in Fig. 3.4, the transmission minima are primarily attributed to enhanced absorption and reflection in the Ag nanograting, due to the excitation of SRSPP and LSPP modes.

To further characterize the electromagnetic modes at the resonance wavelength, we calculate the electric field (i) and E_z vector (ii) distributions at the air/Ag and glass/Ag

interfaces for ultrathin nanogratings (P=340nm) at a wavelength of 610nm. The results are plotted in Fig. 3.5(d), showing the excitation of propagating SPP modes [3.13]. The enhanced electromagnetic field (i) is strongly confined at the Ag/glass interface, with a decay length of hundreds of nanometers into the glass substrate. In addition, the antisymmetric E_z patterns (ii) correspond to a symmetric surface charge distribution, further demonstrating the propagating SPP modes with the characteristics of SRSPPs [3.21]. Additional simulations reveal that the electromagnetic modes in a relatively broad spectral region close to the transmission minimum have similar E_z patterns. The electric field distribution (i) also shows LSPP modes (with a decay length of tens of nanometers) at the corners of nanogratings. Accordingly, the resonant electromagnetic modes in the ultrathin Ag nanogratings (duty cycle 0.5) have the properties of hybrid LSPP and SRSPP modes.

The FDTD simulations performed above, systematically varying geometric parameters such as periodicity and line-width (duty cycle 0.5), help to clarify the underlying physical mechanisms for ELT in ultrathin Ag nanogratings, and illustrate the relative contributions of the different electromagnetic modes (SRSPPs, LSPPs, and RA). For the range of geometric parameters used in our experiments (periods ranging from 220 to 360 nm), ELT results from the excitation of both SRSPP and LSPP modes that lead to enhanced absorption and reflection.

3.4 High-resolution plasmonic subtractive color filtering and applications

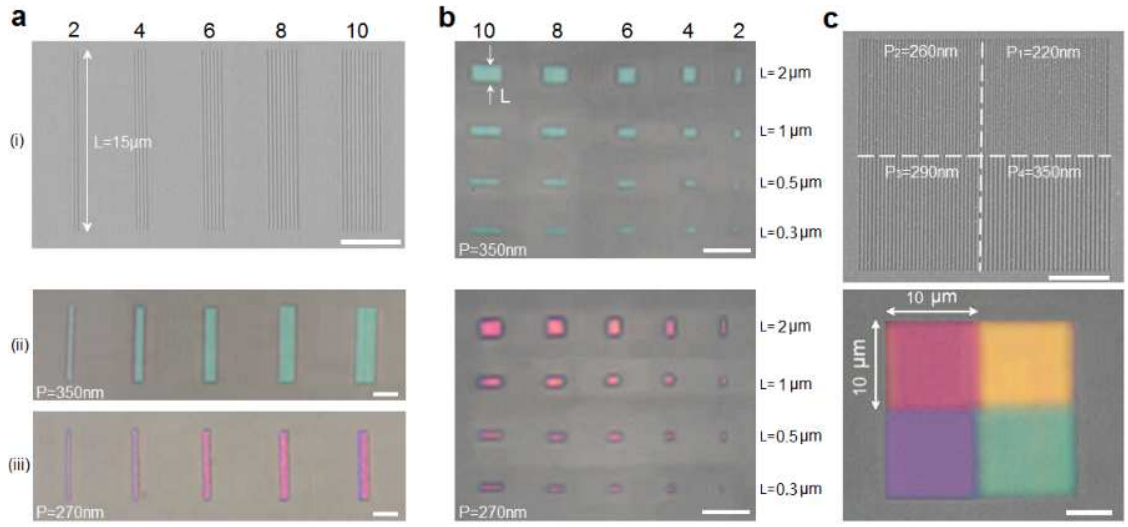

Fig. 3.6 Ultra-compact and high-resolution plasmonic subtractive color filters. (a) SEM image (i) of plasmonic SCFs with 2, 4, 6, 8 and 10 nanoslits of period P=350nm. (ii) and (iii) show the optical microscope images under TM illumination for the case of 2, 4, 6, 8 and 10 nanoslits with periods of 350nm and 270nm, respectively. (b) Optical microscope images of cyan (top panel, P=350nm) and magenta (bottom panel, P=270nm) plasmonic SCFs with 2, 4, 6, 8 and 10 nanoslits of differing lengths, ranging from 2μm to 0.3μm. (c) Top panel shows a SEM image of a plasmonic SCF mosaic consisting of four different $10\times10\mu m^2$ color filter squares (nanogratings with different periods of P_1=220nm, P_2=260nm, P_3=290nm, and P_4=350nm) with no separation. Bottom panel is the optical microscopy image. All of the scale bars are 5μm.

We now examine the functional relationship between plasmonic subtractive color filtering and feature size, to explore the achievable SCF spatial resolution and determine the smallest pixel size for imaging applications. Fig. 3.6(a) shows cyan and magenta plasmonic SCF arrays consisting of 2, 4, 6, 8 and 10 nanoslits, all with the same length of 15μm and a duty cycle of 0.5. The nanoslit periods for the cyan and magenta SCFs are 350nm and 270nm, respectively. Surprisingly, the SCF arrays with only two nanoslits still exhibit distinct cyan (ii) or magenta (iii) colors. The nanoscale dimensions for the cyan and magenta filters with two nanoslits (525nm and 405nm, respectively) are close to the diffraction limit of visible light (λ/2, 200~350nm) [3.4, 3.24]. The electric field distributions were calculated for the cyan and magenta double-slit structures (see Fig.

3.7). These simulations indicate that both SRSPP and LSPP modes are excited in these nanoscale doublet structures and contribute to the observed colors. Additionally, Fig. 3.6(b) shows a series of cyan and magenta SCF structures fabricated with 2, 4, 6, 8 and 10 nanoslits, with slit lengths of 2, 1, 0.5, and 0.3μm. The microscope images show that color filtering persists in the plasmonic SCFs with a few nanoslits even when the length of nanoslits is decreased to 0.3μm. Therefore, plasmonic SCFs are capable of generating much smaller pixel sizes (~0.5×0.3μm^2) than the smallest pixels achieved today in commercial image sensors (1.12×1.12μm^2, Sony Corp.). A unique feature of the plasmonic SCFs is their ability to perform color filtering on the nanometer scale, with much simpler and thinner structures than that of previous multilayered designs [3.3].

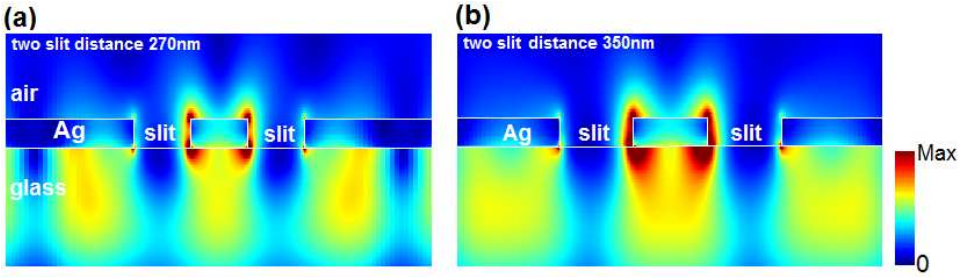

Fig. 3.7 Electric field distribution of plasmonic SCFs consisting of only two nanoslits that exhibit distinct magenta or cyan colors, with slit-to-slit distances of (a) 270nm and (b) 350nm, respectively. The duty cycle, 0.5. Strongly confined and enhanced electromagnetic fields, associated with SRSPP and LSPP modes, are observed at the central Ag wires.

Additionally, Fig. 3.6(c) shows a 2×2 array of plasmonic SCFs fabricated to examine the effect of spatial crosstalk between adjacent structures on transmitted colors. This color filter mosaic consists of four different square-shaped (10×10μm^2) plasmonic SCFs fabricated by FIB with zero separation. The four SCFs are composed of nanogratings with different periods (P_1=220nm, P_2=260nm, P_3=290nm, and P_4=350nm),

as shown by the SEM images in the top panel of Fig. 3.6(c). The optical microscope image of the color filter mosaic under TM-polarized white light is shown in the bottom panel of Fig. 3.6(c). Four distinct subtractive colors can be clearly resolved even at the center corner or boundaries of adjacent filters, indicating that the proposed plasmonic SCFs can be applied to high-resolution color filter arrays widely used in imaging sensors or color displays [3.22, 3.23, 3.33]. The image blurring at boundaries arises from effects of light diffraction and the limited optical resolution of the microscope.

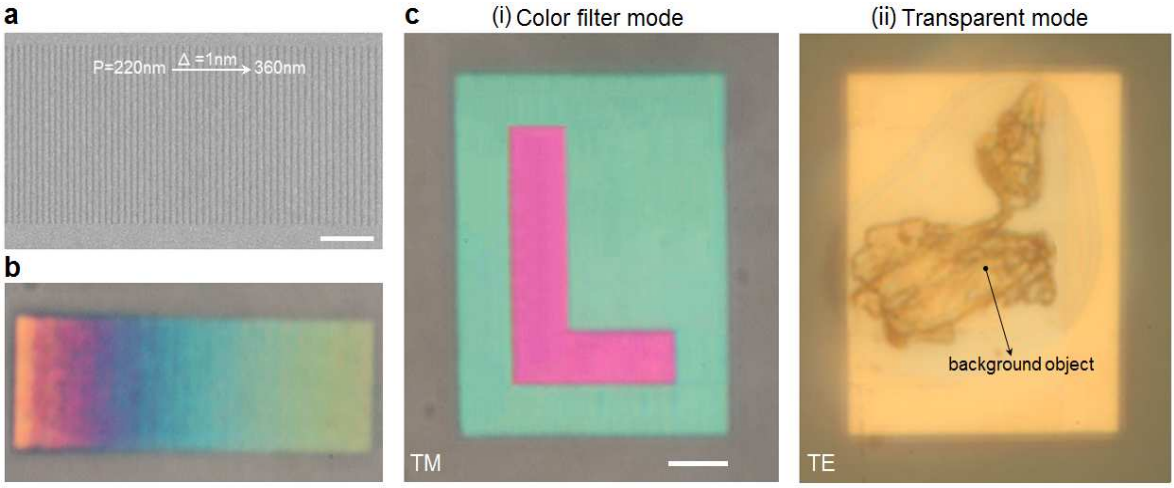

Fig. 3.8 Ultrathin plasmonic subtractive color filters for spectral imaging and transparent displaying. (a) A SEM image of the fabricated plasmonic subtractive spectroscope with grating periods gradually changing from 220nm to 360nm (from left to right, with 1nm increment). The line-width of each nanoslit is fixed at 110nm, and the scale bar represents 5μm. (b) Optical microscopy image of the plasmonic spectroscope illuminated with TM-polarized white light. (c) Optical microscopy image of (i) a magenta pattern 'L' in a cyan background formed by nanogratings with two different periods (P_1=270nm, P_2=350nm) fabricated on a 30nm-thick Ag film, and illuminated with TM-polarized white light. The scale bar is 10μm. (ii) Imaging the background object through the same structure, under TE illumination.

Spectral imaging combines two normally distinct techniques: imaging, in which the light intensity is typically measured at each pixel in a two dimensional array, and spectroscopic measurements of intensity as a function of wavelength, thus generating a three-dimensional multispectral data set I(x,y,λ). Applications of spectral imaging range

from biological studies to remote sensing. However, this technique typically employs bulky filters and scanning interferometers to acquire a complete spectrum at each pixel [3.34], since conventional miniature color filter arrays are normally limited to three spectral bands (i.e. RGB or CMY) [3.3, 3.6]. Recent studies of plasmonic miniature color filter arrays with wide color tunability were conducted to enable direct recording of spectral image data in a single exposure without scanning. These included plasmonic photon sorters (which had a limited transmission efficiency of 1.5~15% [3.6]) and an ultra-compact plasmonic spectroscope (composed of complex MIM nano-resonators [3.3]). In the current work, we employ plasmonic SCFs array to achieve a compact plasmonic subtractive spectroscope. Fig. 3.8(a) shows a SEM image of the fabricated device consisting of ultrathin nanogratings with periods gradually changing from 220nm to 360nm in increments of 1nm and a fixed nanoslit width of 110nm. When illuminated with TM-polarized white light, the structure produces a rainbow stripe of continuous subtractive colors, as shown in Fig. 3.8(b). This miniature plasmonic subtractive spectroscope can disperse the entire visible spectrum into component colors within a distance of a few micrometers, which is orders of magnitude smaller than the conventional prism- or grating-based devices for multispectral imaging [3.34]. This plasmonic subtractive spectroscope has a much higher transmission efficiency (60~70%), a simple scheme consisting of a single ultrathin nanopatterned metal film, which is five to ten times thinner than that of previous designs [3.3, 3.6].

Next, we demonstrate the potential of plasmonic SCFs for transparent displays [3.25,

3.26]. Fig. 3.8(c,i) shows an optical microscope image of a magenta character ‘L’ in a cyan background, formed when nanopatterns are illuminated with TM-polarized white light. The letter ‘L’ is constructed by nanogratings with a period of P=270nm, and the cyan background by nanogratings with a period of P=350nm. Two distinct colors are clearly preserved even at the sharp corners and boundaries between the two different patterns, indicating the high-resolution color filtering capability. Under TE-polarized illumination, on the other hand, the same structure remains a transparent window, through which we can clearly observe a background object with its detailed features, as shown in Fig. 3.8(c,ii). This is quite different from that of the plasmonic nanoresonator ACFs, for which the TE-polarized incident light is totally blocked [3.3]. Therefore, the ultrathin plasmonic SCFs can function as color filters as an alternative to conventional colorant color filters and plasmonic ACFs, or act as a highly transparent window under illumination with a different polarization, offering a new approach for high-definition transparent displays through actively controlling the polarization of incident light at each color pixel.

3.5 Discussion

The theoretical simulations predict that ELT-based subtractive color filters in ultrathin Ag nanogratings can achieve strong extinction within the resonance band, as well as high transmission peaks away from the resonance wavelength (i.e., 60~70% for a duty cycle of 0.5). This peak transmission is significantly larger than that (7~27%) of a closed Ag film of the same thickness. Moreover, since these structures are not optimized,

further improvement may be possible, potentially achieving transmission values comparable to or even larger than that of commerical color filters. For example, we consider how the optical properties of plasmonic SCFs are affected by varying the grating duty cycle. The transmission away from the ELT resonance increases with the removal of highly-reflective Ag. Consequently, increasing the separation between neighboring Ag lines (i.e. varying the grating period while keeping the linewidth fixed) would further enhance the transmission efficiency. However, the near-field coupling between adjacent Ag lines may also become less efficient as the separation is increased, potentially reducing the effectiveness of SRSPP modes relative to LSPP modes and affecting the ELT minimum. Therefore, the nanograting parameters (such as line-width, separation between adjacent lines, and period) should be varied judiciously to achieve simultaneous optimization of the SCF transmission efficiency and the on-resonance extinction.

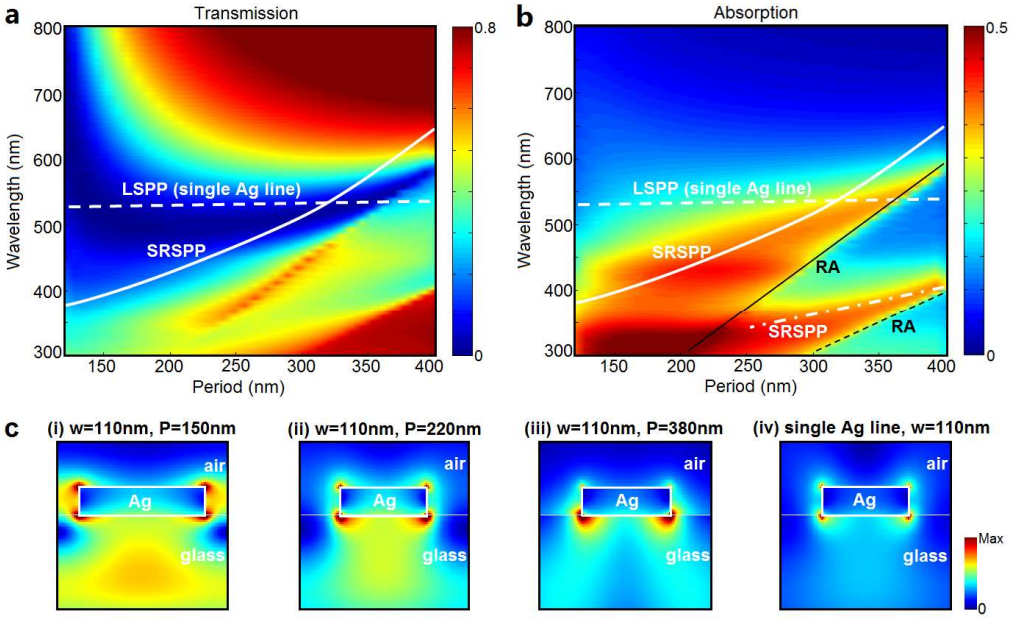

Fig. 3.9 Clarification of different electromagnetic modes in ultrathin Ag nanogratings. 2D maps of the calculated TM optical transmission (a) and absorption (b) spectra of 30nm-thick Ag nanogratings as a

function of the incident wavelength and grating period, when the line-width of individual Ag lines is fixed at 110nm. The solid and dash-dotted white curves correspond to the analytical dispersion relations for the lowest and higher order SRSPP modes, respectively. And the dashed white line represents the spectral position of LSPP for a single Ag line with line-width of 110nm. The solid and dashed black lines in (b) refer to RA at glass/Ag and air/Ag interfaces, respectively. (c) Electric field distribution at the cross-section of ultrathin Ag nanogratings with the fixed line-width w=110nm and period of (i) 150nm, (ii) 220nm, (iii) 380nm; and (iv) a single Ag line with the line-width of 110nm.

Since the excitation of propagating SRSPP modes relies on the effective coupling of electromagnetic modes between Ag lines, we performed FDTD simulations to study the optical properties of ultrathin Ag nanogratings with a constant line-width as a function of the separation between adjacent Ag lines. Fig. 3.9 (a) and (b) show 2D contour maps of the simulated transmission and absorption spectra for 30nm-thick Ag nanogratings as a function of the incident wavelength and grating period, keeping the line-width of Ag wires fixed at 110nm. For periods less than 150nm, the broad transmission minimum in Fig. 3.9(a) in the $400nm<\lambda<800nm$ spectral region is primarily due to high optical reflection, since the separation between adjacent Ag lines (0~40nm) is very small. For nanogratings with $P>150nm$, excitation of SRSPPs and LSPPs in ultrathin Ag nanogratings causes enhanced absorption and reflection that affect the transmission minimum. The spectral transmission minimum narrows and appears less dependent on P with increasing period, suggesting less effective excitation of SRSPPs as the separation between adjacent Ag lines increases.

Fig. 3.9(b) illustrates the contributions of three different mechanisms to absorption enhancement. For periods in the range $150nm<P<250nm$, the separation between adjacent Ag lines ranges from 40 to 140nm, and the absorption is mainly attributed to the

excitation of SRSPP modes, as indicated by the analytical SRSPP dispersion curves (solid white curve). As the period increases further, the absorption spectra are closer to those predicted for LSPP modes (dashed white curve). For periods greater than 300nm, the electromagnetic modes excited in individual Ag lines do not couple effectively with each other due to the large separation (>190nm) between adjacent lines. Finally, for P>350nm, RA modes (solid black curve) interact with SPPs, leading to a red-shift in absorption spectra.

The physical mechanisms are further illustrated by the calculated electric field distribution at the resonance wavelengths in these 30nm-thick Ag nanogratings with a fixed 110nm line-width. Grating periods of (i) 150nm, (ii) 220nm, and (iii) 380nm, as well as (iv) a single Ag line were considered, and the results shown in Fig. 3.9(c). For the 150nm period (i), with a 40nm separation between grating lines, the electromagnetic modes excited in neighboring Ag lines strongly interact with each other. Both LSPP and SRSPP modes at the Ag/glass interface are clearly observed. For P=220nm (ii), the electromagnetic coupling between adjacent Ag lines is weaker than that in (i), but the excitation of SRSPP modes is still observable. For the 380nm period (iii), the SRSPP modes are much less evident due to the large separation (270nm) between adjacent Ag lines, and the field distribution approaches that of a single Ag line in (iv), which shows primarily LSPP modes. Slight differences in the resonance wavelengths between (iii) and (iv) arise due to the RA at the glass/Ag interface.

Plasmonic SCF arrays with only two nanoslits surprisingly exhibited distinct

subtractive colors, which can be understood in terms of the strong confinement properties of SRSPP and LSPP modes [3.15-3.21]. Much of the electric field is concentrated in the metal film, resulting in strong Ohmic losses and short decay lengths. Because of the short propagation distance of SRSPPs and small decay length of LSPPs, interactions between neighboring nanostructures are weaker than those for EOT phenomenon, where SPPs excited at each nanoslit (or nanohole) strongly interact with numerous nearby nanoslits (or nanoholes) [3.12-3.14]. Fewer repeat units are required in the proposed plasmonics SCFs than are commonly employed in plasmonic ACFs based on EOT theory.

Although we have only demonstrated polarization-dependent plasmonic subtractive color filtering with 1D ultrathin nanogratings in this work, it can be easily generalized to 2D ultrathin nanostructures (i.e. nanoholes or nanosquares) for achieving polarization-independent operation. Nevertheless, the 1D plasmonic SCFs, which can either function as color filters or highly transparent windows under different polarizations, making them highly attractive for transparent displaying [3.25, 3.26]. In traditional transparent displays, the RGB color pixels of the color filter are reduced to the minimum size for transparency. Display panel makers even remove the color filter, making the transparent display monochrome. Therefore, the low resolution and color gamut is a fundamental limitation in current transparent displaying techniques. The 1D plasmonic SCFs, which are capable of generating extremely small pixel sizes (~$0.5\times0.3\mu m^2$) for high spatial resolution, could significantly advance this application area.

Discrepancies between the experimental and numerical results can be attributed to

the nonparallel incident light employed in the optical measurement, nanofabrication defects, finite periodicity in the fabricated structures, and surface roughness, which are not considered completely in numerical simulations. Although the experimental transmission minimum (6%) differs appreciably with the numerical value of 0.39% in Fig. 3.2, significant improvements should still be possible. The surface roughness (large grain size) in ultrathin Ag films is one of the factors that could significantly degrade the performance of plasmonic SCFs, possibly leading to measurement errors and non-uniform colors. Improved plasmonic SCF structures can be realized, for example, by introducing an intermediate (1nm) Ge wetting layer before depositing Ag on the glass substrate or using template-stripping techniques [3.35-3.38], permitting ultra-smooth Ag films with smaller grain sizes for improved color filtering performance.

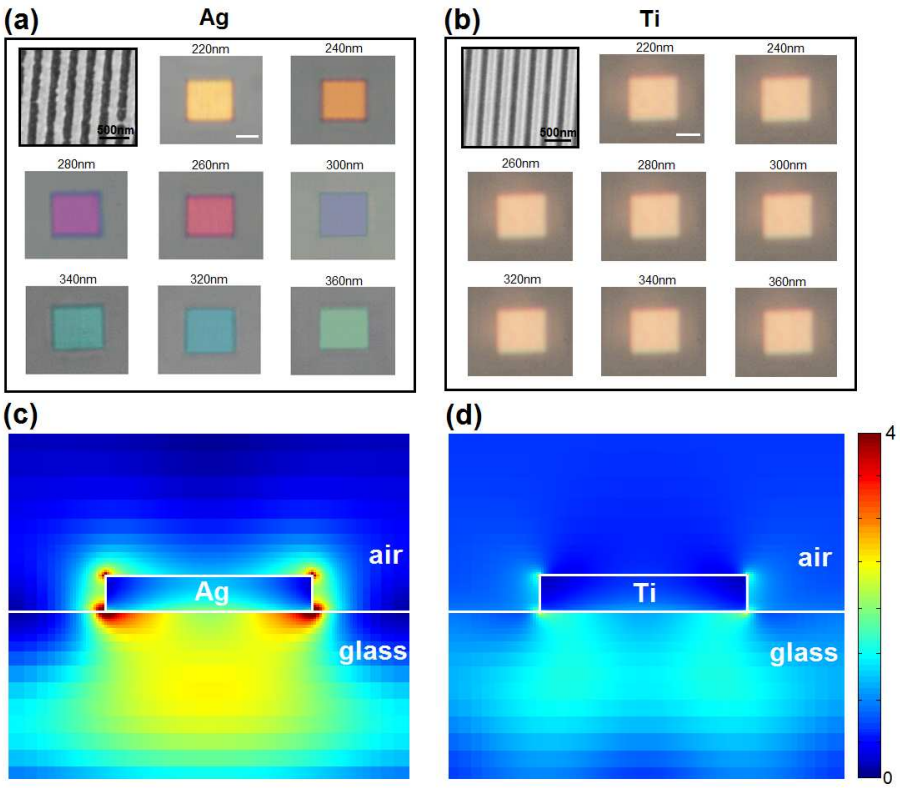

Fig. 3.10 Plasmonic v.s. non-plasmonic ultrathin nanogratings. (a) A full palette of transmitted subtractive colors (ranging from yellow to cyan) is revealed in above $10\times10\mu m^2$ squares under TM-polarized white light illumination. The scale bar represents 5μm. The period of the Ag nanogratings varied from 220nm to 360nm, in 20nm increments. The inset shows a SEM image, with a scale bar indicating 500nm. (b) Optical microscopy images of Ti nanogratings under the same conditions as that of Ag nanogratings. Electric field distribution of (c) Ag and (d) Ti nanogratings with period P=320nm and line-width w=160nm at the resonance wavelength of 575nm.

Plasmonic v.s. non-plasmonic ultrathin nanogratings. To distinguish between plasmonic and non-plasmonic effects in the nanogratings, a control experiment was also performed on a series of nanogratings in an ultrathin (30nm-thick) Ti film. Ti is a lossy material that does not support SPPs in this wavelength range. Fig. 3.10 (a) and (b) show the optical microscope images of the ultrathin Ag and Ti nanogratings (inset shows representative SEM images of the fabricated nanogratings) under the same experimental conditions. All of the fabricated nanogratings have the same dimensions of $10\times10\mu m^2$. In Fig. 3.10(a), the Ag nanogratings exhibit a full palette of filtered subtractive colors that change from yellow to cyan, for periods varying between 220nm and 360nm in 20nm increments (duty cycle is set as 0.5). On the contrary, no color filtering effects can be observed in the non-plasmonic Ti nanogratings under the same experimental condition, as shown in Fig. 3.10(b). This control experiment unambiguously demonstrates the plasmonic origin of subtractive color filtering in ultrathin Ag nanogratings.

To further characterize the plasmonic effect, we calculate the electric field distribution of ultrathin (30nm-thick) Ag and Ti nanogratings (period P=320nm, line-width w=160nm) at the resonance wavelength (transmission minimum) of 575nm, and plot them in Fig. 3.10(c) and (d), respectively. In Fig. 3.10(c), the highly-confined

and enhanced electric field at the Ag/glass interface and sharp corners of the Ag strip clearly demonstrates the excitation of plasmonic modes. On the contrary, no such strong field confinement is observed in the Ti nanogratings, as shown in Fig. 3.10 (d). Therefore, the above experimental and simulation results clearly demonstrate that plasmonic interactions are responsible for subtractive color filtering in ultrathin Ag nanogratings.

3.6 Summary

In summary, systematic theoretical and experimental studies were performed to clarify the underlying physical mechanisms that determine the ELT phenomenon. Different electromagnetic modes (SRSPPs, LSPPs, and RA) can be excited in ultrathin Ag nanogratings, depending on their geometric parameters. By exploiting ELT theory, we have proposed and demonstrated plasmonic SCFs associated with fundamentally different color filtering mechanisms than previous state-of-art plasmonic ACFs. The simple design, with its wide color tunability, ease of fabrication and device integration, as well as robustness and reliability, combines advances of SCFs and ultrathin plasmonic nanostructures to overcome key challenges in current colorant and plasmonic color filters. An unusually high transmission efficiency of 60~70% has been achieved, with the potential for further enhancement. In addition, the proposed plasmonic SCFs are capable of generating even smaller pixel sizes than the smallest pixels achieved today in commercial image sensors. Finally, their unique polarization-dependent features allow the same structures to function either as color filters or highly-transparent windows under different polarizations, opening an avenue towards high-definition transparent displays.

While only 1D nanograting structures have been demonstrated here, this design principle can be extended to 2D structures to achieve polarization-independent operation. The design can also be easily applied to other spectrum regimes for different applications.

References

[3.1] S. Nishiwaki, T. Nakamura, M. Hiramoto, T. Fujii & M. Suzuki, Efficient colour splitters for high-pixel-density image sensors. Nat. Photonics 7, 240 (2013).

[3.2] S. Yokogawa, S. P. Burgos & H. A. Atwater, Plasmonic color filters for CMOS image sensor applications. Nano Lett. 12, 4349 (2012).

[3.3] T. Xu, Y.-K. Wu, X. Luo, & L. J. Guo, Plasmonic nanoresonators for high resolution colour filtering and spectral imaging. Nat. Commun. 1, 1 (2010).

[3.4] Y-K. Wu, A. E. Hollowell, C. Zhang, & L. J. Guo, Angle-Insensitive Structural Colours based on Metallic Nanocavities and Coloured Pixels beyond the Diffraction Limit. Sci. Rep. 3, 1194 (2013).

[3.5] K. Diest, J. A. Dionne, M. Spain, & H. A. Atwater, Tunable color filters based on metal–insulator–metal resonators. Nano Lett. 9, 2579 (2009).

[3.6] E. Laux, C. Genet, T. Skauli, & T. W. Ebbesen, Plasmonic photon sorters for spectral and polarimetric imaging. Nat. Photonics 2, 161 (2008).

[3.7] H. S. Lee, Y. T. Yoon, S. S. Lee, S. H. Kim & K. D. Lee, Color filter based on a subwavelength patterned metal grating. Opt. Express 15, 15457 (2007).

[3.8] Q. Chen & D. R. Cumming, High transmission and low color cross-talk plasmonic color filters using triangular-lattice hole arrays in aluminum films. Opt. Express 18, 14056 (2010).

[3.9] D. Inoue, et al., Polarization independent visible color filter comprising an aluminum film with

surface-plasmon enhanced transmission through a subwavelength array of holes. Appl. Phys. Lett. 98, 093113 (2011).

[3.10] A. F. Kaplan, T. Xu & L. J. Guo, High efficiency resonance-based spectrum filters with tunable transmission bandwidth fabricated using nanoimprint lithography. Appl. Phys. Lett. 99, 143111 (2011).

[3.11] Y. T. Yoon, C. H. Park & S. S. Lee, Highly efficient color filter incorporating a thin metal-dielectric resonant structure. Appl. Phys. Express 5, 022501 (2012).

[3.12] T. W. Ebbesen, H. J. Lezec, H. F. Ghaemi, T. Thio & P. A. Wolff, Extraordinary optical transmission through subwavelength hole arrays. Nature 391, 667 (1998).

[3.13] W. L. Barnes, A. Dereux & T. W. Ebbesen, Surface plasmon subwavelength optics. Nature 424, 824 (2003).

[3.14] C. Genet, & T. W. Ebbesen, Light in tiny holes. Nature 445, 39 (2007).

[3.15] I. S. Spevak, A. Y. Nikitin, E. V. Bezuglyi, A. Levchenko & A. V. Kats, Resonantly suppressed transmission and anomalously enhanced light absorption in periodically modulated ultrathin metal films. Phys. Rev. B 79, 161406 (2009).

[3.16] S. G. Rodrigo, L. Martin-Moreno, A. Y. Nikitin, A. V. Kats, I. S. Spevak & F. J. Garcia-Vidal, Extraordinary optical transmission through hole arrays in optically thin metal films. Optics Lett. 34, 4 (2009).

[3.17] G. D'Aguanno, N. Mattiucci, A. Alu, & M. J. Bloemer, Quenched optical transmission in ultrathin subwavelength plasmonic gratings. Phys. Rev. B 83, 035426 (2011).

[3.18] J., Braun, B., Gompf, G. Kobiela & M. Dressel, How holes can obscure the view: suppressed

transmission through an ultrathin metal film by a subwavelength hole array. Phys. Rev. Lett. 103, 203901 (2009).

[3.19] S. Xiao, et al. Nearly zero transmission through periodically modulated ultrathin metal films. Appl. Phys. Lett. 97, 071116 (2010).

[3.20] S. Xiao, & N. A. Mortensen, Surface-plasmon-polariton-induced suppressed transmission through ultrathin metal disk arrays. Opt. Lett. 36, 37 (2011).

[3.21] Q. Gan, et al. Short Range Surface Plasmon Polaritons for Extraordinary Low Transmission Through Ultra-Thin Metal Films with Nanopatterns. Plasmonics 7, 47 (2012).

[3.22] H. Nabeyama, S. Nagahara, H. Shimizu, M. Noda & M. Masuda, All solid state color camera with single-chip MOS imager. IEEE Trans. Consumer Electron. CE-27, 40 (1981).

[3.23] H. T. Sencar & N. Memon, Digital Image Forensics: Advances and Challenges (Springer, New York, 2012).

[3.24] K. Kumar, H. Duan, R. S. Hegde, S. C. W. Koh, J. N. Wei, & J. K. W. Yang, Printing colour at the optical diffraction limit. Nat. Nanotech. 7, 557 (2012).

[3.25] H.-S. Seo, Transparent display apparatus. U.S. Patent No. 8227797 (2012).

[3.26] R. Azuma, et al., Recent Advances in Augmented Reality. IEEE Comput. Graph. Appli. 21, 34 (2001).

[3.27] S. Y. Chou, P. R. Krauss & P. J. Renstrom, Imprint lithography with 25-nanometer resolution. Science 272, 85 (1996).

[3.28] X. Luo, & T. Ishihara, Surface plasmon resonant interference nanolithography technique. Appl. Phys. Lett. 84, 4780 (2004).

[3.29] B. Zeng, X. Yang, C. Wang, & X. Luo, Plasmonic interference nanolithography with a double-layer planar silver lens structure. Opt. Express 17, 16783 (2009).

[3.30] J. Wang, et al., High-performance nanowire-grid polarizers. Opt. Lett. 30, 195 (2005).

[3.31] R. W. Wood, On a remarkable case of uneven distribution of light in a diffraction grating spectrum. Philos. Mag. 4, 396 (1902).

[3.32] H. Gao, et al., Rayleigh anomaly-surface plasmon polariton resonances in palladium and gold subwavelength hole arrays. Opt. Express 17, 2334 (2009).

[3.33] H.-C. Cheng, I. Ben-David & S.-T. Wu, Five-Primary-Color LCDs. J. Display Technol. 6, 3 (2010).

[3.34] Y., Garini, I. T. Young & G. McNamara, Spectral imaging: principles and applications. Cytometry A 69A, 735 (2006).

[3.35] V. J. Logeeswaran, et al., Ultrasmooth Silver Thin Films Deposited with a Germanium Nucleation Layer. Nano Lett. 9, 178 (2009).

[3.36] P. Nagpal, N. C. Lindquist, S.-H. Oh, D. J. Norris, Ultrasmooth Patterned Metals for Plasmonics and Metamaterials. Science 325, 594 (2009).

[3.37] T. W. Johnson, et al., Highly reproducible near-field optical imaging with sub-20-nm resolution based on template-stripped gold pyramids. ACS Nano 6, 9168 (2012).

[3.38] J. H. Park, et al., Single-crystalline silver films for plasmonics. Adv. Mater. 24, 3988 (2012).

Chapter 4

Rapid and Highly Sensitive Detection using Fano Resonances in Ultrathin Plasmonic Nanogratings

In this chapter, we developed a novel nanoplasmonic sensor platform employing the extraordinary optical properties of one-dimensional nanogratings patterned on 30nm-thick ultrathin Ag films. Excitation of Fano resonances in the ultrathin Ag nanogratings results in transmission spectra with high amplitude, large contrast, and narrow bandwidth, making them well-suited for rapid and highly-sensitive sensing applications.

4.1 Introduction

Optical biosensors employing the surface plasmon resonance (SPR) in flat thin metal films have unquestionable advantages for real-time and label-free detection of

biomolecular interactions, with detection resolution in the range between 10^{-6} and 10^{-7} refractive index unit (RIU) and a temporal resolution of 1 sec [4.1-4.2]. The optical setup of a typical commercial SPR system is illustrated in Fig. 4.1(a), consisting of a light source, a prism SPP coupler, and a detector. The incident light excites SPPs through total internal reflection at the prism-dielectric interface when the momentum matching condition is fulfilled (Eq. 1.11). Depending on which modulation approach is employed (angle, wavelength, or intensity), the detector records a minimum in the angle or wavelength spectrum, or the change of reflected light intensity at a fixed incident angle or wavelength. When there are biomolecules attached to the sensor surface, the local refractive index increases, producing a change in the propagation constant of the SPPs. This change in SPP propagation constant then alters the associated resonant coupling condition (Eq. 1.11), which can be measured as the change in one of the characteristics of the light coupled to SPPs. Depending on which characteristics is measured, SPR sensors can be classified as angular, wavelength, or intensity modulations.

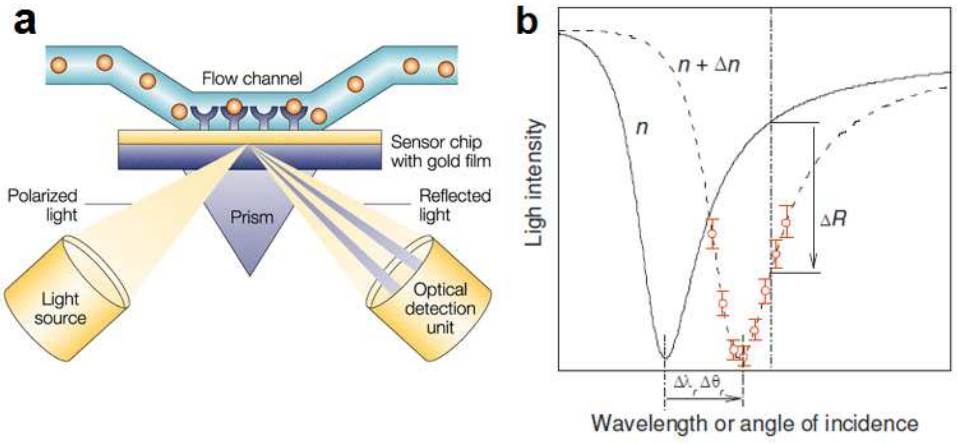

Fig. 4.1 (a) Schematic of an SPR sensor system. (b) Typical SPR wavelength or angular spectrum. The increase in the refractive index results in the red-shift of the angular spectrum Δθ, wavelength spectrum Δλ,

or the decrease of the reflected light intensity ΔR.

In SPR sensors using angular modulation, a narrow-band laser beam excites SPPs through the prism coupler and the resonant light-SPPs coupling leads to a minimum in the angular spectrum of the sensor output, since SPP is a non-radiative mode that is highly confined at the metal/dielectric interface. In SPR sensors based on wavelength modulation, the angle of the incident white light is kept constant, and the wavelength at which light is resonantly coupled to SPPs is measured as the sensor output. In addition, for SPR sensors employing intensity modulation, the wavelength and the angle of the incident light are both kept constant, the change in the intensity of the reflected light serves as the sensor output. Fig. 4.1(b) shows a typical SPR angular or wavelength spectrum, which features a reflection minimum at the resonant SPP coupling wavelength or angle. The increase of the refractive index Δn results in a red-shift of the spectrum (Δλ or Δθ) or a decrease in the reflected light intensity (ΔR) at the fixed wavelength or angle indicated by the dashed-dotted line.

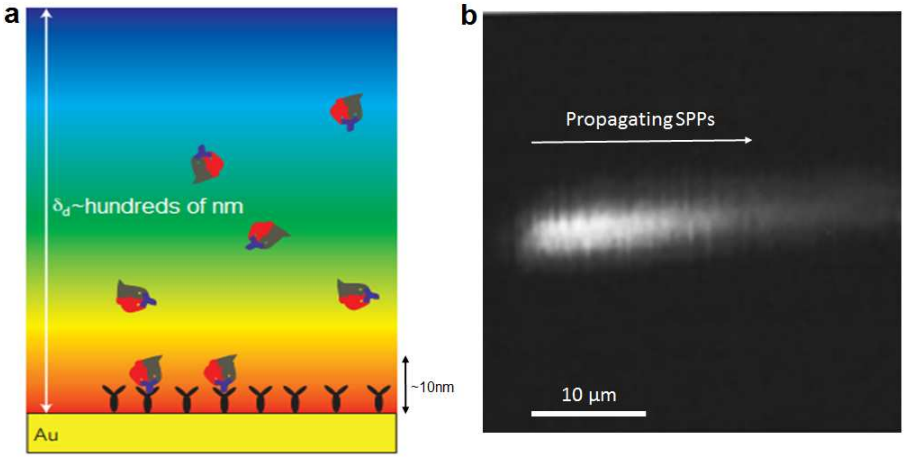

Fig. 4.2 (a) Length scales of the decay length of propagating SPPs and bio-molecules. (b) Near field microscope image of SPP propagation.

Over the past two decades, SPR sensors have become the accepted standard for the rapid kinetic analysis of binding between two proteins [4.3]. However, fundamental properties of the SPR in flat metal films impose several limitations in SPR biosensors relative to other optical sensing approaches. (1) The decay lengths of propagating SPPs into dielectrics, typically hundreds of nanometers at visible frequencies (Eq. 1.9), are much larger than typical sizes of biomolecules, which occupy only a small fraction of the evanescent field, leading to a less than optimal detection resolution, as shown in Fig. 4.2(a) [4.4]. (2) The large propagation distances of SPPs (10~45μm, see Fig. 4.2(b)) at the smooth metal/dielectric interface lead to crosstalk between adjacent sensing areas, which may limit the achievable spatial resolution (footprint) of SPR biosensors, thus the high-throughput capabilities of multiplexed detections. (3) The complexity and cost of the prism-coupled SPR excitation scheme, as shown in Fig. 4.1(a), limit this powerful tool primarily to research laboratories, and are far from ideal for point-of-care devices that can provide instant detection in any place and at any time for personal healthcare. Therefore, the increasing need for sensitive, high-throughput, cost-effective and portable biosensors have driven intense research efforts over the past decade to develop next-generation optical biosensors for clinical and biomedical applications.

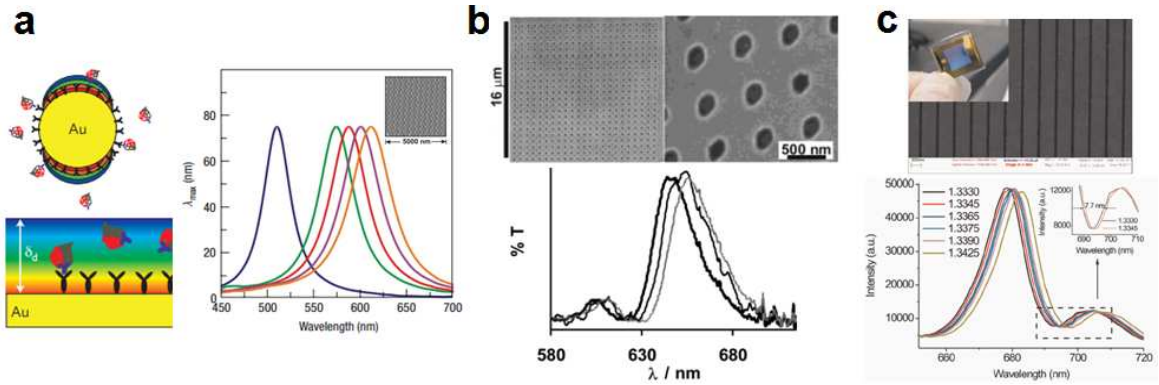

Fig. 4.3 Nanoplasmonic sensors employing (a) metallic nanoparticles; nanohole (b) or nanoslit (c) arrays patterned on optically-thick metal films [4.4-4.11]. Insets show SEM images and measured extinction or transmission spectra in different solutions.

Nanoplasmonic biosensors, employing metallic nanoparticles, nanohole or nanoslit arrays to directly couple incident light into SPPs, have been proposed to overcome above limitations [4.4-4.11]. The localized surface plasmon resonance (LSPR) in metallic nanoparticles exhibits a decay length of tens of nanometers and is highly sensitive to changes close to the surface, as shown in Fig. 4.3(a), making this an attractive approach for biomolecular sensing [4.4-4.6]. However, the strong radiative damping and dissipation losses of LSPRs imply broad resonance linewidths, negatively affecting the device sensing performance [4.4,4.6]. Nanohole or nanoslit arrays patterned on optically-thick metal films in Fig. 4.3(b-c) present additional opportunities due to the co-existence of propagating SPPs (along metal/dielectric interfaces), LSPRs (excited inside individual nanoholes) and plasmonic cavity modes, giving rise to exciting phenomena such as extraordinary optical transmission (EOT) and plasmonic Fano resonances [4.9-4.13]. Due to their narrow linewidths (~4nm), Fano resonances in metallic nanohole arrays were reported to have high figures-of-merits, surpassing those of

commercial SPR sensors [4.9]. However, results reported to date suffer from the relatively weak resonance intensity and low spectral contrast, which limit the signal-to-noise ratio and thus detection resolution [4.9-4.11]. In addition, several groups have recently demonstrated plasmonic interferometric biosensors utilizing interferences between free-space light and propagating SPPs, as shown in Fig. 4.4, and achieved a spectral sensing performance comparable to commercial SPR sensors, as well as a record high intensity-modulation sensitivity [4.14-4.16]. Despite the success of this approach, it is limited by low optical transmission through a single nanoslit or nanohole in each sensor unit, limiting the degree of temporal resolution that can be achieved.

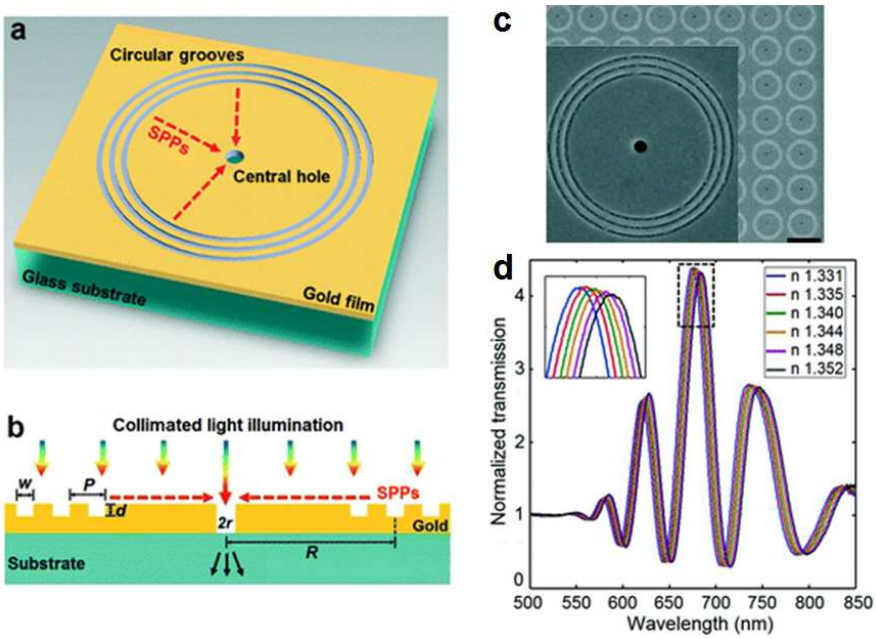

Fig. 4.4 Plasmonic interferometric biosensors employing ring-hole nanostructures. (a) Schematic of the proposed plasmonic interferometer. (b) Side view and the operating principle of the device. (c) SEM images of the fabricated interferometer array and one of the interferometers (inset). (d) The measured transmission spectra of the interferometer array in water and 3, 6, 9, 12, 15% glycerol–water mixtures.

In this work, we present a fundamentally new nanoplasmonic sensor platform exploiting the Fano resonances in one-dimensional (1D) nanogratings patterned on

30nm-thick ultrathin Ag films [4.17-4.19]. Compared with nanohole or nanoslit arrays patterned on optically-thick metal films [4.7-4.13], Fano resonances in ultrathin 1D Ag nanogratings should exhibit significantly higher optical transmission [4.17-4.19], potentially resulting in a strong resonance intensity and high spectral contrast, making them especially suitable for rapid and highly-sensitive sensing applications. Ultrathin nanoplasmonic sensors integrated with PDMS microfluidic channels were fabricated, and their refractive index sensitivity and detection resolution were determined experimentally. The electric field distributions associated with LSPR and SPP modes were determined by FDTD simulations to elucidate the sensor performance and spectral response. The detection, temporal and spatial resolutions determined for the ultrathin plasmonic nanograting sensor are compared to those for previously reported nanoplasmonic biosensors [4.8-4.11,4.14-4.16]. Our results demonstrate significantly improved temporal and spatial resolution (sensor footprint), and a detection resolution comparable to state-of-the-art nanoplasmonic sensors, creating a promising sensing platform for characterizing the real-time kinetics of surface binding events with a high multiplexing capacity [4.4].

4.2 Fabrication and characterization of the ultrathin plasmonic sensor chip

Fabrication of 1D nanogratings on 30nm-thick ultrathin Ag films. E-beam evaporation (Indel system) was used to deposit a 2nm-thick titanium film and

subsequently a 30nm-thick Ag film onto a pre-cleaned standard glass slide (Fisher Scientific). Prior to the evaporation, the glass slides were cleaned thoroughly with acetone in an ultrasonic cleaner for 20min, followed by extensive DI water rinsing. Focused ion beam (FIB) (FEI Dual-Beam system 235) milling (30kV, 30pA) was used to fabricate 1D nanogratings on the deposited 30nm-thick Ag film.

Here FIB milling was used to fabricate the plasmonic nanogratings due to its convenience and precise control over geometric parameters, allowing us to fabricate and optimize the grating design easily. Fig. 4.5 shows different nanostructures we fabricated using FIB, showing the flexibility to easily and precisely control the nanostructure shape and geometric parameters. For our long-term goal to do high-throughput bio-sensing, electron beam lithography will be employed for relatively large-area array patterning. Possibilities for low-cost and large-area sensor platforms will also be explored using other emerging nanofabrication techniques such as nanoimprint lithography, colloidal lithography, or nano-photolithography.

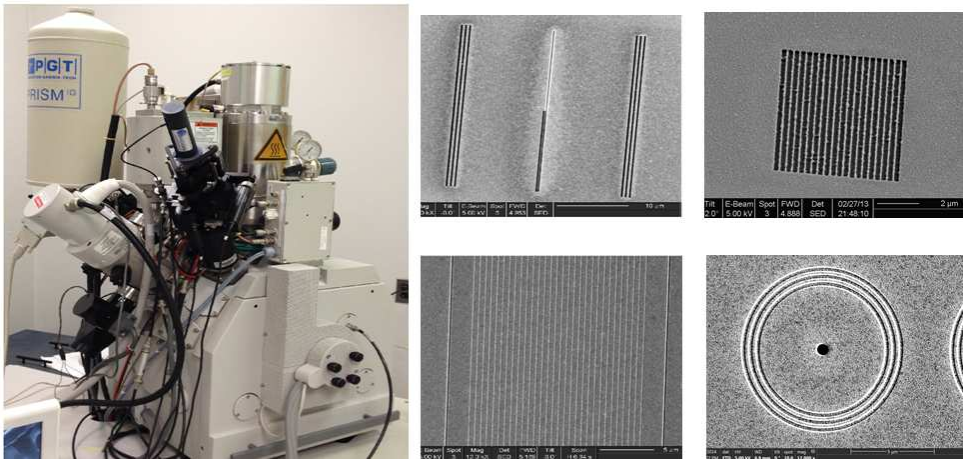

Fig. 4.5 FEI Dual-Beam system 235 used for the nanofabrication. Various nanostructures fabricated using

the FIB milling.

Fabrication of PDMS microfluidic channels. Microfluidic channels were fabricated by conventional photolithography. A SU-8 (SU8-50, Microchem) master mold of the channel (50 µm deep and 4 mm wide) was first pattemed on a 3 inch wafer through the photolithography processes. A 10:1 ratio of PDMS (Sylgard 184, Dow corning) and curing agent were used to cast the mold, which was then baked at 70^{o}C for 3 h. The PDMS channel was cut and peeled from the master, and inlet and outlet holes were punched for tubing.

The sensor chip was cleaned using oxygen plasma (PX-250, March Instruments) and then clamped to the PDMS microfluidic channel. Fig. 4.6(a) shows a photograph of the fabricated ultrathin plasmonic nanograting sensor chip integrated with a microfludic channel. Due to the transparency of ultrathin Ag film in the visible regime [4.19], the background patterns can be clearly seen through the semi-transparent device. In the central area of Ag film (black box), The fabricated 1D nanogratings was with a period of 420nm and slit-width 110nm, as shown in Fig. 4.6(b).

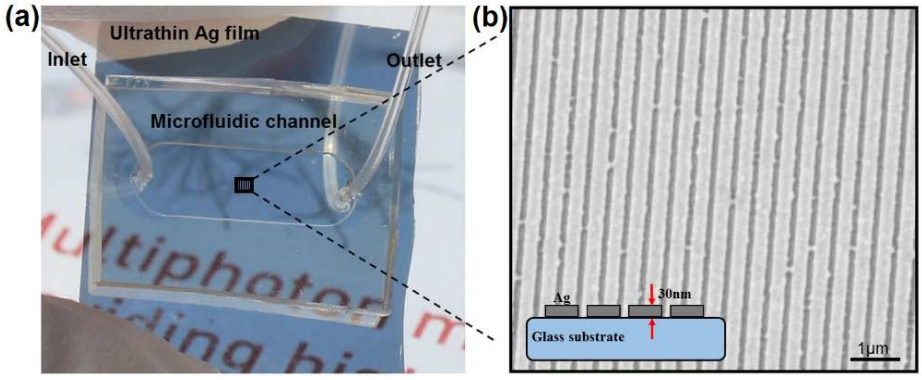

Fig. 4.6 (a) A photograph of an ultra-thin (30nm-thick) Ag film integrated with a PDMS microfluidic channel. The whole device is semitransparent, showing the background patterns. 1D nanogratings are fabricated in the center area of Ag film (black box). (b) A detailed SEM image of 1D nanogratings patterned on the ultrathin

Ag film, with a period of 420nm and slit-width 110nm. Scale bar, 1μm. Inset, a cross-section illustration of the ultrathin Ag nanogratings on a glass substrate.

Experimental setup for optical measurement. Optical measurements were performed in a simple collinear transmission geometry using an Olympus IX81inverted microscope [4.15,4.19], as shown in Fig. 4.7. A white light beam from a 100W halogen lamp illuminated the sample surface through a 50× objective lens, with a spot size of ~50×50μm^2. The field and aperture diaphragms of the microscope were both closed to obtain a nearly collimated light beam. A linear polarizer was used to limit the incident light to transverse magnetic (TM) polarization. The transmitted light was collected through a 40× objective lens (numerical aperture, NA=0.6), and then coupled into a multimode fiber bundle interfaced to a fiber-based compact spectrometer (Ocean Optics USB4000). A CCD camera (Cooke sensicam qe) was employed to record the positions of the nanogratings and the illumination spot.

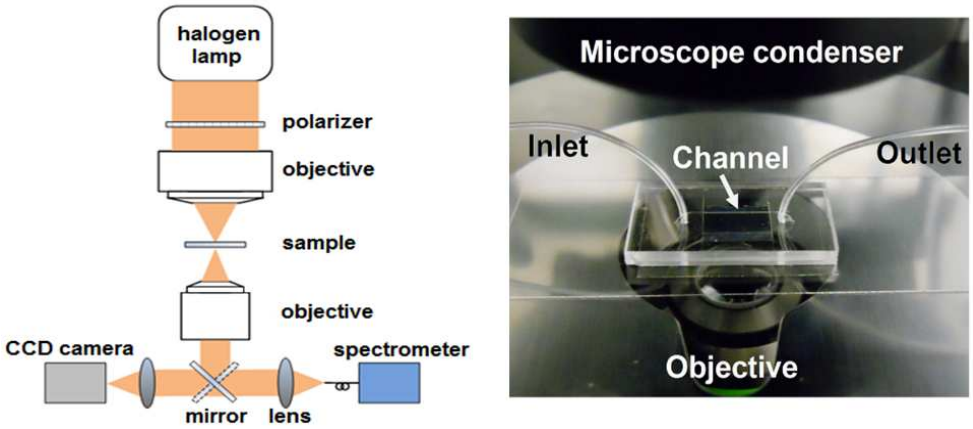

Fig. 4.7 The experimental setup for the optical transmission measurements using an Olympus IX81 inverted microscope.

4.3 Fano resonances in ultrathin plasmonic nanogratings

What is Fano resonance? In 1961, in a quantum mechanical study of the autoionizing states of atoms, Ugo Fano discovered a new type of resonance that now bears his name. In contrast to a classical Lorentzian resonance, the Fano resonance exhibits a distinctly asymmetric shape with the following functional form [4.20]:

$$I \propto \frac{(F\gamma+\omega-\omega_0)^2}{(\omega-\omega_0)^2+\gamma^2} \tag{4.1}$$

Where ω_0 and γ are standard parameters that denote the position and width of the resonance, respectively. F is the Fano parameter, which describes the degree of asymmetry. The microscopic origin of the Fano resonance arises from the constructive and destructive interference of a narrow resonance (a discrete state) with a broad resonance (a continuum state). The first observation of the Fano resonance in optics is probably Wood's anomaly, in which the asymmetric spectral profiles is related to interference of narrow excited leaky modes with an broad incoming radiation. Over the past few years, the Fano resonance has been observed in a number of nanoscale optical systems, e.g. plasmonic nanostructures, metamaterials, and nanohole or nanoparticle arrays, etc. And the steep dispersion of the Fano resonance profile finds applications in optical sensors, lasing, switching, and slow-light devices.

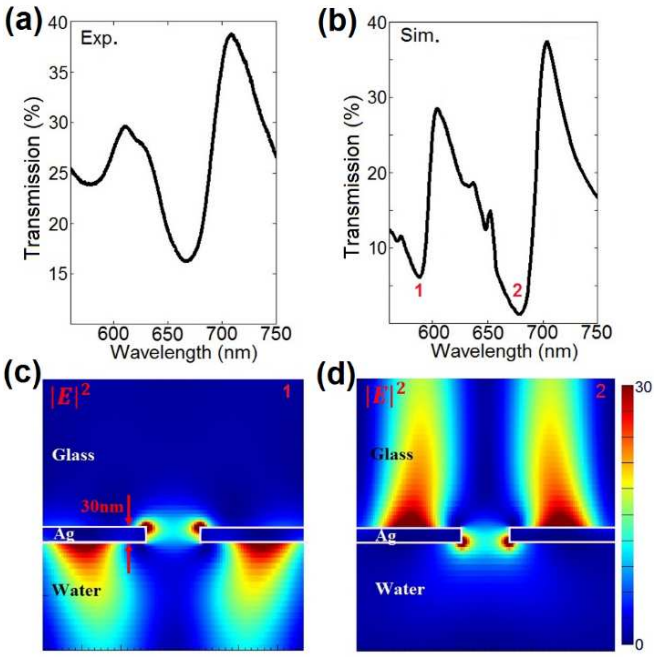

Fig. 4.8 (a) Measured and (b) simulated optical transmission spectra (TM polarization) through 30nm-thick Ag nanogratings with a period of 420nm and slit-width 110nm. Two transmission minima are indicated by the numbers 1 and 2 in (b). (c-d) Electric field distributions at two different resonance wavelengths, corresponding to transmission minima 1 and 2 in (b), respectively.

Fig. 4.8(a) and (b) show the measured and simulated TM polarized optical transmission spectra for light normally incident on a 30nm-thick Ag nanograting in a water environment. The period and slit widths of the nanogratings are 420nm and 110nm, respectively. The spectra were normalized to the reference spectrum of an open aperture with the same area as the nanograting. The transmission spectrum contains two Fano-type asymmetric profiles, each containing a maximum and minimum that are attributed to the constructive and destructive interferences between the broadband LSPR in the nanoslits and two narrowband propagating SPPs on the top (Ag/water) or bottom (Ag/ glass) metal/dielectric interfaces [4.10,4.11,4.20-4.22], respectively. For 1D nanogratings, the momentum matching condition between incident photons and SPPs is fulfilled when the

Bragg coupling condition $k_{spp} = 2\pi/\lambda_0 \cdot \sin\theta + i \cdot 2\pi/P$ is met [4.23]. Here k_{spp} is the wave-vector of SPPs, λ_0 incident wavelength, θ incident angle, i is the grating order, P is the period of nanogratings. The wave-vector relations for SPPs at the metal/dielectric interface is $k_{spp}=2\pi/\lambda_0 \cdot \sqrt{\varepsilon_m \varepsilon_d/(\varepsilon_m+\varepsilon_d)}$ (ε_m and ε_d are the dielectric constants of metal and dielectric material) [4.23]. For normally incident light $\theta=0^0$, the theoretical resonance wavelengths of SPPs are λ_1=596nm and λ_2=665nm at Ag/water and Ag/glass interfaces, respectively, which agree well with the measured and simulated transmission minima [4.24], as shown in Fig. 4.8(a) and (b). The spectra differ significantly from the Fano resonances observed in nanoslit or nanohole arrays patterned on optically-thick metal films, which exhibit an extremely low resonance intensity (~1% peak transmission) and modulation ratio [4.9-4.11]. The transmission peak in the Fano-type spectrum of the ultrathin Ag nanogratings studied here increased up to nearly 40%. The increase in transmitted intensity and modulation ratio at resonance can be attributed to the strong SPPs excited by light transmitted through the nanoslits in the ultrathin metal film. The resonant amplitude of the SPPs is comparable to that of broadband LSPRs, leading to a strong interference between these two modes. This interference is expected to degrade with increasing film thickness, as the reduced transmission through nanoslits (or nanoholes) results in a much lower SPP mode intensity (see Fig. 4.9) and Fano resonances with a low resonance intensity and modulation ratio. The proposed ultrathin nanostructures with strong Fano resonances create an opportunity to achieve sensing with high signal-to-noise ratio and improved detection resolution.

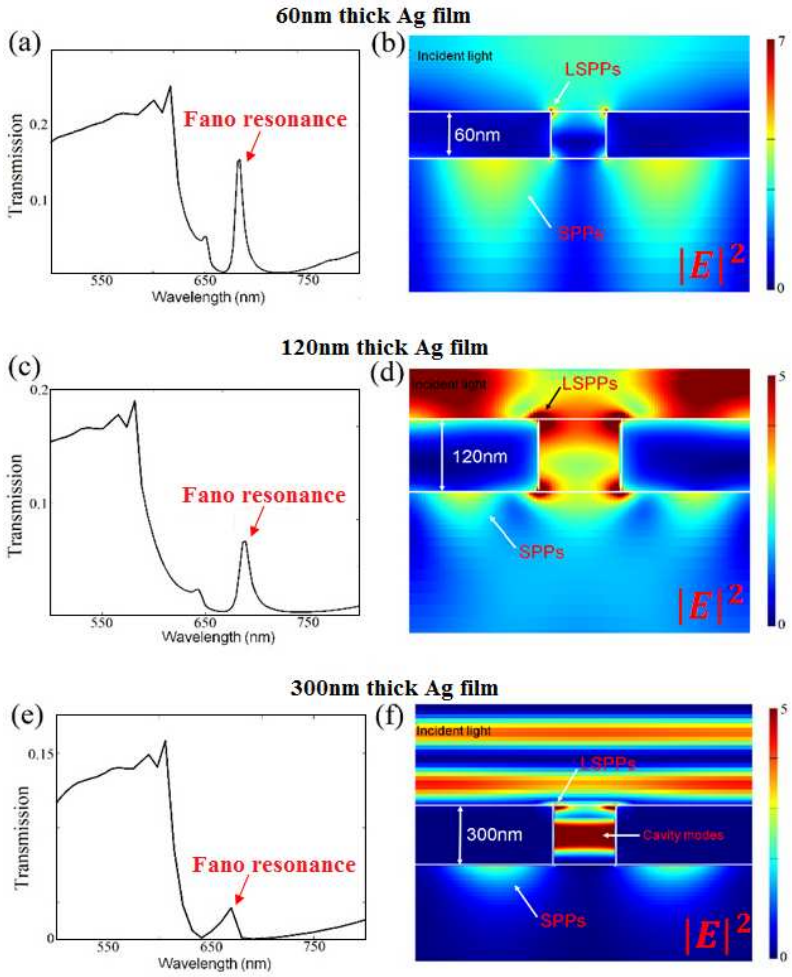

Fig. 4.9 (a, c, e) Simulated optical transmission spectra (TM polarization) through 60*nm*, 120*nm*, 300*nm*-thick Ag nanogratings with a period of 420*nm* and slit-width 110*nm*. (b,d,f) Electric field distributions, corresponding to Fano resonances in (a,c,e), respectively. LSPPs show up on both surfaces as the film becomes thicker from (b) 60*nm* to (d) 120*nm*. And then the cavity mode (f) appears as the film thickness increases up to 300*nm*. As the film thickness increases from 30*nm* to 300*nm*, the intensity of SPPs excited by the light transmitted through the nanoslit becomes weaker, leading to less-effective interference with broadband LSPPs and smaller modulation ratio of Fano resonances.

In order to elucidate the physical mechanisms, Fig. 4.8(c) and (d) plot electric field distributions at two resonance wavelengths corresponding to the transmission minima 1 and 2 in Fig. 4.8(b), respectively. Fig. 4.8(c) clearly shows LSPR modes (with a decay length of tens of nanometers) around the corners of the nanogratings at the glass/Ag interface, and SPP modes (with a decay length of hundreds of nanometers) at the

water/Ag interface. This pattern is reversed in Fig. 4.8(d), where the field distributions of LSPR and SPP modes are located at the water/Ag and glass/Ag interfaces, respectively. The electric field distributions clearly demonstrate the co-existence of both LSPR and SPP modes for different resonance wavelengths. The LSPR and SPP modes interact with each other and generate Fano resonances with asymmetric spectral profiles [4.20-4.22]. The fields of propagating SPPs penetrate hundreds of nanometers into the surrounding dielectric, while the fields of LSPR mode are concentrated within tens of nanometers at the metal surfaces. Thus, LSPRs have the potential to probe surface binding events more sensitively than SPP modes, while SPP modes may be more effective for monitoring bulk solution refractive index change. By properly selecting the wavelength, it is possible to excite either LSPR or SPP modes at the water/Ag interface, as shown in Fig. 4.8(c) and (d), and help to differentiate surface and bulk refractive index changes through their significantly different decay lengths. This unique feature would improve the ability of sensors to detect target biomolecules in complex solutions, such as blood samples [4.25].

4.4 Ultrathin plasmonic sensor chip for high-performance spectral sensing

To calibrate the sensor sensitivity and detection resolution, we integrated the fabricated sensor chip with a PDMS microfluidic channel and injected a series of glycerol–water solutions (0, 3, 6, 9, 12, and 15% glycerol concentration) with measured refractive index (RI) ranging from 1.331 to 1.352 (J. A. Woollam, V-VASE). As shown in Fig. 4.10(a), the transmission spectrum red-shifts monotonically with increase in the

RI of liquid solutions. The multiple maxima and minima in the non-normalized transmission spectrum arise from interferences of LSPR and SPPs (Fano resonances), as discussed above. The resonance wavelengths of LSPR and SPPs depend on the grating period, film thickness, slit-width, as well as the RI of substrate and surrounding medium. Thus, changes in the local RI of surrounding medium (e.g. glycerol–water solutions) shifts the positions of these spectral features, and can be monitored in real-time by continually recording these spectral features.

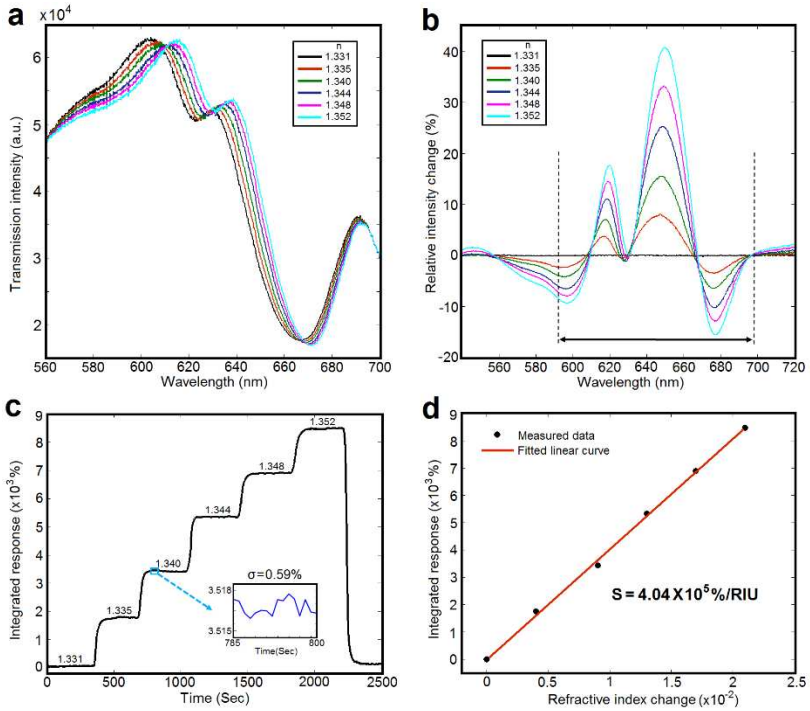

Fig. 4.10 Refractive index sensing using the proposed nanoplasmonic sensors consisting of ultrathin Ag nanogratings (period 420nm and slit-width 110nm). (a) The measured optical transmission spectra of the sensor in water and 3, 6, 9, 12, 15% glycerol–water mixtures with RI ranging from 1.331 to 1.352, as shown in the inset box. (b) The relative intensity changes $(I(\lambda) - I0(\lambda))/I0(\lambda))\times 100\%$ for liquids with different RI. The black dashed lines indicate the integration region. (c) The integrated sensor response as a function of time. The inset shows the noise level of the sensor response over 15 data points with the time interval of 1 sec. (d) Extracted sensor output for liquids with different RI. The red line is the linear fit to the measured data (black dot), showing good sensor linearity.

To exploit this sensing principle, we employ a multispectral data analysis

method, which makes use of more SPP-mediated spectral information than the traditional single-peak tracking method, and significantly improves the detection signal-to-noise ratio and sensor resolution [4.14-4.16, 4.26]. This method integrates the magnitude of the relative intensity changes $(I(\lambda) - I_0(\lambda))/I_0(\lambda)$ as a function of wavelength, where $I_0(\lambda)$ and $I(\lambda)$ are the transmitted intensities at wavelength λ in water and glycerol–water mixtures, respectively. The integrated response (IR) of the sensor can be expressed as: $IR = \sum_{\lambda_1}^{\lambda_2}(|I(\lambda) - I_0(\lambda)|/I_0(\lambda)) \times 100\%$, where λ_1 and λ_2 define the wavelength range for integration. Fig. 4.10(b) shows the relative intensity changes in percent for liquids of different refractive indices. The signals are most prominent in the spectral range from 590nm to 700nm, as indicated by the black dashed lines. The magnitude of relative intensity changes was integrated within this spectral range, providing the sensor output IR as a function of time. As shown in Fig. 4.10(c), the change in IR is approximately proportional to the increase in refractive index, showing excellent sensor linearity. Fig. 4.10(d) shows the extracted IR values as a function of the refractive index. The linear fit to the data points yields a sensor sensitivity of 4.04×10^5%/RIU. The inset of Fig. 4.10(c) indicates the noise level of the IR signal, which exhibits a standard deviation of 0.59% over 15 data points with a time interval of 1 sec. This corresponds to a bulk refractive index resolution of 1.46×10^{-6} RIU (i.e., 0.59%/(4.04×10^5%/RIU)).

4.5 Discussion

Table 4.1 Comparison of detection, temporal and spatial resolutions of state-of-the-art nanoplasmonic biosensors.

State-of-the-art Nanoplasmonic sensors	Detection Resolution (RIU)	Temporal Resolution (sec)	Spatial Resolution (μm^2)
Nanogratings on optically-thin Ag film	**1.46×10^{-6}**	**1**	**50×50**
Nanohole arrays on optically-thick Au film [8]	3.1×10^{-6}	2	200×200
Interferometric nanoring-hole arrays [15]	0.8×10^{-6}	10	150×150
Nanogratings on optically-thick Au film [10, 11]	1.74×10^{-5}	30	~150×150
Quasi-3D plasmonic crystals [26]	1×10^{-5}	90	1000×5000

Table 4.1 compares the detection, temporal, and spatial resolutions of the optically-thin Ag nanogratings studied here to those of other state-of-the-art nanoplasmonic sensors. As discussed in Ref. [4.27], there are inherent tradeoffs between these quantities, which need to be carefully balanced to achieve optimal performance of nanoplasmonic sensors. Note that the detection resolution demonstrated for the optically-thin Ag nanogratings (1.6×10^{-6} RIU) is among the lowest reported for state-of-the-art nanoplasmonic sensors, and compares very well with results reported for optically-thick nanohole arrays (3.1×10^{-6} RIU) [4.8], but with 2× better temporal resolution and an order of magnitude improvement in spatial resolution ($50\times50\mu m^2$ *v.s.* $200\times200\mu m^2$). The ultrathin nanogratings exhibit a slightly higher detection resolution than the ring-hole arrays (0.8×10^{-6} RIU), but have approximately an order of magnitude improvement in both temporal (1 sec *v.s.* 10 sec) and spatial resolution ($50\times50\mu m^2$ *v.s.* $150\times150\mu m^2$). In the real-time measurements, N_t=200 spectrum frames are averaged with an integration time of τ=5msec for each spectrum, yielding a temporal resolution of

$T=N_t \cdot \tau$ =1 sec. This is much shorter than that of nanoplasmonic sensors using ring-hole arrays (T=10 sec) [4.15], 1D nanogratings patterned on optically-thick metal films (T=30 sec) [4.10, 4.11], and quasi-3D plasmonic crystals (T=90 sec) [4.26]. This improved temporal resolution is attributed to the high resonant optical transmission (~40%) of the ultra-thin Ag nanogratings, which leads to a large photon flux on each detector pixel, permitting a rapid integration time τ=5 msec. The temporal resolution T=1 sec is comparable to that of commercial SPR sensors, and is sufficient for measuring the binding kinetics of most antibodies.

The temporal resolution, which is important for time-resolved sensing systems, can be further improved by averaging over a smaller number of spectra (e.g. N_t=50 or 100 frames) with only a modest increase in sensor noise ($\sigma \propto 1/\sqrt{N_t}$), resulting in a slightly poorer detection resolution [4.15, 4.27]. The temporal resolution could also be improved by enlarging the sensor footprint (currently 50×50μm^2) to increase the overall detected photon flux and allow a shorter integration time τ, but this would be at the expense of spatial resolution (sensor footprint), which is critical for high-throughput multiplexed sensing. Shorter integration times are desired to reduce the effects of shot noise and dark noise in the detector (dominant noise sources in optical biosensor systems), and hence improve the signal-to-noise ratio and detection resolution [4.8, 4.27]. Note that although optically-thick nanohole and ring-hole arrays employed larger sensor footprints (200×200μm^2 and 150×150μm^2) to increase the overall photon flux, the temporal resolution and integration time τ were still quit long due to the inherently low

transmission of those structures. The interferometric ring-hole arrays used a τ=50msec integration time, yielding a temporal resolution of T= 200×50msec=10 sec, while nanohole arrays had a 10msec integration time and a temporal resolution of T=200×10msec=2 sec [4.8, 4.15].

The observed improvements in sensor performance results from the high-contrast, narrow bandwidth, and large amplitude of the Fano-type spectrum profiles, as well as the advanced data analysis method employed. Several potential improvements could further enhance the signal-to-noise ratio and sensor resolution. These include: (1) increasing the size of ultra-thin nanogratings using large-area nanofabrication techniques (e.g., optical interference lithography [4.28]); (2) reducing the SPP loss by employing ultra-smooth metal films with larger grain sizes (e.g., using template stripping methods) [4.8,4.29,4.30]; (3) using a detector with a higher saturation level and faster frame rates to reduce the shot noise; (4) integrating temperature controllers with both sensor chip and light source to decrease the noise caused by temperature fluctuations [4.25]; and (5) optimization of microfluidic channels and sample transport to the sensing surface [4.4,4.31], etc.

4.6 Summary

In summary, we have demonstrated a novel nanoplasmonic sensor platform employing Fano resonances in 1D nanogratings patterned on ultrathin Ag films. We have observed Fano-type asymmetric spectral profiles with large transmission amplitude (~40%), high modulation ratio, and narrow line-widths. In addition to the simple sensor design, employing a standard microscope, a portable spectrometer, and PDMS

microfluidic channels, this sensor system can achieve a detection resolution of 1.46×10^{-6} RIU with high temporal resolution of 1 sec, and a miniaturized sensor footprint of $50\times50\mu m^2$. The sensor resolution is among the lowest reported for state-of-the-art nanoplasmonic sensors using ring-hole or nanohole arrays, but the temporal (1 sec *v.s.* 10 sec) and spatial ($50\times50\mu m^2$ v.s. $200\times200\mu m^2$) resolutions are significantly improved by 1 order of magnitude. Several potential methods have also been discussed for further performance improvement. The superior temporal, spatial and detection resolutions and simple optical geometry suggests exciting potential for sensitive, cost-effective, and portable biosensors with a high multiplexing capacity, which would significantly impact point-of-care diagnostics for personal healthcare.

References

[4.1] J. Homola, S. S. Yee & G. Gauglitz, Surface plasmon resonance sensors: review. Sensors and Actuators B: Chemical 54, 3-15 (1999).

[4.2] C. T., Campbell & G. Kim, SPR microscopy and its applications to high-throughput analyses of biomolecular binding events and their kinetics. Biomaterials 28, 2380-2392 (2007).

[4.3] J. Homola, Surface plasmon resonance sensors for detection of chemical and biological species. Chem. Rev. 108, 462-493 (2008).

[4.4] A. G. Brolo, Plasmonics for future biosensors. Nat. Photonics 6, 709 (2012).

[4.5] S. A. Maier, Plasmonics: Fundamental and Applications, Springer, New York (2007).

[4.6] J. N. Anker, et. al., Biosensing with plasmonic nanosensors. Nat. Mater. 7, 442 (2008).

[4.7] N. C. Lindquist, A. Lesuffleur, H. Im and S.-H. Oh, Sub-micron resolution surface plasmon resonance imaging enabled by nanohole arrays with surrounding Bragg mirrors for enhanced sensitivity and isolation. Lab Chip, 9, 382 (2009).

[4.8] H. Im, J. N. Sutherland, J. A. Maynard and S.-H. Oh, Nanohole-based surface plasmon resonance instruments with improved spectral resolution quantify a broad range of antibody-ligand binding kinetics. Anal. Chem., 84, 1941 (2012).

[4.9] A. A. Yanik, et al., Seeing protein monolayers with naked eye through plasmonic Fano resonances. Proc. Natl. Acad. Sci. U. S. A. 108, 11784 (2011).

[4.10] K. L. Lee, P. W. Chen, S. H. Wu, J. B. Huang, S. Y. Yang, & P. K. Wei, Enhancing surface plasmon detection using template-stripped gold nanoslit arrays on plastic films. ACS Nano 6, 2931 (2012).

[4.11] S. H. Wu, K. L. Lee, A. Chiou, X. Cheng, & P. K. Wei, Optofluidic Platform for Real-Time Monitoring of Live Cell Secretory Activities Using Fano Resonance in Gold Nanoslits. Small 9, 353213).

[4.12] T. W. Ebbesen, H. J. Lezec, H. F. Ghaemi, T. Thio, P. A. Wolff, Extraordinary optical transmission through sub-wavelength hole arrays. Nature 391, 667 (1998).

[4.13] F. J. Garcia-Vidal, L. Martin-Moreno, T. W. Ebbesen, & L. Kuipers, Light passing through subwavelength apertures. Rev. Mod. Phys. 82, 729 (2010).

[4.14] J. Feng, et al., Nanoscale plasmonic interferometers for multispectral, high-throughput biochemical sensing. Nano Lett. 12, 602 (2012).

[4.15] Y. Gao, Z. Xin, B. Zeng, Q. Gan, X. Cheng, & F. J. Bartoli, Plasmonic interferometric sensor arrays for high-performance label-free biomolecular detection. Lab on a Chip 13, 4755 (2013).

[4.16] Y. Gao, Z. Xin, Q. Gan, X. Cheng, and F. J. Bartoli, Plasmonic interferometers for label-free multiplexed sensing. Opt. Express 21, 5859 (2013).

[4.17] G. D'Aguanno, N. Mattiucci, A. Alu & M. J. Bloemer, Quenched optical transmission in ultrathin subwavelength plasmonic gratings. Phys. Rev. B 83, 035426 (2011).

[4.18] J. Braun, B. Gompf, G. Kobiela, & M. Dressel, How holes can obscure the view: suppressed transmission through an ultrathin metal film by a subwavelength hole array. Phys. Rev. lett. 103, 203901 (2009).

[4.19] B. Zeng, Y. Gao, & F. J. Bartoli, Ultrathin Nanostructured Metals for Highly Transmissive Plasmonic Subtractive Color Filters. Sci. Rep. 3, 2840 (2013).

[4.20] B. Luk'yanchuk, et. al., The Fano resonance in plasmonic nanostructures and metamaterials. Nat. Mater. 9, 707 (2010).

[4.21] B. Auguié & W. L. Barnes, Collective resonances in gold nanoparticle arrays. Phys. Rev. Lett. 101, 143902 (2008).

[4.22] A. Christ, et. al., Controlling the interaction between localized and delocalized surface plasmon modes: Experiment and numerical calculations. Physical Review B 74, 155435 (2006).

[4.23] H. Raether, Surface plasmons on smooth surfaces and rough surface and on gratings (Springer Berlin Heidelberg, 1988).

[4.24] Q. Cao & P. Lalanne, Negative role of surface plasmons in the transmission of metallic gratings with very narrow slits. Phys. Rev. Lett. 88, 057403 (2002).

[4.25] X. Fan, et. al., Sensitive optical biosensors for unlabeled targets: A review. Analytica Chimica Acta 620, 8 (2008).

[4.26] M. E. Stewart, et al., Quantitative multispectral biosensing and 1D imaging using quasi-3D plasmonic crystals. Proc. Natl. Acad. Sci. U. S. A. 103, 17143 (2006).

[4.27] M. Piliarik, & J. Homola, Surface plasmon resonance (SPR) sensors: approaching their limits?. Opt. Express 17, 16505 (2009).

[4.28] B. Zeng, X. Yang, C. Wang, & X. Luo, Plasmonic interference nanolithography with a double-layer planar silver lens structure. Opt. Express 17, 16783 (2009).

[4.29] P. Nagpal, N. C. Lindquist, S.-H. Oh & D. J. Norris, Ultrasmooth Patterned Metals for Plasmonics and Metamaterials. Science 325, 594–597 (2009).

[4.30] V. J. Logeeswaran, et al., Ultrasmooth Silver Thin Films Deposited with a Germanium Nucleation Layer. Nano Lett. 9, 178–182 (2009).

[4.31] A. Barik, et al., Dielectrophoresis-Enhanced Plasmonic Sensing with Gold Nanohole Arrays. Nano Lett. 14, 2006 (2014).

Chapter 5

Conclusions

In this chapter, we first summarize the results achieved in this dissertation and then propose future research directions.

5.1 Conclusions

This dissertation have clarified underlying physical mechanisms of SPRs in ultrathin nanostructured metals and tailored them for practical applications. Specifically, we discussed the physical mechanisms, designs, fabrication and characterization of 1D and 2D ultrathin Ag plasmonic nanostructures for applications in three most common and successful areas: plasmonic photovoltaics, plasmonic color filters, and plasmonic biosensors, achieving superior sensing performances comparable to their optically-thick counterparts.

In Chapter 2, we have studied plasmonic transparent conducting electrodes (TCEs) consisting of ultrathin two-dimensional (2D) or two one-dimensional (1D) perpendicular Ag nanogratings for organic photovoltaics (OPVs) with polarization-insensitive optical absorption enhancement. The proposed ultrathin transparent conducting electrodes have a calculated sheet resistance <10 Ω/sq, indicating a better electrical conductivity than that of traditional ITO electrodes. In addition, a strong polarization-insensitive optical absorption enhancement in the active layers of molecular OPVs has been demonstrated with ultrathin

2D Ag nanogrids and two 1D perpendicular Ag nanogratings electrodes, achieving record-high optical absorption enhancements of 150% and 200%, respectively. The OPV device with two 1D perpendicular Ag nanogratings, providing the strongest absorption enhancement in active layers, are more complex than that with single-layer ultrathin 2D nanogrids, but still should be feasible. This design principle is quite general and can be extended to other optoelectronic devices.

In addition, in Chapter 3, systematic theoretical and experimental studies have been performed to clarify the underlying physical mechanisms that determine the counter-intuitive Extraordinary Low Transmission (ELT) phenomenon in ultrathin Ag plasmonic nanogratings. By exploiting the ELT theory, we have proposed and demonstrated novel plasmonic subtractive colour filters (SCFs) associated with fundamentally different colour filtering mechanisms than previous state-of-the-art plasmonic colour filters, overcoming key challenges in current colorant and plasmonic colour filters. An unusually high transmission efficiency of 60~70% has been achieved, with the potential for further enhancement. In addition, the proposed plasmonic SCFs are capable of generating even smaller pixel sizes than the smallest pixels achieved today in commercial image sensors. Finally, their unique polarization-dependent features allow the same structures to function either as colour filters or highly-transparent windows under different polarizations, opening an avenue towards high-definition transparent displays.

Finally, in Chapter 4, we have demonstrated a novel nanoplasmonic sensor platform employing Fano resonances in 1D nanogratings patterned on ultrathin Ag films, in which

we have observed Fano-type asymmetric spectral profiles with large transmission amplitude (~40%), high modulation ratio, and narrow line-widths. In addition to its simple design, this sensor system employed a collinear transmission optical setup associated with a portable spectrometer, experimentally achieving a detection resolution of 1.46×10^{-6} RIU with high temporal resolution of 1 sec, and a miniaturized sensor footprint of $50\times50\mu m^2$. The detection resolution is among the lowest reported for other state-of-the-art nanoplasmonic sensors, but the temporal and spatial resolutions are significantly improved by 1 order of magnitude. The superior temporal, spatial and detection resolutions and simple optical geometry suggests exciting potential for sensitive, cost-effective, and portable biosensors with a high multiplexing capacity, which would significantly impact point-of-care diagnostics for personal healthcare.

5.2 Future directions

Experimental demonstration of power conversion efficiency (PCE) enhancement in OPVs with ultrathin plasmonic TCEs. Although we have numerically demonstrated record-high optical absorption enhancements in OPVs with the proposed ultrathin plasmonic TCEs, the absorption enhancements do not necessarily transfer to PCE enhancement in OPVs, which is the ultimate goal of the proposed plasmonic light-trapping approaches. Until now, a single-layer ultrathin 1D Ag NGs has been demonstrated to replace traditional ITO electrodes and enhance the PCE in OPVs [5.1], as shown in Fig. 5.1(a). However, due to fabrication challenges, direct evidence of PCE enhancement in OPVs with ultrathin 2D Ag NG and two 1D perpendicular Ag NG electrodes, which have

been demonstrated to achieve much stronger optical absorption enhancements than 1D Ag NGs, is still lacking. The OPV device with two 1D perpendicular Ag NGs, providing the strongest absorption enhancement in active layers, are more complex than that with single-layer ultrathin 2D NGs, but still should be feasible. For instance, in Fig. 5.1(b), improved PCE in OPVs with dual metallic nanostructures have been experimentally demonstrated by simultaneously incorporating Au nanoparticles and Ag nanogratings on the top and bottom interfaces [5.2]. With the development of nanofabrication techniques, it is promising to obtain experimental evidence of PCE enhancements in OPVs with the proposed ultrathin 2D Ag NG and two 1D perpendicular Ag NG electrodes.

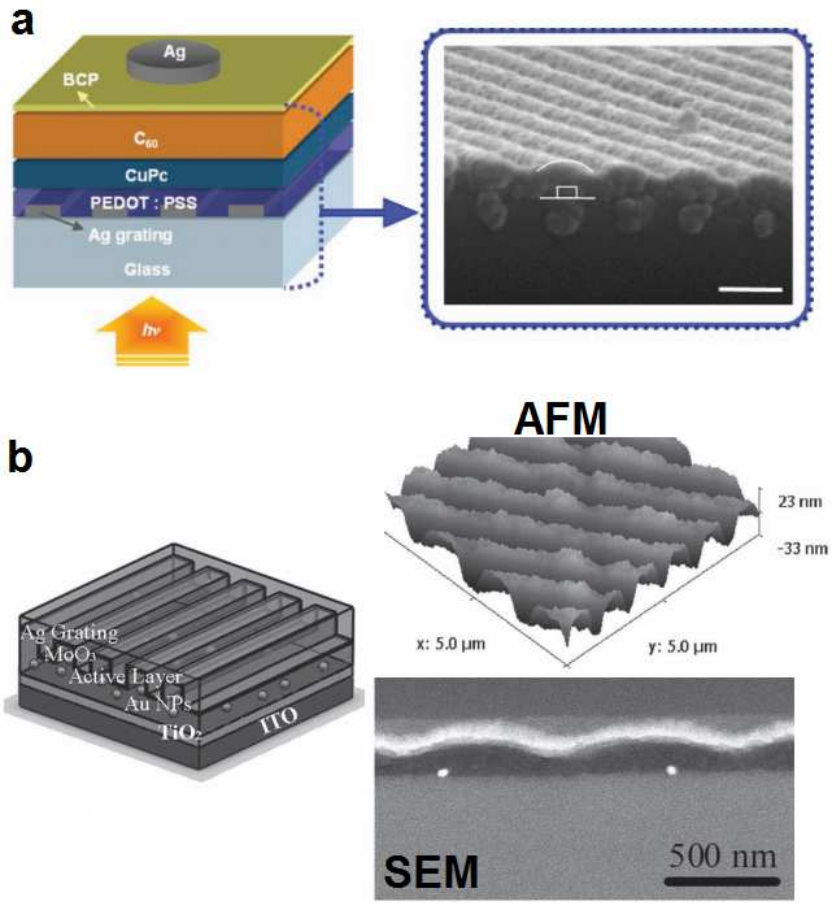

Fig. 5.1 (a) Schematic and SEM images of the fabricated OVPs with a single-layer of ultrathin Ag NGs. Organic layers are depicted with solid lines and the square shows the position of the Ag NGs on glass substrate [5.1]. The scale bar is 200 nm. (b) Schematic of the OPV device with dual metallic structures (left). AFM (top) and SEM (bottom) images of the OPVs with embedded Au nanoparticles (50 nm) in the active layer and patterned with Ag nanogratings (grating period = 750 nm) (right) [5.2].

Further development of ultrathin plasmonic subtractive color filters for practical applications. First of all, while only 1D ultrathin Ag nanograting structures have been demonstrated for a proof-of-principle experiment, the design principle of ultrathin plasmonic SCFs can be extended to 2D structures (e.g. nanoholes, nanosquares, etc.) to achieve polarization-independent operation for practical applications in high-resolution image sensors, displays, and cameras, etc. The design can also be easily applied to other spectrum regimes for different applications. In addition, since the structural parameters of plasmonic SCFs have not been optimized, further improvement may be possible to achieve transmission effiencies comparable to or even larger than that of commercial colorant color filters (80%). On the other hand, the proposed ultrathin plasmonic SCFs can function either as color filters or transparent windows under different polarizations. By combining liquid crystals that can actively control the polarization of incident light, a new approach for high-definition transparent displays can be realized.

Performance improvement in the ultrathin nanoplasmonic sensor platform. While the demonstrated sensor resolution for single-channel refractive index sensing is comparable to state-of-the-art nanoplasmonic sensors and commercial SPR systems, significant improvements in sensor performance are still possible. Additional improvements have the potential for further enhancement of the signal-to-noise ratio and sensor resolution,

including: (1) increasing the size of ultrathin nanogratings using large-area nanofabrication techniques; (2) reducing the SPP loss by employing ultra-smooth metal films with larger grain sizes; (3) using a detector with a higher saturation level and faster frame rates to reduce the sensor noise; (4) integrating temperature controllers with both sensor chip and light source to decrease the noise caused by temperature fluctuations; and (5) optimization of microfluidic channels and sample transport to the sensing surface, etc.

Sensing in complex biological samples. To facilitate the application in real biomedical sensing, this demonstrated ultrathin nanoplasmonic sensor platform needs to be able to detect analytes in complex biological samples such as blood, human serum, urine, etc. To achieve this goal, the next-step would be to optimize the surface modification to maintain receptor stability and minimize non-specific bindings in a complex solution. In addition, due to the significantly different decay lengths of LSPR and SPP modes (LSPR modes, with decay lengths of tens of nanometers, have the potential to probe surface binding events more sensitively than SPP modes; while SPP modes, with hundreds of nanometers decay lengths, may be more effective for monitoring bulk solution changes), it is possible to excite either LSPR or SPP modes at the water/Ag interface, which could aid in differentiating surface and bulk changes [5.3].

Sensor miniaturization and integration. An unique advantage of nanoplasmonic sensors with respect to commercially SPR systems is their potential for system miniaturization and integration. For instance, in Fig. 5.2, it will significantly decrease the cost and size of the system by replacing the spectrometer and white light source with a

simple CMOS detector and a LED light source [5.4], although trade-offs must be made between system miniaturization and performance degradation. Integration of nanoplamsonic sensor chips with smart phones is another research direction. Finally, to commercialize the proposed sensor system, we also need to package the sensor system, develop friendly software and hardware user-interfaces, and automate the instrument operation and sample handling.

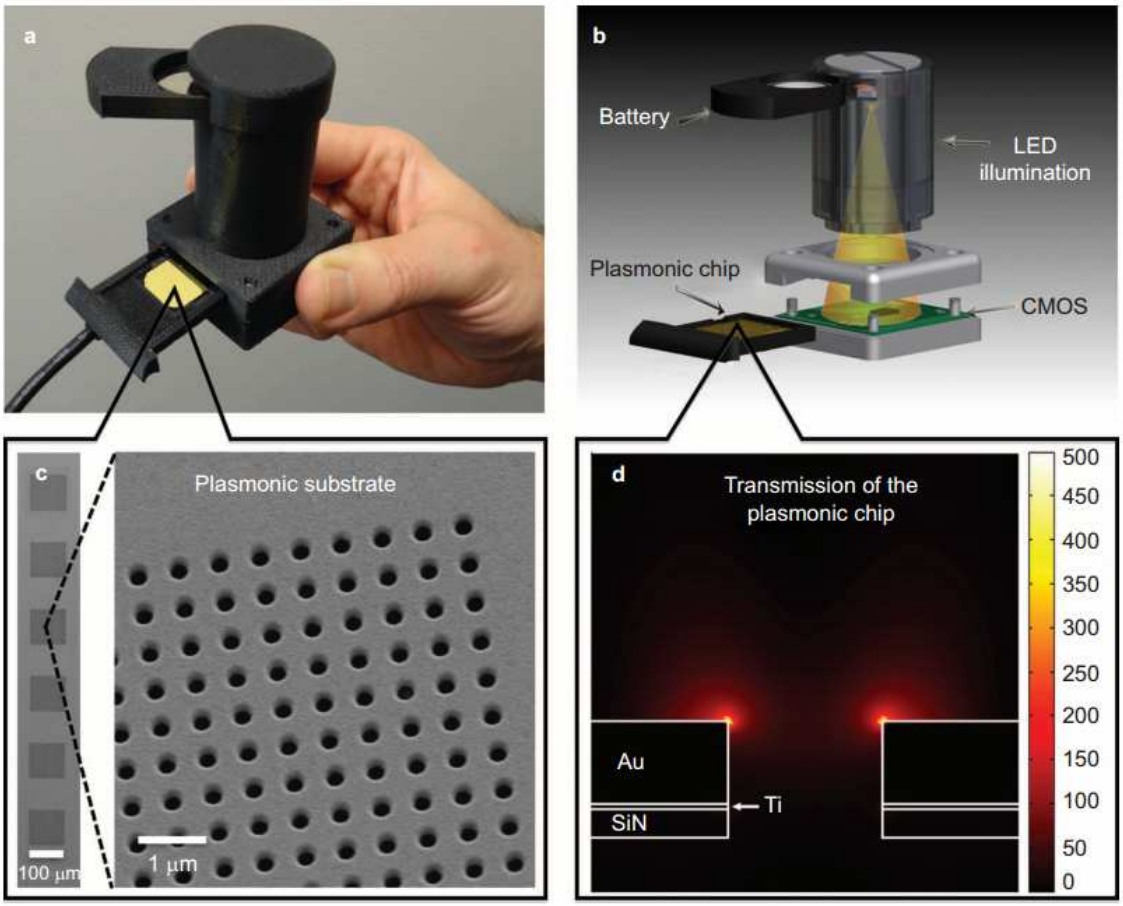

Fig. 5.2 On-chip sensing platform with plasmonic microarrays and lens-free computational imaging. (a) Real picture of the portable biosensing device. (b) Schematic of the on-chip biosensing platform comprising a battery, an LED, a plasmonic sensor chip and a CMOS imager chip. (c) SEM image of plasmonic sensor pixels and the zoomed image of a plasmonic pixel containing periodic nanohole array. (d) FDTD simulation of the near-field intensity enhancement distribution for the nanohole array [5.4].

References

[5.1] M.-G, Kang, et al., Efficiency enhancement of organic solar cells using transparent plasmonic Ag nanowire electrodes. Advanced Materials 22, 4378 (2010).

[5.2] X. Li, et al., Dual plasmonic nanostructures for high performance inverted organic solar cells. Advanced Materials 24, 3046 (2012).

[5.3] Slavík, R., Homola, J. and Vaisocherová, H., Advanced biosensing using simultaneous excitation of short and long range surface plasmons. Meas. Sci. Technol. 17, 932 (2006).

[5.4] A. E. Cetin, et al., Handheld high-throughput plasmonic biosensor using computational on-chip imaging. Light: Science & Applications 3, e122 (2014).

Name : **Beibei Zeng** Email : beibeizeng210@gmail.com Cell: 610-762-2360
Address: 7 ASA Drive, Room 219, Bethlehem, PA 18015

Education

- 08/2010-12/2014 Ph.D., Electrical and Computer Engineering Department, Lehigh University, PA, US
  (Advisor: Prof. Filbert J. Bartoli, *Fellow* of *IEEE and OSA*)
- 09/2007-06/2010 M.S., Institute of Optics and Electronics, Chinese Academy of Sciences, China (Advisor: Prof. Xiangang Luo)
- 09/2003-06/2007 B.S., College of Mechanical Science & Engineering, Jilin University, Jilin, China

Research Interests

Nano-photonics, nanofabrication, plasmonics, opto-electronics and their applications for next-generation display, bio-sensing, and photovoltaics.

Journal Publications

1. **B. Zeng**, Z. H. Kafafi, F. J. Bartoli, "Transparent Electrodes based on 2-D Ag Nanogrids and Double 1-D Ag Nanogratings for Organic Photovoltaics", ***J. Photon. Energy.*** (2014). (*in press*)
2. **B. Zeng**, Y. Gao, F. J. Bartoli, "Differentiating surface and bulk interactions in plasmonic interferometric sensor arrays", ***Nanoscale*** (2014). DOI: 10.1039/C4NR05495D
3. **B. Zeng**, Y. Gao, F. J. Bartoli, "Rapid and highly-sensitive detection using Fano resonances in ultra-thin plasmonic nanogratings", ***Appl. Phys. Lett.*** **105**, 161106 (2014).
4. [Invited] **B. Zeng***, K. Liu*, H. Song, Q. Gan, F. J. Bartoli, Z. H. Kafafi, "Super absorption of ultra-thin organic photovoltaic films", ***Opt. Commun.*** **314**, 48 (2014).
5. **B. Zeng**, Y. Gao, and F. J. Bartoli, "Ultrathin Nanostructured Metals for Highly Transmissive Plasmonic Subtractive Color Filters", ***Sci. Rep.*** **3**, 2840 (2013).
6. Y. Gao, Z. Xin, **B. Zeng**, Q. Gan, X. Cheng, and F. J. Bartoli, "Plasmonic interferometric sensor arrays for high-performance label-free biomolecular detection", ***Lab on a Chip*** **13**, 4755 (2013). (Cover Article)
7. **B. Zeng**, Q. Gan, Z. H. Kafafi, and F. J. Bartoli, "Polymeric Photovoltaics with Various Metallic Plasmonic Nanostructures", ***J. Appl. Phys.*** **113**, 063109 (2013).
   ("*The most-accessed articles from July-October 2013*")
8. **B. Zeng,** X. Yang, C. Wang, Q. Feng, X. Luo, "Super-resolution imaging at different wavelengths by using one dimensional metamaterial structure", ***J. Opt.*** **12**, 035104

(2010)
(Selected as ***Highlight* of 2010** by *Journal of Optics*).

9. X. Yang, L. Fang, **B. Zeng**, C. Wang, Q. Feng and X. Luo, "Deep subwavelength photolithography based on surface plasmon polariton resonance with metallic grating waveguide heterostructure," ***J. Opt*** **12**, 045001 (2010).
10. **B. Zeng,** X. Yang, C. Wang, and X. Luo, "Plasmonic interference nanolithography with a double-layer planar silver lens structure", ***Optics Express*** **17**, 16783 (2009).
11. **B. Zeng,** L. Pan, L. Liu, L. Fang, C. Wang and X. Luo, "Improved near field lithography by surface plasmon resonance in groove-patterned masks", ***J. Opt. A: Pure Appl. Opt.*** **11**, 125003 (2009).
12. X. Yang, **B. Zeng,** C. Wang, X. Luo, "Breaking the feature sizes down to sub-22nm by plasmonic interference lithography using dielectric-metal multilayer", ***Optics Express*** **17**, 21560 (2009).
13. T. Xu, L. Fang, **B. Zeng**, Y. Liu, C. Wang, Q. Feng and X. Luo, "Subwavelength nanolithography based on unidirectional excitation of surface plasmons," ***J. Opt. A: Pure Appl. Opt.*** **11**, 085003 (2009).
14. T. Xu, L. Fang, J. Ma, **B. Zeng**, Y. Liu, J. Cui, C. Wang, Q. Feng and X. Luo, "Localizing surface plasmons with a metal-cladding superlens for projecting deep-subwavelength patterns," ***Appl. Phys.*** **B 97**, 175 (2009).

Patents

1. **B. Zeng**, Y. Gao, F. J. Bartoli, "Ultrathin plasmonic subtractive color filters for transparent display and miniaturized image and display technologies", US Patent (Pending).
2. **B. Zeng**, F. J. Bartoli, "Transparent Plasmonic Nanogrid Electrodes for Absorption Enhancement in Thin-film Organic Photovoltaics", US Patent (Pending).
3. C. Zhao, X. Ming, Q. Zhang, B. Yang, **B. Zeng, "**A sort of secure wheel chair with self-locking devices", Chinese Patent **NO.** 200820150497.5

Professional Society Membership and Activities

- Member of Optical Society of America (OSA), IEEE, American Physics Society (APS), Material Research Society (MRS).
- Independent reviewer for over 15 leading journals including: *Nature: Scientific Reports*, *Phys. Rev.* A, *Appl. Phys. Lett.*, *Opt. Exp.*, *Opt. Lett.*, *Appl. Opt.*, *JOSA*, *Organic Electronics*, *Nanotechnology*, IEEE *JSTQE*, IEEE *Photonics Journal*, IEEE *PTL*, *J.of Phys.s* D, etc.